Journal of
*Composites Science*

MDPI

*Review*

# $WO_3/MoO_3$ Nanocomposite Thin Films and Heterostructures: Interfacial Synergy for Smart and Sustainable Technologies

**Aleksei V. Shchegolkov [1,*], Veronica O. Malinkina [1], Ivan A. Komarov [1,2,3], Vladimir V. Kaminskii [4] and Alexandr V. Shchegolkov [5]**

[1] Center for Project Activities, Scientific Research Department, Advanced Engineering School of Electric Transport, Moscow Polytechnic University, Moscow 107023, Russia; thehellfox@mail.ru (V.O.M.); master_kom@mail.ru (I.A.K.)
[2] Federal Research Center of Problems of Chemical Physics and Medicinal Chemistry of the Russian Academy of Sciences, Semenov Prospect 1, Chernogolovka 142432, Russia
[3] Moscow Center for Advanced Studies, Kulakova Str. 20, Moscow 123592, Russia
[4] Institute of Advanced Data Transfer Systems, ITMO University, St. Petersburg 197101, Russia; kam-vladimiro@yandex.ru
[5] Institute of Power Engineering, Instrumentation and Radioelectronics, Tambov State Technical University, Tambov 392000, Russia; energynano@yandex.ru
* Correspondence: alexxx5000@mail.ru

**Abstract**

Tungsten trioxide ($WO_3$) and molybdenum trioxide ($MoO_3$) are redox-active Group VI transition-metal oxides widely used in functional thin-film technologies. Many studies have examined single-phase $WO_3$ and $MoO_3$ films. However, $WO_3/MoO_3$ nanocomposite thin films and heterostructures have not yet been comprehensively reviewed as interface-engineered platforms for smart and sustainable technologies. This review addresses this gap by analyzing $WO_3/MoO_3$ thin-film nanocomposites through the concept of interfacial synergy. Particular attention is paid to the structural complementarity of $WO_3$ and α-$MoO_3$, oxygen nonstoichiometry, mixed $W^{6+}/W^{5+}/W^{4+}$ and $Mo^{6+}/Mo^{5+}/Mo^{4+}$ valence states, crystallographic-shear suboxides, W–O–Mo interfaces, and fabrication routes for mixed, graded, and multilayer films. The functional advantages of these systems do not arise from simply combining the two oxides. Instead, they result from charge and oxygen-vacancy redistribution, shortened ion–electron transport pathways, phase stabilization, and the formation of new active sites at interface boundaries. The review also emphasizes the need to distinguish genuine interfacial synergy from apparent improvements caused by surface area, film thickness, porosity, hydration, or measurement conditions. Finally, the review links structural features, defect chemistry, and interface-controlled properties to device-level functionality. This framework highlights promising directions for $WO_3/MoO_3$ nanocomposite films in a wide range of smart and sustainable technologies.

**Keywords:** nanocomposites; heterostructures; interface-engineered platforms; transition metal oxides; smart devices; sustainable technologies; Magnéli phases; thin-film architecture; oxygen vacancies

Check for updates

Academic Editor: Yongcai Zhang

Received: 8 July 2026
Revised: 7 August 2026
Accepted: 21 August 2026
Published: 1 September 2026

**Copyright:** © 2026 by the authors. Licensee MDPI, Basel, Switzerland. This article is an open access article distributed under the terms and conditions of the Creative Commons Attribution (CC BY) license.

## 1. Introduction

### 1.1. Structural Complementarity of $WO_3$ and α-$MoO_3$

Thin films of transition metal oxides (TMOs) occupy a central position in modern functional electronics [1], electrochemistry [2], photonics [3], sensing [4], and energy-saving

technologies [5]. Their importance stems from high chemical and thermal stability, potential radiation resistance, compatibility with low-temperature deposition on transparent and flexible substrates, widely tunable optical properties, and the ability to reversibly change cation valence states [6,7]. Unlike many narrowly functional materials, oxide films can simultaneously serve as an active optical layer [8], an ion-electron conductor [9], a surface catalyst [10], a buffer interlayer, or an electrode [11]. Consequently, developing thin-film oxide systems increasingly involves designing composite and heterostructured materials with controlled synthesis, defect structures, interface boundaries, and multilevel architectures rather than optimizing an individual oxide compound [12,13].

Tungsten trioxide ($WO_3$) and molybdenum trioxide ($MoO_3$) are redox-active Group VI TMOs widely employed in functional thin-film technologies (Figure 1a). Their $W^{6+}$ and $Mo^{6+}$ cations have a $d^0$ electronic configuration [5,14–16]. Both oxides can form oxygen-deficient phases, $WO_{3-x}$ and $MoO_{3-x}$ (Figure 1b), in which oxygen vacancies and the associated mixed-valence states of the cations largely govern their electronic, optical, electrochemical, and catalytic properties [17–19]. Despite their similar local coordination—both crystal structures are built from $MO_6$ octahedra—their crystallographic frameworks differ fundamentally (Figure 1).

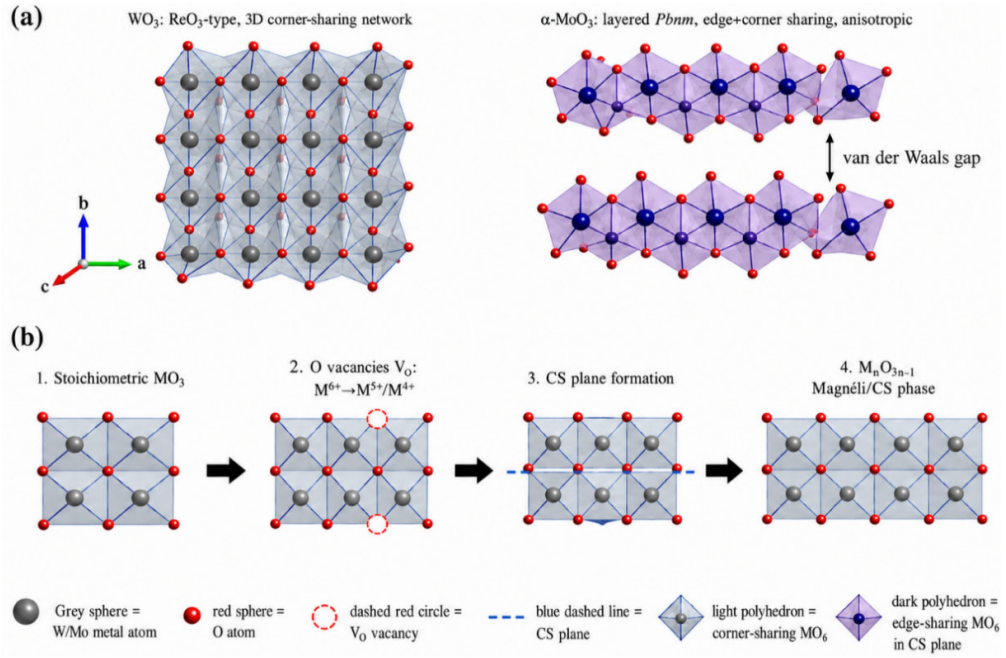



**Figure 1.** Crystallographic shear (CS) mechanism and phase families in $WO_3$ and $MoO_3$ systems: (**a**) crystal structures of $WO_3$ and $\alpha$-$MoO_3$; (**b**) schematic representation of CS plane formation and the evolution of Magnéli phases.

$WO_3$ adopts a three-dimensional framework structure derived from the $ReO_3$-type lattice, whereas $\alpha$-$MoO_3$ possesses a layered orthorhombic structure (space group Pbnm/Pnma) with van der Waals gaps separating the bilayers [5,19–21]. Consequently, $MoO_3$ exhibits pronounced anisotropy in ion transport and surface reactivity. However, it also suffers from intrinsically low electronic conductivity and a tendency toward structural rearrangement during deep ion intercalation [22–24].

The structural differences between $WO_3$ and $MoO_3$ play a pivotal role in determining ion transport, mechanical stability, cycling stability, and the overall functional performance of thin-film devices. The formation of oxygen vacancies and localized $W^{5+}/W^{4+}$ and $Mo^{5+}/Mo^{4+}$ states is particularly important. Changes in the coordination and connectivity of $MO_6$ octahedra reinforce these effects. Together, these factors strongly influence electronic

transport, optical absorption, surface chemical reactivity, and the intercalation of small cations such as $H^+$, $Li^+$, $Na^+$, and $K^+$ [24,25]. These structural and defect-related characteristics are particularly important for controlling broadband electrochromic modulation and for designing composite electrochromic films based on $WO_3/MoO_3$ heterostructures [19,22]. These combined structural and redox features make $WO_3$ and $MoO_3$ attractive for diverse functional applications, including electrochromic devices [22], gas sensors [26], lithium-ion batteries [27], adsorption technologies [28], photocatalysis [29], and other related technologies [20,30]. Consequently, $WO_3$ and $MoO_3$ provide complementary material platforms for the development of advanced ion-intercalation-based functional thin-film systems.

### *1.2. Beyond Single-Phase Thin Films: Interface-Engineered $WO_3/MoO_3$ Nanocomposites—Motivation and Scope of the Review*

Despite these advantages, single-phase $WO_3$ and $MoO_3$ thin films still suffer from fundamental limitations [31]. For $WO_3$, typical challenges include the trade-off among high optical modulation, fast electrochromic switching, and cycling stability, along with the need to balance electronic conductivity and ion diffusion. For $MoO_3$, the main limitations are low electronic conductivity, anisotropic ion transport, sensitivity to hydration, and pronounced volume expansion during deep $Li^+$ intercalation [32,33]. In photocatalysis and photoelectrochemistry, both oxides are limited by charge-carrier recombination and a narrow spectral response. In sensing applications, high sensitivity is often accompanied by insufficient selectivity, humidity interference, and slow recovery of the initial signal [19–22]. Thus, simply improving the morphology of a single-phase oxide does not necessarily produce a qualitative breakthrough in functional performance.

Consequently, increasing attention has shifted from single-phase $WO_3$ and $MoO_3$ thin films toward compositionally and interface-engineered $WO_3/MoO_3$ systems, including mixed oxides, nanocomposite coatings, compositionally graded films, heterostructures, and nanolaminated hybrid architectures [34]. Their superior performance arises not merely from the additive properties of the two constituent oxides but from interfacial synergy. This synergy involves charge redistribution across the W–O–Mo interface, modulation of oxygen-vacancy concentration, formation of mixed-valence $W^{6+}/W^{5+}$ and $Mo^{6+}/Mo^{5+}$ states, reorganization of $H^+/Li^+$ intercalation pathways, and modification of optical absorption [35]. Within these architectures, $WO_3$ can serve as a relatively stable electrochromic framework, whereas $MoO_3$ provides layered ion-transport channels, a high work function, surface redox activity, and additional adsorption sites [36,37]. However, improved functional performance requires precise control of the composition, phase state, and robust interfacial architecture of the $WO_3/MoO_3$ system [24,34,35].

However, $WO_3/MoO_3$ systems remain inherently complex to interpret because the nominal W:Mo ratio does not necessarily reflect the actual active phase composition. Hydration, annealing temperature, oxygen partial pressure, substrate characteristics, and film thickness can all shift the equilibrium among amorphous, crystalline, hydrated, substoichiometric, and mixed-phase structures. For $WO_3$, oxygen-deficient suboxides and Magnéli phases, including $W_{18}O_{49}$, $W_{20}O_{58}$, $W_{25}O_{73}$, and related CS phases of the $WO_{3-x}$ system, are particularly important. Their CS planes generate new electronic states [38]. In the case of $MoO_3$, suboxides such as $Mo_4O_{11}$, $Mo_8O_{23}$, $Mo_9O_{26}$, and other CS phases also play significant roles. However, their thermodynamic stability and $Li^+$ intercalation behavior differ substantially from those of the tungsten-based phases [31]. Therefore, conclusions regarding interfacial synergy should be based not only on the evaluation of functional performance but also on direct characterization of the phase composition, oxidation states, and interfacial structure.

This review is motivated by the recognition that further improvements in $WO_3$ and $MoO_3$ thin films can no longer be achieved merely by optimizing the individual single-

phase oxides. For electrochromic devices, it is essential to simultaneously achieve high coloration efficiency (CE), fast switching kinetics, and excellent cycling stability. In gas sensors, the respective contributions of oxygen vacancies, humidity, catalytic active sites, and phase composition must be distinguished. For energy-storage applications, the low electronic conductivity and mechanical degradation of $MoO_3$ during deep $Li^+$ intercalation must be overcome. In photocatalysis and photoelectrochemistry, efficient charge separation, controlled oxygen nonstoichiometry, and proper energy-band alignment are critical for maximizing performance [37]. These challenges require a transition from simply combining $WO_3$ and $MoO_3$ to rationally designing reproducible, interface-engineered $WO_3/MoO_3$ platforms. In such platforms, composition, oxygen-vacancy concentration, phase boundaries, and W–O–Mo interfacial contacts are interconnected parameters that govern functional performance.

Thus, the aim of this review is to establish a unified concept of interfacial synergy in $WO_3/MoO_3$ nanocomposite thin films and heterostructures as interface-engineered materials for smart windows, sensors, energy-storage devices, organic electronics, and photoactive systems. To achieve this aim, the article:

1. Compares the structural and electronic features of $WO_3$ and $\alpha$-$MoO_3$.
2. Examines the role of oxygen vacancies, mixed-valence states, and CS-suboxides.
3. Summarizes methods for fabricating mixed, compositionally graded, and multilayer $WO_3/MoO_3$ thin films.
4. Analyzes the functional applications of $WO_3/MoO_3$ nanocomposite thin films.
5. Identifies the limitations that hinder the transition from laboratory-scale demonstrations to reproducible devices.

## 2. Structural, Electronic, Defect, and Interfacial Fundamentals of $WO_3/MoO_3$ Nanocomposite Thin Films

This section discusses the physicochemical basis of interfacial synergy in $WO_3/MoO_3$ nanocomposite thin films. The main emphasis is placed on three interconnected levels: the structural complementarity of $WO_3$ and $\alpha$-$MoO_3$; the defect chemistry of oxygen-deficient $WO_{3-x}/MoO_{3-x}$ phases; and the role of W–O–Mo interfaces in coupled ion–electron transport. This approach allows $WO_3/MoO_3$ to be considered not as a mechanical mixture of two oxides but as a defect- and interface-engineered thin-film architecture.

### *2.1. Crystalline Architecture and Structural Complementarity of $WO_3$ and $\alpha$-$MoO_3$*

$WO_3$ and $MoO_3$ are closely related in terms of their chemical nature and redox activity, yet they represent distinct types of oxide frameworks [39]. $WO_3$ adopts a distorted $ReO_3$-type three-dimensional framework composed of corner-sharing $WO_6$ octahedra. This framework readily accommodates tilting, displacement, and local rearrangement of the octahedra during the intercalation of small cations. Consequently, the properties of $WO_3$ thin films are highly sensitive to crystallinity, the degree of hydration, oxygen nonstoichiometry, porosity, and annealing conditions. Each of these factors directly influences the optical response, electrochromic switching kinetics, and cycling stability [40].

In contrast to $WO_3$, $\alpha$-$MoO_3$ possesses a layered orthorhombic crystal structure in which distorted $MoO_6$ octahedra are arranged into bilayers separated by van der Waals gaps. The layered nature of $\alpha$-$MoO_3$ is clearly reflected in the morphology of its microcrystals and nanoplates. Figure 2 presents SEM images, reported by Martín-Ramos et al., of $\alpha$-$MoO_3$ with a multilayered plate-like architecture [41]. These micrographs clearly illustrate why $\alpha$-$MoO_3$ is widely regarded as a source of anisotropic ion-transport pathways and highly surface-active crystallographic planes.

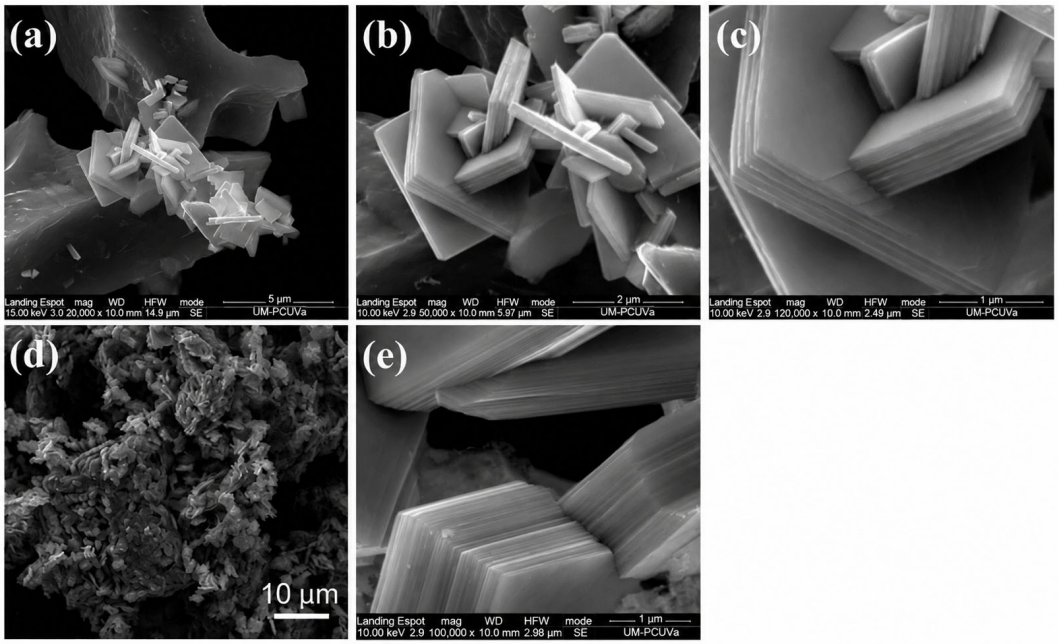



**Figure 2.** (**a**–**c**) SEM micrographs of α-$MoO_3$ crystals exhibiting a multilayered stacked morphology acquired at magnifications of ×20,000, ×50,000, and ×120,000, respectively; (**d**) SEM image of $MoO_3$ crystals obtained by calcination of commercial molybdic acid ($MoO_3 \cdot H_2O$); (**e**) high-magnification SEM image showing the layered stacking of an α-$MoO_3$ crystal consisting of 44 individual layers. Reproduced from [41] (MDPI, CC BY 4.0).

This architecture increases the sensitivity of $MoO_3$ to hydration, reduction, phase transformations, and mechanical degradation during deep $Li^+$ insertion. In this respect, α-$MoO_3$ can be compared with graphite, the classical layered anode material for lithium-ion batteries (LIBs). In graphite, lithiation mainly proceeds by reversible intercalation between graphene layers to form $Li_x C_6$, giving a theoretical intercalation capacity of approximately 372 mAh $g^{-1}$. $MoO_3$ must be treated differently because two electrochemical regimes are possible. Limited lithiation may involve comparatively reversible insertion and pseudocapacitive redox within the oxide framework, whereas deeper lithiation leads to conversion chemistry. The frequently quoted value of approximately 1117 mAh $g^{-1}$ corresponds to the complete six-electron reaction:

$$MoO_3 + 6Li^+ + 6e^- \rightarrow Mo^0 + 3Li_2O\ (Mo^{6+} \rightarrow Mo^0) \quad (1)$$

It is therefore the theoretical limit of deep conversion, not a reversible electrochromic or intercalation capacity. Approaching this limit requires extensive Mo–O bond breaking, phase reconstruction, and large volume changes; therefore, the 1117 and 372 mAh $g^{-1}$ values should not be compared as equivalent reversible intercalation capacities. Consequently, nanostructuring, carbon matrices, and interfacial stabilization are important for retaining the lower-depth reversible storage contribution and limiting conversion-induced mechanical damage [39,41–46].

The structural differences between the two oxides provide a fundamental design advantage for $WO_3/MoO_3$ nanocomposites. Within these $WO_3/MoO_3$ architectures, $WO_3$ can serve as a structurally robust three-dimensional electrochromic or pseudocapacitive framework. $MoO_3$, meanwhile, contributes layered ion-transport channels, a high work function, coordinatively unsaturated surface Mo–$O_x$ sites, and additional $Mo^{6+}/Mo^{5+}$ redox couples capable of participating in charge transfer, adsorption, and catalytic reactions. Consequently, the rational design of $WO_3/MoO_3$ nanocomposites requires consideration

of the nominal W:Mo ratio and phase connectivity. It must also account for the spatial distribution of the $MoO_3$ phase, the continuity of coupled ion–electron transport pathways, and the structural stability of W–O–Mo heterointerfaces during prolonged electrochemical cycling. Figure 3 illustrates how the structural asymmetry of $WO_3$ and α-$MoO_3$ can be exploited to construct $WO_3/MoO_3$ heterointerfaces. The three-dimensional $WO_3$ framework provides structural robustness and distributed intercalation sites, whereas the layered α-$MoO_3$ matrix creates anisotropic ion-transport pathways together with a highly surface-active architecture.

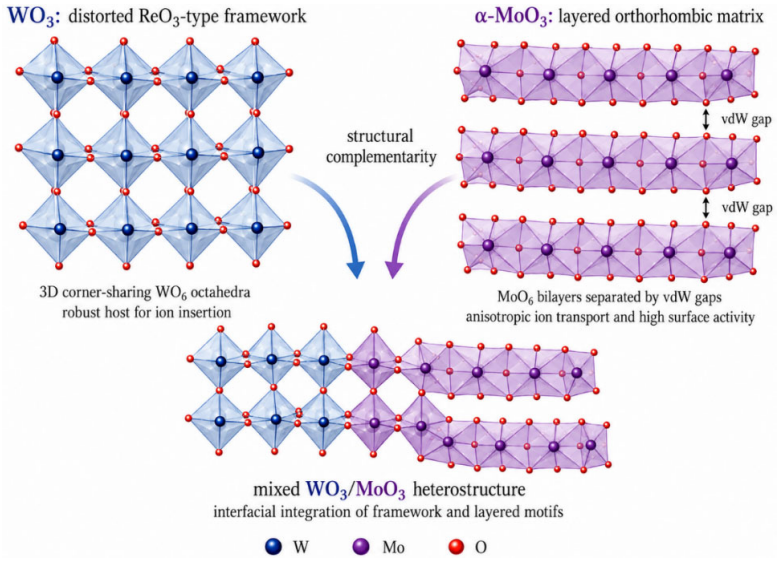
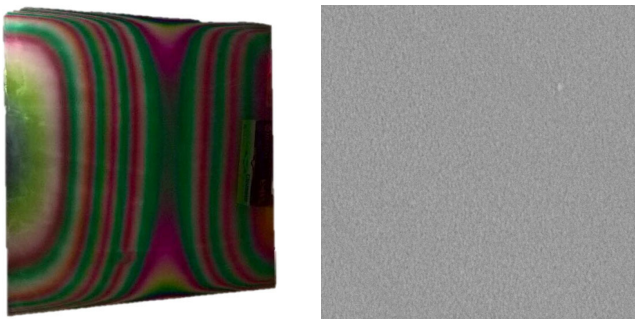



**Figure 3.** Structural complementarity of $WO_3$ and α-$MoO_3$ as a basis for $WO_3/MoO_3$ heterointerface formation and interfacial synergy.

Microscopic analysis of thin films confirms that the structural architecture of an oxide is directly related to its functional properties. Deposition and annealing conditions affect grain structure, thickness, crack formation, porosity, and the accessibility of active surface sites [42,43]. The relationship between fabrication method, composition, and morphology is illustrated in Figure 4 using data reported by Lábadi et al. [14].



(**a**) (**b**)

**Figure 4.** Photograph and SEM micrograph of a compositionally graded $WO_3/MoO_3$ thin-film structure: (**a**) photograph of a 30 × 30 $cm^2$ substrate coated with compositionally graded $WO_3/MoO_3$ layers; the interference fringes reflect spatial variations in film thickness and composition; (**b**) SEM micrograph of a 4 × 4 $\mu m^2$ area recorded from the central region of a 10 cm long Si substrate. Reproduced from [14] (MDPI, CC BY 4.0).

The compositionally graded $WO_3/MoO_3$ film deposited on a large-area substrate exhibits pronounced interference fringes (Figure 4a), reflecting spatial variations in coating thickness and composition. The corresponding SEM surface image shows a dense and

relatively uniform thin-film morphology (Figure 4b), which is characteristic of coatings formed by reactive magnetron sputtering (RMS).

For $WO_3$, the relationship among annealing temperature, film morphology, and electrochromic switching speed is fundamentally important. The switching process is governed by the intercalation and deintercalation of small cations and electrons. Figure 5 shows FE-SEM images of the surfaces and cross-sections of electrodeposited $WO_3$ films after annealing at 50, 250, and 450 °C. According to the micrographs, the transition from 50 to 250 °C is accompanied by grain coarsening and densification of the coating, whereas annealing at 450 °C leads to the formation of cracks and agglomerated regions. Such morphological changes may deteriorate the uniformity of $Li^+/H^+$ insertion, increase local mechanical stresses, and reduce the cycling stability of the electrochromic response [43].

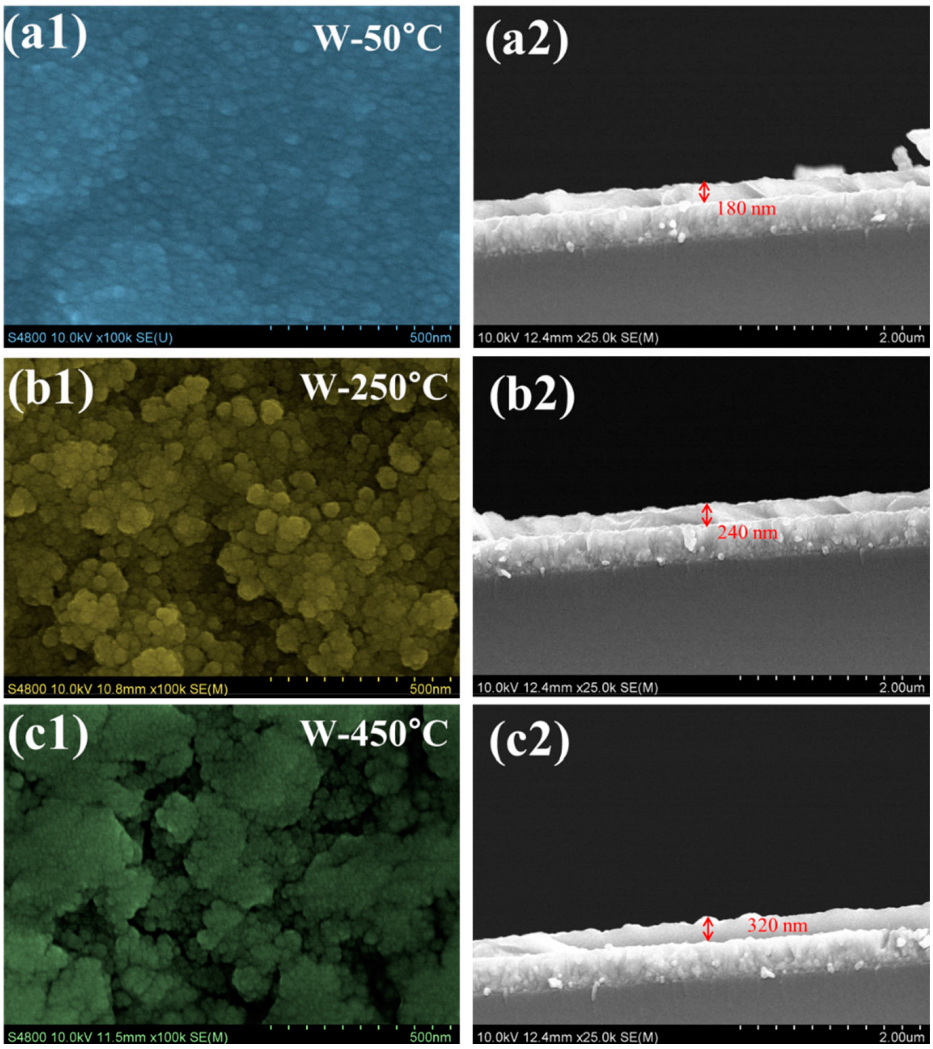



**Figure 5.** FE-SEM surface and cross-sectional images of electrodeposited $WO_3$ thin films annealed at different temperatures: (**a1**) surface morphology after annealing at 50 °C; (**a2**) corresponding cross-sectional morphology after annealing at 50 °C; (**b1**) surface morphology after annealing at 250 °C; (**b2**) corresponding cross-sectional morphology after annealing at 250 °C; (**c1**) surface morphology after annealing at 450 °C; (**c2**) corresponding cross-sectional morphology after annealing at 450 °C. The images illustrate the temperature-dependent evolution of grain structure, film densification, thickness, and crack formation. Reproduced from [43] (MDPI, CC BY 4.0).

Table 1 summarizes the key structural features of $WO_3$ and $\alpha$-$MoO_3$ and illustrates how the differences between the three-dimensional framework-type and layered oxide matrices can be exploited in the design of composite thin films. Comparison of these

parameters shows that the functional value of $WO_3/MoO_3$ systems is not determined by the properties of either oxide alone. Instead, it depends on their controlled integration within a stable architecture that jointly defines phase connectivity, interfacial W–O–Mo contacts, and coupled ion–electron transport pathways.

**Table 1.** Structural features of $WO_3$ and $\alpha$-$MoO_3$ governing the behavior of $WO_3/MoO_3$.

| No | Parameter | $WO_3$ | $\alpha$-$MoO_3$ | Design Implication for $WO_3/MoO_3$ | Ref. |
|---|---|---|---|---|---|
| 1 | Oxide matrix | Distorted $ReO_3$-type three-dimensional network of corner-sharing $WO_6$ octahedra; a framework for reversible $H^+/Li^+$ insertion | Layered $MoO_6$ bilayers separated by van der Waals gaps; anisotropic ion transport | Combining the three-dimensional stability of $WO_3$ with the layered transport channels of $MoO_3$ increases functional flexibility | [39–41] |
| 2 | Morphology | Grain size, porosity, thickness, and crack formation depend strongly on annealing and deposition conditions | Plate-like and multilayered morphology increases the surface area and accessibility of interlayer regions | Morphology should enhance transport while avoiding uncontrolled degradation, cracking, and mechanical instability | [41,43] |
| 3 | Defect sensitivity | Oxygen vacancies and $W^{5+}/W^{4+}$ states modulate electronic conductivity and the electrochromic response | Oxygen vacancies and $Mo^{5+}/Mo^{4+}$ states strongly affect conductivity, work function, and structural stability | Defect density should be controlled rather than maximized, because excessive nonstoichiometry may reduce stability | [39,47,48] |
| 4 | Intercalation behavior | More distributed three-dimensional intercalation of small cations within the $WO_3$ framework | Directional $Li^+$ intercalation along the layers; risk of lattice expansion during deep lithiation | $MoO_3$ is preferably introduced as a thin layer, nanodomain, or interfacial modifier rather than as a thick unstable phase | [45] |
| 5 | Electronic profile | $WO_3$ generally exhibits n-type semiconducting behavior under oxygen-deficient conditions | The high work function of $MoO_3$ is associated with its layered dipolar structure and surface electronic states | The W–O–Mo interface can tune charge transfer, contact selectivity, and coupled ion–electron transport | [44,47] |

### *2.2. Oxygen Vacancies, Mixed-Valence States, and Crystallographic-Shear Suboxides*

Oxygen vacancies are one of the key tools for tuning the properties of $WO_3$, $MoO_3$, and their nanocomposite heterostructures. Their formation disrupts the local coordination of $MO_6$ octahedra, alters the electron density at the cations, and generates the mixed-valence states $W^{6+}/W^{5+}/W^{4+}$ or $Mo^{6+}/Mo^{5+}/Mo^{4+}$. In $WO_3$, vacancies can act as donor defects, enhance n-type conductivity, and influence the electrochromic response [47]. In $MoO_3$, oxygen vacancies can increase conductivity and surface activity, but in excess they initiate hydration, phase drift, and reduction to lower oxide states [48].

XPS provides one of the most direct methods for investigating valence states and oxygen nonstoichiometry. For $WO_3$, the W 4f and O 1s regions allow the surface chemical state to be evaluated by tracking the relative contributions of stoichiometric $W^{6+}$ centers, reduced $W^{5+}/W^{4+}$ states, and oxygen-containing surface components. In particular, deconvolution of the W 4f spectrum reveals the degree of tungsten reduction and the possible

formation of oxygen vacancies. The O 1s region distinguishes lattice oxygen, hydroxyl groups, and adsorbed oxygen-containing species. Figure 6 presents a representative XPS analysis of a $WO_3$ film, including the survey spectrum as well as detailed spectra of the W 4f and O 1s regions [43].

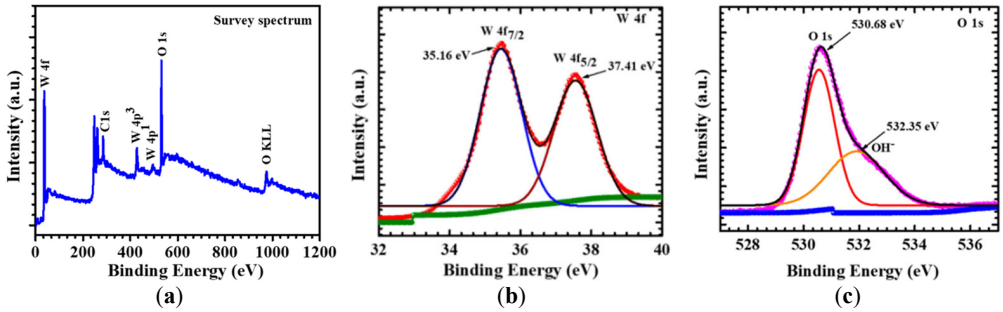



**Figure 6.** XPS spectra of the electrodeposited $WO_3$ thin film: (**a**) survey spectrum; (**b**) high-resolution W 4f core-level spectrum showing the W $4f_7/_2$ (35.16 eV) and W $4f_5/_2$ (37.41 eV) components; (**c**) high-resolution O 1s core-level spectrum containing the lattice-oxygen component at 530.68 eV and the higher-binding-energy $OH^-$ component at 532.35 eV. In the high-resolution spectra, the experimental signal is shown together with the overall fitted envelope and the individual deconvoluted peak components used to identify the corresponding chemical states. Reproduced from [43] (MDPI, CC BY 4.0).

Figure 7 compares the Mo 3d and O 1s XPS spectra of untreated and thermally annealed sputtered $MoO_3$ films. The Mo 3d envelope is dominated by the $Mo^{6+}$ spin–orbit doublet, confirming $MoO_3$ as the principal surface phase. A minor $Mo^{5+}$ contribution is present on the lower-binding-energy side and becomes slightly more pronounced after annealing at 300 °C, indicating increased oxygen deficiency. The narrowing of the $Mo^{6+}$ peaks with increasing annealing temperature reflects a more uniform local chemical environment around molybdenum. In the O 1s region, the main component at approximately 530.4–530.6 eV is assigned to lattice oxygen, whereas the higher-binding-energy contribution is associated mainly with surface hydroxyl and contamination-related oxygen species.

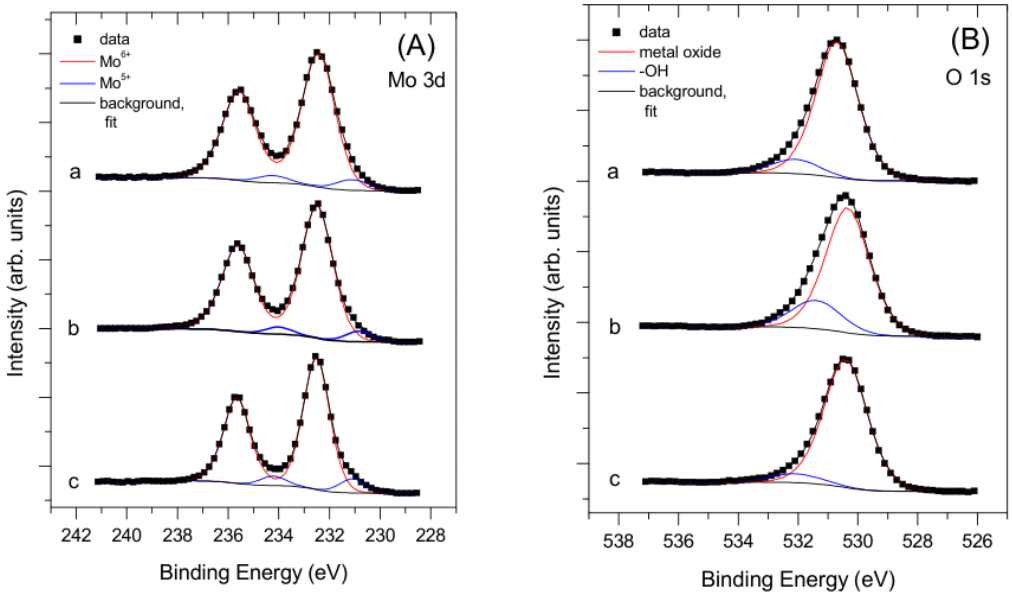



**Figure 7.** High-resolution XPS spectra of sputtered $MoO_3$ thin films: (**A**) Mo 3d and (**B**) O 1s regions for the untreated film (a) and films annealed at 200 °C (b) and 300 °C (c). Reproduced from [49] (MDPI, CC BY 4.0).

Upon deeper reduction in $WO_{3-x}$ and $MoO_{3-x}$, the defect structure evolves from dilute, statistically distributed oxygen vacancies toward more ordered CS suboxide phases. In such structures, oxygen deficiency is accommodated not merely as isolated point defects but through shear-plane formation. These planes alter the local connectivity of $MO_6$ octahedra, creating edge-sharing regions in addition to corner-sharing linkages. Figure 8 integrates the oxygen-deficiency-driven phase evolution and defect-engineering pathways in $WO_{3-x}$ and $MoO_{3-x}$. In Figure 8, the arrows indicate the progression from stoichiometric oxides toward increasingly oxygen-deficient and reduced states. The color coding distinguishes the $WO_{3-x}$ and $MoO_{3-x}$ structural-evolution pathways and the principal defect states, while the vacancy, electron/polaron, and mixed-valence symbols represent oxygen vacancies, localized charge carriers, and reduced W/Mo centers, respectively. With increasing reduction, $WO_{3-x}$ commonly forms relatively ordered crystallographic-shear suboxides, including $W_{18}O_{49}$, $W_{20}O_{58}$, $W_{25}O_{73}$, and $W_5O_{14}$, which can enhance electronic conductivity, near-infrared absorption, and electrochemical activity. In contrast, $MoO_{3-x}$ exhibits a more complex phase landscape: $Mo_8O_{23}$ and $Mo_9O_{26}$ are associated with shear structures, whereas $Mo_4O_{11}$ and related suboxides contain mixed Mo coordination environments and are not strict CS phases. Thus, the common $MO_{3-x}$ notation does not imply identical defect topologies or reduction mechanisms in the W–O and Mo–O systems. Oxygen vacancies, mixed-valence states, and small polarons may improve optical modulation, ion transport, surface reactivity, and charge conduction; however, excessive reduction can promote hydration, phase drift, irreversible ion trapping, and structural degradation.

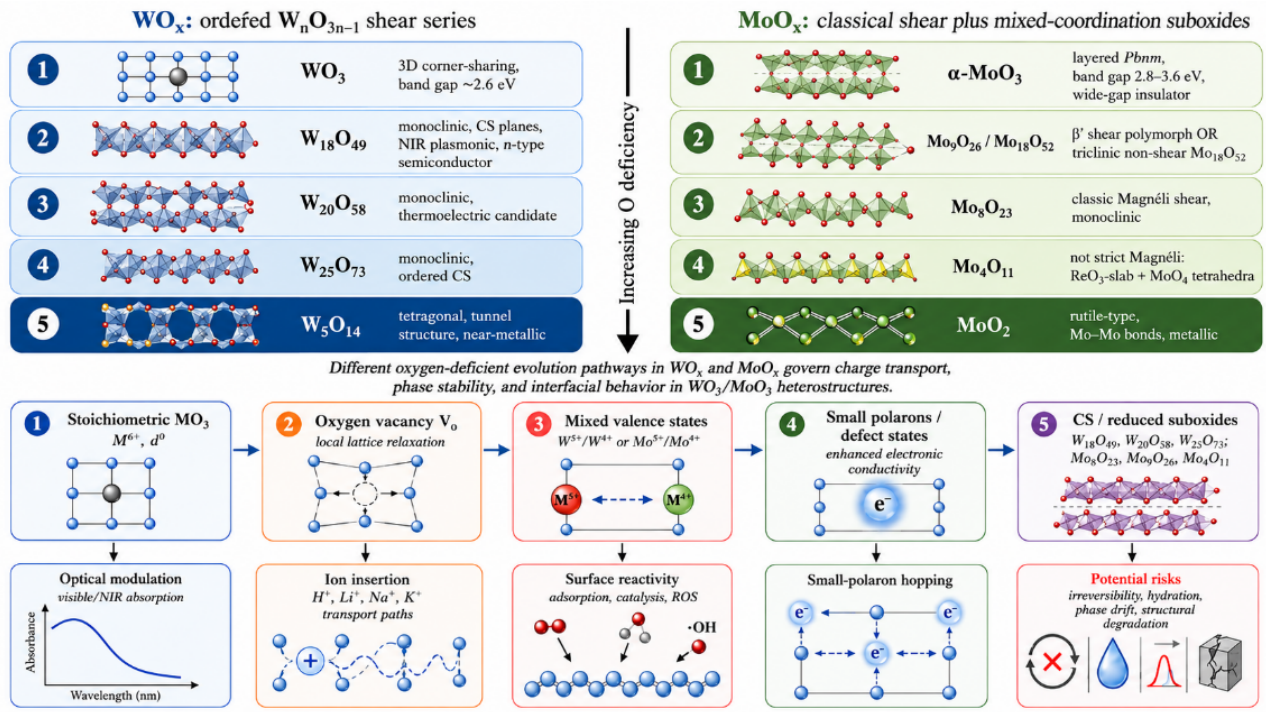



**Figure 8.** Oxygen-deficiency-driven structural evolution and defect-engineering pathways in $WO_{3-x}$ and $MoO_{3-x}$ systems, illustrating the formation of mixed-valence states, small polarons, crystallographic-shear or mixed-coordination suboxides, their functional contributions, and the associated stability risks.

The different phase-evolution pathways of oxygen-deficient $WO_{3-x}$ and $MoO_{3-x}$ systems have important consequences for the long-term stability of $WO_3$/$MoO_3$-based devices operating under repeated ion insertion/extraction or prolonged illumination conditions. Because tungsten- and molybdenum-based suboxides accommodate oxygen deficiency

through different structural mechanisms, their responses to continuous redox cycling are not equivalent. $WO_x$ systems generally evolve through relatively ordered crystallographic-shear structures, which can preserve extended lattice connectivity and provide enhanced electronic transport. In contrast, $MoO_x$ exhibits a broader range of reduced phases, including mixed-coordination suboxides, which may induce stronger local structural rearrangement, lattice distortion, and phase instability during prolonged operation.

Therefore, the stability of $WO_3/MoO_3$ heterostructures is architecture-dependent and determined by the balance between defect activation and structural preservation. Under repeated $H^+/Li^+$ intercalation or prolonged photoexcitation, differences in oxygen-vacancy mobility, reduction pathways, and local lattice response can lead to asymmetric degradation mechanisms, including chemical strain accumulation, interlayer sliding, trapped charge formation, and interfacial stress development. Recent studies have demonstrated that coherent interfacial constraint can substantially suppress structural deformation. For example, coherent pinning reduced the b-axis expansion of α-$MoO_3$ from approximately 16% to approximately 2%. This result highlights the importance of mechanical coupling at heterointerfaces [45]. Conversely, uncontrolled reduction and vacancy redistribution may accelerate phase drift and loss of functional reversibility [50].

Consequently, the long-term reliability of $WO_3/MoO_3$ devices should not be evaluated solely from the initial electrochemical, optical, or photocatalytic response. A comprehensive stability assessment requires monitoring phase retention, oxidation-state distribution, oxygen-vacancy evolution, impedance characteristics, and optical/electrochemical recovery after prolonged operation. Since $WO_{3-x}$ and $MoO_{3-x}$ follow inherently different phase-evolution pathways, degradation processes in $WO_3/MoO_3$ heterostructures are expected to be spatially and chemically asymmetric. Thus, stable device architectures should be designed not only to maximize interfacial activity but also to maintain phase compatibility, controlled defect mobility, and reversible W–O–Mo interfacial coupling during long-term operation.

For oxygen-deficient $MoO_{3-\delta}$ thin films, δ denotes a slight deficiency of lattice oxygen and the associated oxygen-vacancy concentration. Variations in oxygen nonstoichiometry, molybdenum oxidation state, and the fraction of suboxide components directly affect electrode behavior in lithium microbatteries [51,52]. In oxygen-deficient $MoO_{3-x}$, oxygen vacancies can enhance the pseudocapacitive contribution to charge storage by increasing the density of redox-active sites and facilitating coupled ion–electron transport [53]. Therefore, increased conductivity, changes in optical coloration, or improved capacity in $WO_3/MoO_3$ thin films should not automatically be interpreted as direct evidence of interfacial synergy. Such effects may originate not only from the formation of W–O–Mo interfaces, but also from changes in porosity, film thickness, hydration degree, oxygen-vacancy concentration, or the formation of suboxide phases.

To correctly distinguish these contributions, studies of $WO_3/MoO_3$ heterostructures should rely on comprehensive phase, valence-state, morphological, and electrochemical characterization, including XRD, Raman spectroscopy, XPS, XANES/EXAFS, EPR, TEM/EELS, and electrochemical impedance spectroscopy. Figure 8 summarizes the sequential evolution of oxide defect structures from stoichiometric $MO_3$ to oxygen vacancies, mixed-valence states, small polarons, and CS suboxides. The lower part of the scheme highlights the dual role of defects. Moderate defect engineering can improve optical modulation, ion insertion, coupled ion–electron transport, and surface reactivity. Excessive reduction, however, increases the risk of irreversible phase degradation, mechanical instability, loss of optical transparency, and deterioration of long-term cycling durability. Thus, defect engineering in $WO_3/MoO_3$ nanocomposite thin films should be regarded as a controlled

balance between functional activation and structural destabilization, rather than as a simple route toward maximizing oxygen-vacancy concentration.

Table 2 summarizes the key defect states governing the behavior of $WO_3$- and $MoO_3$-based oxide systems, including oxygen vacancies ($V_O$), crystallographic-shear suboxides, and W–O–Mo interfacial contacts.

**Table 2.** Defect states in $WO_3$- and $MoO_3$-based oxide systems.

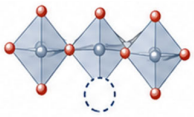
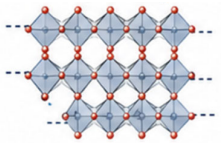
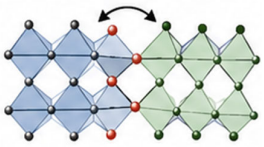
| No | Defect State | Typical Manifestation | Functional Contribution | Associated Risks | Characterization |
|---|---|---|---|---|---|
| 1 | Oxygen vacancies ($V_O$)  | Reduced $W^{5+}/W^{4+}$ or $Mo^{5+}/Mo^{4+}$ centers; local lattice relaxation | Higher electronic conductivity; stronger visible/NIR absorption; enhanced pseudocapacitive response | Excessive reduction; sensitivity to hydration; drift of optical and electrochemical properties | XPS; Raman spectroscopy; EPR; UV–Vis–NIR spectroscopy; EIS |
| 2 | Shear/suboxide phases  | $WO_{3-x}$ and $MoO_{3-x}$ suboxides; CS structures; Magnéli-type phases | Enhanced conductivity; modified redox behavior; altered electrochemical response | Irreversible phase transitions; poor reproducibility; reduced optical transparency | XRD; Raman spectroscopy; HRTEM; XPS; XANES/EXAFS |
| 3 | W–O–Mo interfacial contacts  | Heterointerfaces in mixed, compositionally graded, and multilayer films; charge and vacancy redistribution | Interfacial charge transfer; coupled ion–electron transport; new active sites; possible interfacial synergy | Difficult attribution of effects; metastable interfaces; dependence on composition and phase connectivity | STEM-EDS/EELS; TEM; XPS depth profiling; EIS; electrochemical testing |

Table 2 highlights the dual role of defect states in $WO_3/MoO_3$ systems. Oxygen vacancies, mixed-valence centers, and crystallographic-shear suboxides can enhance electronic conductivity, optical absorption, ion insertion, and pseudocapacitive charge storage. However, excessive defect formation may also cause phase instability, loss of transparency, poor cycling durability, and reduced reproducibility. W–O–Mo interfaces are therefore especially important because they can promote charge redistribution, oxygen-vacancy redistribution, and coupled ion–electron transport. Nevertheless, only complementary structural, valence-state, morphological, and electrochemical characterization can support an interpretation of these effects as true interfacial synergy. Relevant methods include XRD, Raman spectroscopy, XPS, XANES/EXAFS, EPR, TEM/EELS, and EIS [14,47–49,51–53].

### *2.3. W–O–Mo Interfaces: Composition, Charge Transport, and Interfacial Synergy*

In $WO_3/MoO_3$ heterostructures, the heterointerface acts as an active functional region rather than a passive physical contact [14,54,55]. The intimate coupling between the two oxides promotes equilibration of their electrochemical potentials, which can induce interfacial charge redistribution, local band bending, modulation of oxygen-vacancy concentration, and the emergence of an internal electric field. In photocatalysis, such interfacial effects are crucial for promoting electron–hole separation. In electrochromic devices, they can govern the kinetics of coupled electron–cation injection. In gas sensors, they can modulate the depletion-layer width and the density of chemisorbed oxygen species.

Compositionally graded $WO_3/MoO_3$ thin films are of particular interest for analyzing W–O–Mo interfaces, because they allow the W/Mo ratio, coating thickness, and degree of interfacial interaction to be systematically varied within a single substrate. This

architecture makes it possible to directly correlate the local film composition with its optical or electrochemical response and, therefore, to distinguish composition-driven effects from those associated with thickness, morphology, phase connectivity, and defect distribution. Figure 9a compares the Mo content determined by two independent methods: spectroscopic ellipsometry (SE) and Rutherford backscattering spectrometry (RBS). Such cross-validation is essential for reliable analysis of charge transport, interfacial synergy, and functional response. Conclusions should be based on the measured spatial distribution of Mo within the film rather than on the nominal composition of the target or precursor mixture [14].

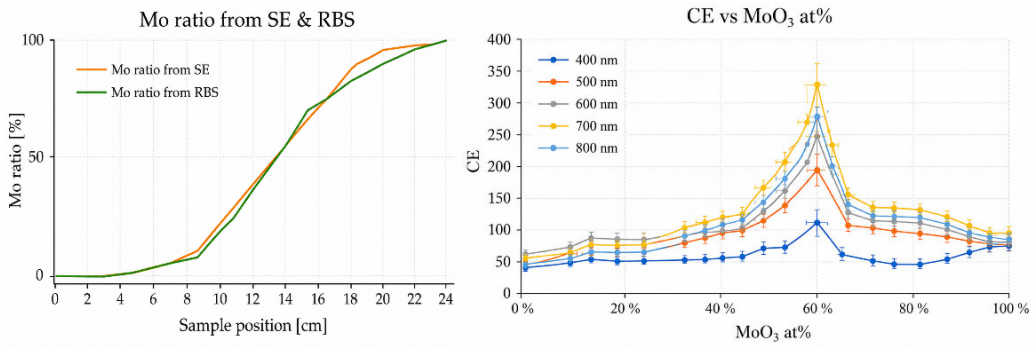



**Figure 9.** Compositionally graded $WO_3/MoO_3$ thin films: validation of Mo-content distribution and its effect on coloration efficiency: (**a**) verification of the Mo content in a compositionally graded $WO_3/MoO_3$ thin film using spectroscopic ellipsometry (SE) and Rutherford backscattering spectrometry (RBS); (**b**) coloration efficiency (CE) as a function of $MoO_3$ atomic fraction in mixed $WO_3/MoO_3$ thin films with different thicknesses. Reproduced from [14] (MDPI, CC BY 4.0).

In this sense, compositionally graded $WO_3/MoO_3$ films provide a powerful model platform for separating genuine interfacial effects from apparent performance changes caused by variations in film thickness, morphology, or phase composition.

The coloration efficiency of $WO_3/MoO_3$ thin films further demonstrates that the maximum functional response is not necessarily achieved at the limiting compositions corresponding to pure $WO_3$ or pure $MoO_3$. Figure 9b shows the dependence of coloration efficiency on the $MoO_3$ content in the film at different wavelengths in the 400–800 nm range. The most pronounced maximum is observed at an intermediate composition, close to approximately 60 at.% $MoO_3$, indicating the existence of an optimal W/Mo ratio for the electrochromic response. This maximum cannot be explained by a simple additive combination of the individual properties of the two oxides. It most likely reflects the combined effects of local composition, film thickness, phase state, oxygen-defect concentration, and W–O–Mo interface formation. Therefore, composition is more than a chemical parameter in the analysis of $WO_3/MoO_3$ systems. It is also a key factor governing interfacial connectivity, coupled ion–electron transport, and the efficiency of optical modulation [14].

In $WO_3/MoO_3$ heterostructures, the interfacial region is important not only as a zone of charge redistribution, but also as a domain where coupled ion–electron transport pathways can be formed. For electrochromic and pseudocapacitive thin films, the functional response depends on electronic-level alignment and the W/Mo oxidation states. It also depends on the accessibility of reversible insertion and extraction channels for small cations such as $H^+$, $Li^+$, $Na^+$, and $K^+$. In this regard, $WO_3$ can be regarded as a relatively stable three-dimensional framework for reversible ion insertion, whereas $MoO_3$ is more effectively introduced as a thin layer, nanodomain, compositionally graded region, or interfacial modifier. This design strategy exploits the layered nature of $MoO_3$ and additional $Mo^{6+}/Mo^{5+}$

redox centers while limiting deep irreversible intercalation and the associated structural deformation. A similar principle is realized in $WO_3/MoO_3$ nanohybrid electrodes, where short diffusion lengths, a large interfacial area, and shortened charge-transfer pathways contribute to an improved pseudocapacitive response [56]. The functional advantage of $WO_3/MoO_3$ architectures therefore does not arise from combining two redox-active oxides alone. It depends on controlling the spatial distribution of $MoO_3$ to enhance interfacial charge transfer and reversible ion transport while avoiding deep structural degradation.

However, the interpretation of transport effects in $WO_3/MoO_3$ composites requires caution, because pronounced changes in the electrochemical response may also arise in other $WO_3$-based heterostructures. Figure 10 shows scan-rate-dependent cyclic voltammograms of WTi-1, WTi-5, and WTi-10 $WO_3/TiO_2$ heterostructured thin films [57]. The increase in current density with increasing scan rate indicates active ion–electron transport and redox participation within the films. Among the presented samples, WTi-5 exhibits the strongest current response and the largest enclosed CV area, suggesting a more favorable balance between electroactive $WO_3$ domains, $TiO_2$ modification, morphology, and charge-transport pathways. In contrast, the lower response of WTi-10 indicates that excessive modification may reduce electrochemical accessibility or hinder charge transport. These results illustrate that variations in CV shape, current density, and apparent capacitance can originate from film architecture, grain structure, porosity, thickness, phase composition, and defect state, rather than from interfacial synergy alone.

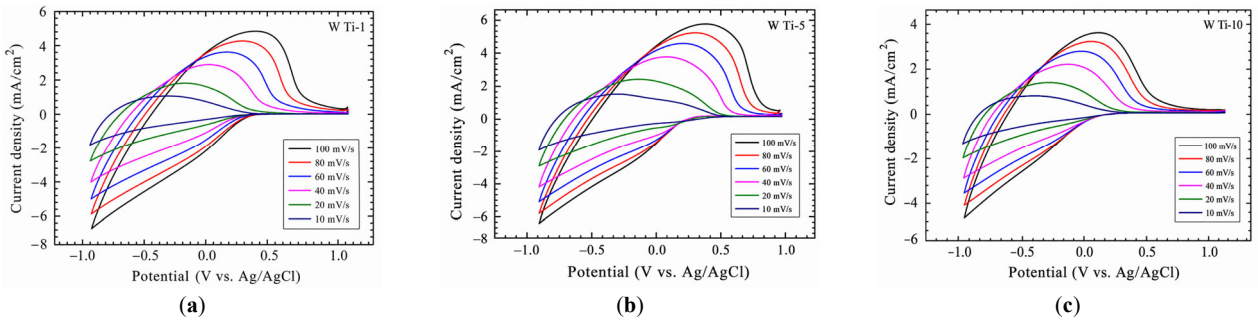



**Figure 10.** Scan-rate-dependent cyclic voltammograms of $WO_3/TiO_2$ heterostructured thin films: (**a**) WTi-1, (**b**) WTi-5, and (**c**) WTi-10 recorded at scan rates from 10 to 100 mV $s^{-1}$ in the potential range from −1.0 to +1.0 V vs. Ag/AgCl. Reproduced from [57] (MDPI, CC BY 4.0).

When analyzing $WO_3/MoO_3$ systems, an increase in current or capacitance should be considered evidence of improved coupled ion–electron transport only after electrochemical data have been correlated with morphological, phase, and valence-state characterization. Enhanced electrochemical response in $WO_3/MoO_3$ architectures should not be assigned to interfacial synergy solely from CV behavior. Independent structural and chemical evidence must confirm the formation and functional role of W–O–Mo interfaces [57].

Figure 11 presents a qualitative scheme of band alignment and transport processes at the W–O–Mo interface in $WO_3/MoO_3$ heterostructures. The band alignment shown in Figure 11 should be regarded as preparation-specific rather than universal. In particular, the electronic levels of $MoO_3$ depend strongly on the crystallographic polymorph, crystallographic orientation, oxygen stoichiometry, hydration state, and interfacial termination. Combined VB-XPS and DFT analyses showed that the valence-band edge of $\alpha$-$MoO_3$ is approximately 0.9 and 1.0 eV higher, respectively, than that of $\beta$-$MoO_3$, whereas the conduction-band edges of these two phases remain close to −2.5 eV [58]. Phase-dependent band structures and work functions have also been demonstrated for polymorphic molybdenum oxides [59]. Metastable h-$MoO_3$ possesses a structurally distinct framework, and its band-edge positions therefore cannot be assigned from those of $\alpha$- or $\beta$-$MoO_3$ with-

out direct characterization [60]. Moreover, oxygen vacancies generate Mo 4d-derived polaronic states and progressively transform the electronic and structural properties of $MoO_{3-x}$ [61,62]. For one specifically prepared monoclinic $WO_3$/defect-rich $MoO_{3-x}$ heterostructure, Mott–Schottky and optical analyses yielded CBE/VBE values of 0.43/3.08 V versus RHE for $WO_3$ and 0.15/3.05 V versus RHE for $MoO_{3-x}$. These values correspond to approximate CBO and VBO magnitudes of 0.28 and 0.03 eV, respectively, and support type-II alignment only for that particular architecture [63]. Accordingly, reliable band-offset assignment requires phase- and stoichiometry-resolved UPS/XPS measurements or geometry-matched first-principles interface calculations.

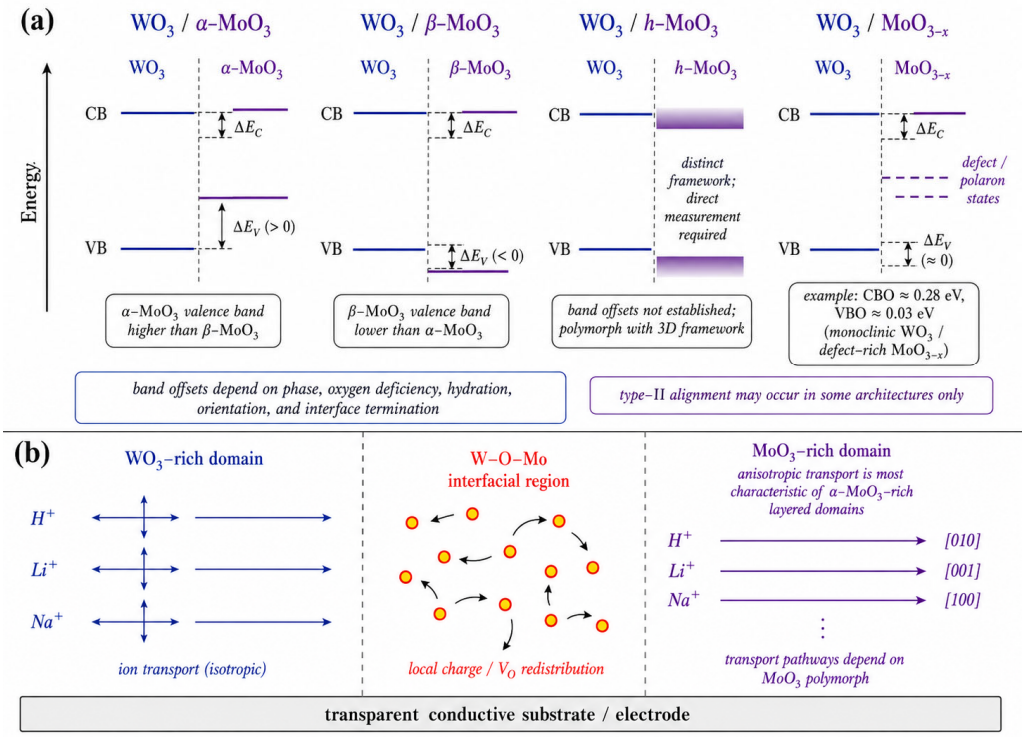



**Figure 11.** Preparation-dependent electronic structure and coupled ion–electron transport in $WO_3/MoO_3$ heterostructures: (**a**) qualitative band-alignment schemes for $WO_3$ interfaced with α-$MoO_3$, β-$MoO_3$, h-$MoO_3$, and oxygen-deficient $MoO_{3-x}$, illustrating the dependence of the conduction- and valence-band offsets on $MoO_3$ polymorph and oxygen stoichiometry; the experimentally derived CBO ≈ 0.28 eV and VBO ≈ 0.03 eV for monoclinic $WO_3$/defect-rich $MoO_{3-x}$ are shown only as a preparation-specific example [63]; (**b**) schematic representation of coupled ion transport and oxygen-vacancy/charge redistribution across $WO_3$-rich domains, the W–O–Mo interfacial region, and $MoO_3$-rich domains.

When favorable offsets are realized, interfacial charge redistribution and local band bending can assist carrier separation. At the same time, the W–O–Mo interfacial region may undergo oxygen-vacancy redistribution, thereby modifying the local defect structure and facilitating coupled ion–electron transport pathways. In this architecture, $WO_3$-rich domains provide predominantly isotropic pathways for the insertion of small cations. By contrast, anisotropic ion transport is most characteristic of α-$MoO_3$-rich layered domains, whereas transport in β-$MoO_3$, h-$MoO_3$, or $MoO_{3-x}$—containing regions may differ because of their distinct structures and defect states. Thus, the functional behavior of $WO_3/MoO_3$ heterostructures does not arise from simple mixing of the two oxides. Instead, it requires coordinated control of band alignment, composition, oxygen-defect chemistry, phase connectivity, and the spatial organization of the W–O–Mo interface.

Thus, W–O–Mo interfaces in $WO_3/MoO_3$ heterostructures should be regarded as active regions in which composition, defect chemistry, oxidation states, and phase connectivity jointly determine the electronic structure and coupled ion–electron transport. However, band alignment in these systems cannot be reduced to a single universal type-I or type-II scheme. Instead, it depends strongly on oxygen nonstoichiometry, Mo content, hydration degree, phase state, layer thickness, substrate effects, and thermal-treatment conditions. Therefore, the specific interfacial scenario must be experimentally verified using XPS/UPS, Mott–Schottky analysis, photocurrent measurements, electrochemical impedance spectroscopy, and valence-state characterization [64].

Interfacial synergy in $WO_3/MoO_3$ systems is not an automatic consequence of mixing two oxides. Enhanced electrochromic efficiency, photocatalytic activity, or pseudocapacitive response may originate not only from W–O–Mo interfaces, but also from changes in porosity, thickness, phase composition, hydration, or oxygen-vacancy concentration. Therefore, true synergy can only be demonstrated by correlating composition, structure, W/Mo oxidation states, the presence of interfacial W–O–Mo contacts, and transport–functional response within the same series of samples. Consequently, high-performance $WO_3/MoO_3$ composite films should be designed as interface-engineered systems. Optimization should address the W/Mo ratio, phase connectivity, defect density, interfacial stability, and accessible ion–electron transport pathways. This conclusion leads directly to the next section. The synthesis method determines film thickness, morphology, porosity, phase composition, defect structure, and the quality of W–O–Mo interfaces.

### *2.4. Operational Criterion and Minimum Evidence for Interfacial Synergy*

The rule-of-mixtures approach is commonly used to assess hybrid effects in composite materials [65–68]. On this basis, we introduce a first-order additive null model for evaluating the functional response of $WO_3/MoO_3$ nanocomposite thin films. For a composite containing a $WO_3$ fraction x, the expected additive response is defined as

$$P_{add} = xP_{WO_3} + (1 - x)P_{MoO_3} \quad (2)$$

where $P_{WO_3}$ and $P_{MoO_3}$ are the normalized responses of matched single-phase reference films. The non-additive contribution is then operationally defined as

$$\Delta P_{syn} = P_{obs} - P_{add} \quad (3)$$

where $P_{obs}$ is the experimentally observed response of the $WO_3/MoO_3$ composite or heterostructure. Equations (2) and (3) are used here as a first-order screening framework rather than as a universal mixing law. A positive $\Delta P_{syn}$ value exceeding the combined experimental uncertainty indicates positive non-additivity. However, its attribution to W–O–Mo interfacial synergy additionally requires correlation with an interface-sensitive parameter and the exclusion of differences in thickness, loading, porosity, roughness, hydration, phase composition, and oxygen nonstoichiometry.

A positive $\Delta P_{syn}$ value alone does not establish W–O–Mo interfacial synergy because an apparently non-additive response may also arise from differences in thickness, morphology, porosity, phase composition, hydration, or oxygen-vacancy concentration. Accordingly, four minimum conditions should be met before interfacial synergy is assigned. First, pure-$WO_3$, pure-$MoO_3$, physical-mixture, and heterostructure controls should be prepared using identical substrates, post-heat treatment parameters, and active-material loadings. Second, the functional response should be normalized by active mass, area, or film thickness, as appropriate. Third, phase composition, roughness, porosity, hydration, and oxygen nonstoichiometry should be quantitatively constrained. Finally, at least

one interface-sensitive structural, chemical, electronic, or transport parameter should be measured, or the interfacial density should be systematically varied at fixed composition. Operando characterization substantially strengthens the mechanistic assignment but is not required to satisfy this minimum evidentiary standard. The complete evidence-based validation workflow is summarized in Figure 12.

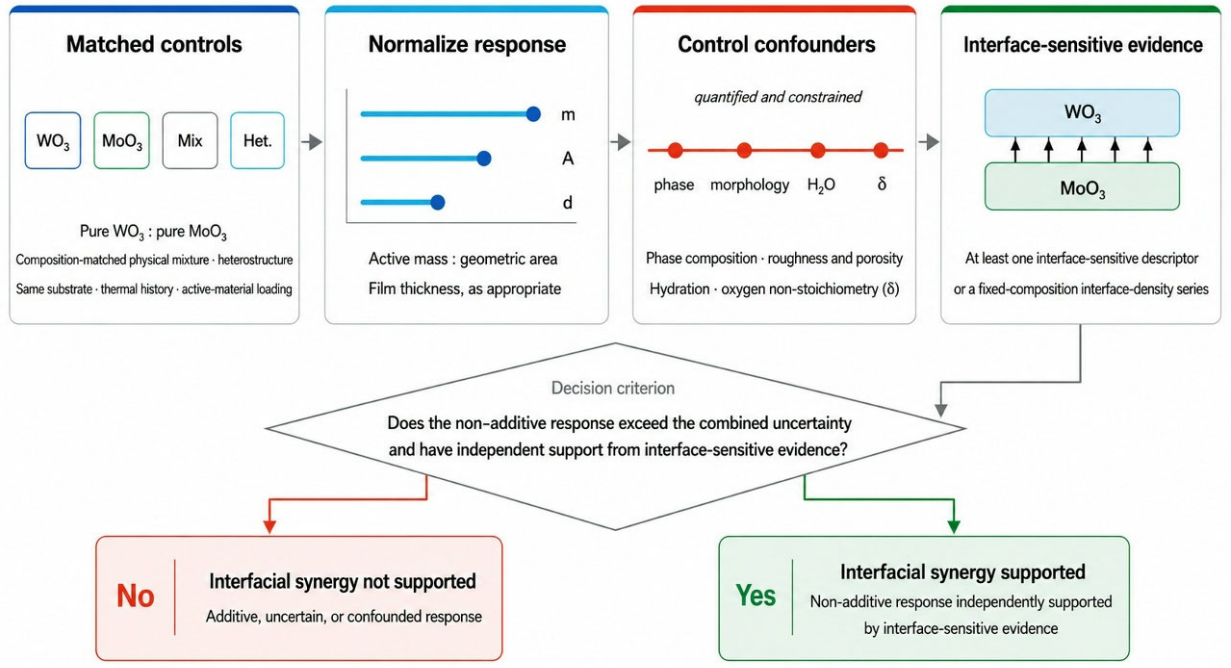



**Figure 12.** Minimum evidence-based workflow for assigning interfacial synergy in $WO_3/MoO_3$ nanocomposite thin films and heterostructures. The arrows indicate the sequential validation pathway from matched reference samples and normalized functional measurements to structural/chemical interface verification and, finally, evidence-supported assignment of genuine W–O–Mo interfacial synergy.

## 3. Synthesis Strategies for $WO_3/MoO_3$ Nanocomposite Thin Films and Heterostructures

The preceding analysis of structural, defect-related, and interfacial factors shows that the synthesis method determines both the coating process and the final thin-film architecture. Depending on the fabrication route, a $WO_3/MoO_3$ film may exist as an atomically mixed oxide, a compositionally graded layer, a nanolaminate, an island-like heterostructure, a porous electrode, or a hybrid film incorporating a conductive matrix. These architectures differ in thickness, phase state, oxygen nonstoichiometry, W/Mo distribution, defect density, and the stability of W–O–Mo interfacial contacts. Therefore, in this section, fabrication methods are considered not merely as technological procedures, but as tools for controlling interfacial architecture, defect chemistry, and coupled ion–electron transport. This perspective makes it possible to distinguish genuine W–O–Mo interfacial synergy from performance improvements caused only by variations in thickness, porosity, secondary phases, or the degree of oxide reduction [14,15].

### *3.1. Fabrication Strategy as a Tool for Engineering the Interfacial Architecture*

Tungsten and molybdenum oxides have been studied individually for several decades. Their nanocomposite combinations, however, have attracted particular attention only recently. The growing interest in these systems arises from the possibility of integrating the three-dimensional $WO_3$ framework with the layered $\alpha$-$MoO_3$ matrix, thereby enabling simultaneous control over oxygen vacancies, coupled ion–electron transport, and pho-

toinduced conductivity modulation within a single heterostructure. This combination of mechanisms has opened a new research direction involving $MoO_3/WO_3$ heterojunctions for ultralow-power optoelectronic synaptic elements and neuromorphic devices. Although this field should still be regarded as an emerging application area, recent studies on artificial synapses based on $MoO_3/WO_3$ heterostructures already demonstrate its feasibility [55]. For this review, these results show that the W–O–Mo interface extends beyond electrochromic, sensing, and photocatalytic applications. It can also enable devices whose functional response depends on controlled and reversible conductivity modulation.

For $WO_3/MoO_3$ systems, the choice of fabrication method determines not only the morphology, but also the actual nature of the active phase. The same nominal W:Mo composition may correspond to a dense amorphous mixed oxide, a phase-separated coating, a nanolaminate with sharp interfaces, a compositionally graded layer, or a porous electrode material. Therefore, each fabrication route should be evaluated against four key criteria. These criteria include precise control of the W:Mo ratio and oxygen stoichiometry, reproducibility of W–O–Mo interfaces, and compatibility with the target substrate. Relevant substrates include ITO/FTO, glass, silicon (Si), metals, and flexible polymer supports [15,40,43,64,69–71].

$MoO_3$ incorporation into $WO_3$ is meaningful only when it generates a measurable interfacial effect, including faster coupled ion–electron transport, higher CE, enhanced pseudocapacitive response, improved charge separation, or the emergence of selective adsorption sites. When performance enhancement is governed mainly by porosity, thickness, or surface-area effects, the system should be considered morphologically optimized, rather than genuinely synergistic. Accordingly, Table 3 treats $WO_3/MoO_3$ thin-film fabrication methods as strategies for engineering interfaces, phase composition, and defect chemistry rather than merely as separate deposition techniques.

**Table 3.** Systematization of fabrication methods for $WO_3/MoO_3$ composite thin films and their role in interfacial design.

| Method | Typical Architecture | Parameters | Advantages | Limitations/Risks | Target Applications | Ref. |
|---|---|---|---|---|---|---|
| Sol–gel, spin coating/dip coating | Mixed oxides, Mo-doped $WO_3$, porous coatings | Precursor composition, pH, viscosity, deposition speed, annealing | Low cost, large-area processing, compatibility with glass and ITO/FTO | Hydration, shrinkage, cracking, residual organic phases | Electrochromic coatings, photocatalysis, gas sensors | [16,35,72,73] |
| Spray coating/spray pyrolysis | Mesoporous coatings, graded layers, oxide mixtures | Substrate temperature, aerosol flow rate, droplet size | Scalability and simple thickness tuning | Inhomogeneity, roughness, complicated phase control | Sensing, photocatalysis, protective coatings | [74] |
| Hydrothermal/ solvothermal synthesis | Nanosheets, nanorods, $MoO_3$ ribbons, 3D structures | Temperature, pressure, mineralizer, growth time | Control over crystallinity and high surface area | Difficult transfer to uniform thin films | Photocatalysis, gas sensors, pseudocapacitive electrodes | [64,70] |
| Electrodeposition/ anodization | Hydrated $WO_3/MoO_{3-x}$ layers, Mo-modified $WO_3$ photoanodes | Potential, current, pH, peroxo-complex concentration, deposition charge | Low-temperature processing, direct growth on conductive substrates | Limited to conductive substrates; sensitivity to pH and electrolyte composition | Electrochromics, flexible electrodes, supercapacitors | [57,64,65] |

**Table 3.** *Cont.*

| Method | Typical Architecture | Parameters | Advantages | Limitations/Risks | Target Applications | Ref. |
|---|---|---|---|---|---|---|
| Reactive magnetron sputtering | Atomically mixed oxides, W:Mo gradients, multilayer coatings | Power applied to W/Mo targets, $O_2$/Ar ratio, pressure, substrate position | Reproducibility, clean films, composition-property mapping | Vacuum processing, cost, risk of hidden phase inhomogeneity | Smart windows, organic electronics, sensors | [14,15,66] |
| ALD/CVD | Nanolaminates, ultrathin interfaces, conformal layers | Number of cycles, precursors, temperature, oxidant/plasma | Sub-nanometer control and high conformality | Slow growth, expensive precursors, narrow temperature window | Microelectronics, supercapacitors, buffer layers | [56,75–77] |
| PLD, e-beam evaporation, and thermal evaporation | Dense layers, model heterostructures, nonequilibrium phases | Beam/laser energy, $O_2$ pressure, substrate temperature | High purity and possibility of stabilizing nonstoichiometry | Limited area, particulates/droplets in PLD, difficult scaling | Fundamental studies, model interfaces | [71] |

Overall, no single method is universal. The optimal route must be selected according to the target architecture and application. To complement the method-by-method comparison in Table 3, Figure 13 presents a qualitative decision matrix for selecting fabrication routes for $WO_3/MoO_3$ thin films. The methods are compared using six practically relevant criteria: thickness control, large-area compatibility, processing cost, compatibility with low-temperature substrates, porosity and texture tunability, and interface cleanliness. The matrix highlights the trade-off between scalable, low-cost processing and precise interfacial control, supporting the development of hybrid fabrication strategies. The scores are comparative and should not be interpreted as universal quantitative rankings.

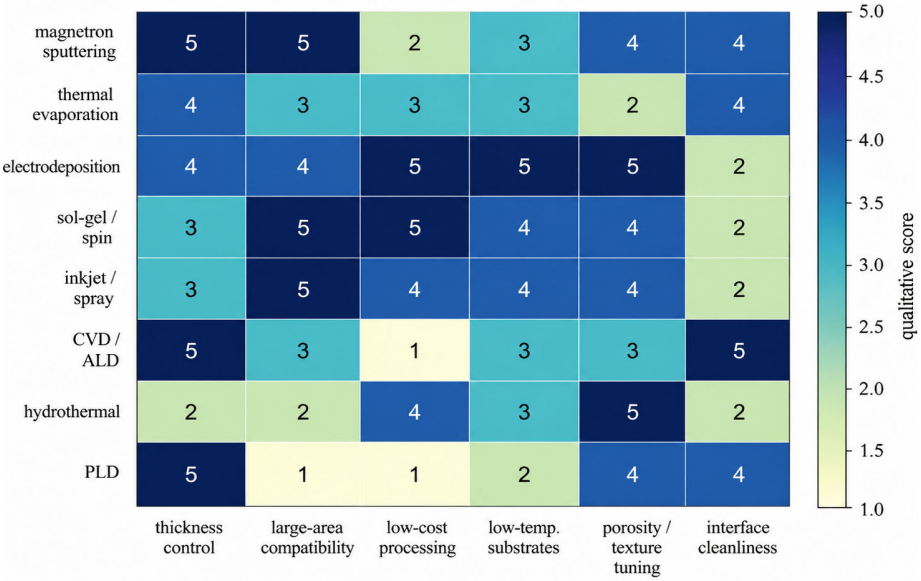



**Figure 13.** Qualitative decision matrix for selecting fabrication routes for $WO_3/MoO_3$ thin films. Fabrication-route decision matrix for $WO_3/MoO_3$ films (scores: 1–5; 5 = favorable).

A technically feasible approach is a two-stage, interface-selective process. First, the bulk $WO_3/MoO_3$ layer is deposited by scalable reactive co-sputtering, spray/slot-die coating, or electrodeposition. A limited number of spatial ALD/PEALD cycles then form conformal

W–O–Mo junctions, followed by mild oxidative annealing. This confines the costly self-limiting process to the nanoscale interfacial region while preserving high throughput. Spray coating has enabled ultrathin W–Mo oxide films from aqueous nanoparticle inks [66], whereas ALD has produced wafer-scale $WO_3$–$MoO_3$ heterostructures below 10 nm [57]. Scale-up should be benchmarked using equal-loading controls, in-line thickness, composition, and sheet-resistance monitoring, process yield, and cost per unit area. Most importantly, improved performance should be attributed to true W–O–Mo interfacial synergy only when synthesis conditions, W/Mo distribution, oxygen stoichiometry, phase connectivity, defect structure, and functional response are correlated within the same sample series.

### *3.2. Vacuum Deposition Methods*

#### 3.2.1. Reactive Magnetron Sputtering

Reactive magnetron sputtering (RMS) is one of the most versatile and reproducible methods for establishing composition–structure–property relationships in the $WO_3/MoO_3$ system. When separate W and Mo targets are used together with a controlled $Ar/O_2$ plasma, a continuous composition gradient can be generated within a single substrate. This combinatorial strategy greatly accelerates the search for the optimal W:Mo ratio and enables direct correlation of local film thickness, composition, and optical response without the need to fabricate a large series of individual samples [14,15]. In RMS, the W:Mo ratio can be finely tuned by adjusting the power applied to each target. The oxygen partial pressure controls the oxidation state and oxygen stoichiometry of the deposited oxide, from substoichiometric $WO_x/MoO_x$ phases to nearly stoichiometric $WO_3/MoO_3$. Compared with sol–gel processing or conventional CVD routes, this method provides higher reproducibility of composition and cleaner control over film architecture. This combinatorial approach is particularly important for $WO_3/MoO_3$ thin films. Their maximum functional response is often observed at intermediate compositions rather than at the limiting states corresponding to pure $WO_3$ or pure $MoO_3$. Nevertheless, the deposited-film composition must be independently verified, for example by SE/RBS analysis. Nominal target parameters do not always reproduce the actual spatial distribution of W and Mo within the coating.

Figure 14 presents a cross-sectional schematic of the RMS chamber used for $WO_3/MoO_3$ thin-film deposition. Two magnetron targets, W and Mo, are positioned inside the chamber and directed toward a glass substrate, with a target-to-target separation of 700 mm. The simultaneous supply of Ar and $O_2$, combined with vacuum pumping, creates a controlled reactive plasma environment for oxide-film growth. By independently adjusting the power applied to each target, this configuration allows the fabrication of mixed, compositionally graded, or multilayer $WO_3/MoO_3$ coatings with controlled W/Mo distribution and tunable interfacial architecture.

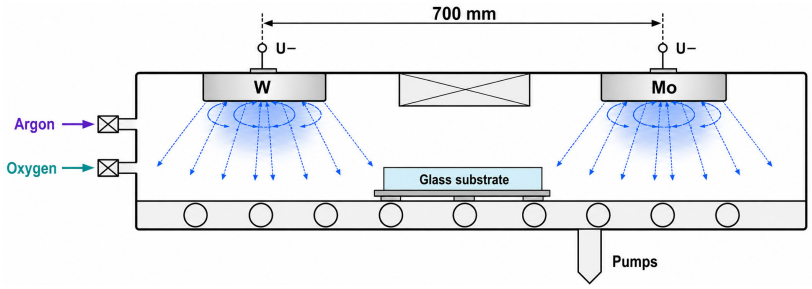



**Figure 14.** Cross-sectional schematic view of the sputtering chamber and W/Mo target arrangement used for combinatorial RMS of $WO_3$–$MoO_3$ thin films. The W and Mo targets are separated by 700 mm and positioned above a glass substrate, while Ar and $O_2$ gas inlets and vacuum pumping provide a controlled reactive atmosphere for oxide-film deposition. Reproduced from [15] (MDPI, CC BY 4.0).

#### 3.2.2. Pulsed Laser Deposition (PLD), Electron-Beam Evaporation, and Thermal Evaporation

PLD, electron-beam evaporation, and thermal evaporation are primarily suitable for fabricating dense layers, model heterostructures, and nanolaminated architectures. Their main advantages are high deposition purity and the ability to stabilize nonequilibrium states. However, oxygen pressure and subsequent phase diagnostics are critical for $WO_3/MoO_3$ systems. Insufficient oxygen activity may lead to the formation of $WO_{3-x}/MoO_{3-x}$ suboxides, whereas high-temperature annealing can promote crystallization, mechanical stress accumulation, and phase segregation [53,70,75,78]. Therefore, these methods are particularly useful when fundamental interfacial effects need to be studied in a well-controlled architecture. However, their application to scalable electrochromic coatings and sensing films is limited by deposition area, equipment cost, and the need for strict control of oxygen activity.

#### 3.2.3. Atomic Layer Deposition (ALD) and Chemical Vapor Deposition (CVD)

ALD and CVD are particularly important when interface precision is more critical than deposition rate. ALD is based on self-limiting surface reactions and is therefore well suited for fabricating ultrathin $WO_3/MoO_3$ nanolaminates, coating porous frameworks, and forming conformal oxide layers on three-dimensional substrates. In contrast to atomically mixed oxides, where the functional response is governed by the volume distribution of W–O–Mo bonds, nanolaminate architectures are controlled by the density, sharpness, and stability of interfacial boundaries. Decreasing the nanolaminate period increases the number of W–O–Mo interfaces, but also imposes stricter requirements on adhesion, mechanical compatibility, and diffusion stability during subsequent thermal treatment. For $MoO_3$-based layers, precursor chemistry, deposition temperature, and plasma activation are especially important, as they determine whether amorphous $MoO_x$, oriented $\alpha$-$MoO_3$, or partially reduced mixed phases are formed [54,75,76,79].

For $WO_3/MoO_3$ nanolaminates, precursor selection must be evaluated at the supercycle level rather than only for the individual oxides. A suitable precursor must be sufficiently volatile and thermally stable, exhibit self-limiting surface chemistry, and produce volatile reaction by-products; additionally, the Mo and W subcycles must share compatible substrate-temperature ranges, oxidants, plasma conditions, and purge requirements. Otherwise, precursor carry-over, unequal growth per cycle, ligand-derived impurities, interfacial etching, or phase-selective crystallization may convert an intended abrupt W–O–Mo boundary into a compositionally graded or chemically contaminated region. Table 4 summarizes representative precursor chemistries and the minimum controls required to assess their compatibility in $WO_3/MoO_3$ supercycles.

The comparison shows that no precursor pair can be assumed a priori to yield an abrupt and compositionally uniform $WO_3/MoO_3$ nanolaminate. The classical carbonyl processes have narrow and non-overlapping verified windows: 152–172 °C for $Mo(CO)_6$ and 195–205 °C for $W(CO)_6$. By contrast, $\beta$-diketonate and imido-amidinato routes may require heated delivery and can exhibit phase mixing or incomplete saturation. Imido-amido/$O_2$-plasma chemistries offer a broader nominal temperature overlap, but the Mo and W subcycles still require independent calibration because their ligand removal, oxygen deficiency, incubation, and crystallization behavior are not equivalent. Halide chemistry enables low-temperature H:$MoO_x$ deposition but introduces additional concerns associated with chlorine-containing by-products, hydrogen incorporation, and possible interface corrosion. Consequently, reliable nanolaminate fabrication requires saturation testing on cross-nucleation surfaces, thickness-normalized rather than cycle-count-normalized

subcycles, and direct verification of composition and interface abruptness by QCM or in situ ellipsometry, XRR, depth-resolved XPS, and cross-sectional STEM-EDS/EELS.

**Table 4.** Representative Mo- and W-oxide precursor chemistries and their implications for $WO_3/MoO_3$ nanolaminate supercycles.

| Oxide/Precursor–Reactant Pair | Verified Deposition Behavior | Main Risk in a $WO_3/MoO_3$ Supercycle | Required Process and Interface Control | Ref. |
|---|---|---|---|---|
| $MoO_3$: $Mo(CO)_6$ + $O_3/H_2O$ | Self-limiting $MoO_3$ growth was reported at 152–172 °C. Above this narrow interval, thermal decomposition of the carbonyl precursor becomes increasingly important | The verified Mo window does not overlap the classical $W(CO)_6/O_3$ window. Carbonyl decomposition, delivery instability and ligand-derived carbon can broaden or chemically grade the nominal interface | Independent saturation and decomposition tests for each half-cycle; QCM or in situ ellipsometry; carbon-sensitive XPS; precursor-line temperature and dose-repeatability monitoring | [80] |
| $MoO_3/MoO_x$: $MoO_2(acac)_2$, $Mo(OiPr)_4$ or bis(ethylbenzene)Mo + $H_2O$ (comparative screening) | Comparative QCM screening found useful linear growth only for $Mo(OiPr)_4$ and bis(ethylbenzene)Mo; the latter showed a 135–150 °C window and ~0.08 Å $cycle^{-1}$. $MoO_2(acac)_2$ did not yield a practical ALD process under the tested conditions | Low volatility and weak surface reactivity can require long dosing, produce very low growth per cycle, increase precursor carry-over and make the Mo subcycle highly sensitive to surface termination. Calcination may also alter a previously deposited $WO_3$ layer | Report bubbler and delivery-line temperatures, dose and purge lengths, QCM saturation curves and post-calcination composition. Verify carbon and depth-dependent Mo loading rather than assuming $\beta$-diketonate transferability | [81] |
| $MoO_3/MoO_x$: $MoO_2(thd)_2$ + $O_3$ | Uniform and conformal growth was demonstrated at 200–275 °C. The as-deposited films can contain $\alpha$-$MoO_3$, $\beta$-$MoO_3$ and substoichiometric $MoO_x$ in condition-dependent proportions | Although the temperature range is compatible with some W processes, phase mixing, surface roughness and partial precursor decomposition can obscure the chemical abruptness of ultrathin nanolaminates | Pulse/purge saturation, GPC and roughness mapping; XRD/Raman phase analysis; XPS or ERDA impurity quantification; cross-sectional STEM-EELS for intermixing | [82] |
| $MoO_x$: $(N^tBu)_2(NMe_2)_2Mo$ + $O_2$ plasma | PEALD was demonstrated over 50–350 °C, generally yielding slightly oxygen-deficient $MoO_x$. Precursor delivery and thermal history strongly affect nucleation, density and crystallization; boosted delivery can favor oriented $\alpha$-$MoO_3$ at high temperature | Plasma exposure, unequal radical recombination and precursor-delivery transients can alter oxygen deficiency and phase selection from one nanolaminate period to the next. Nitrogen/carbon residues and plasma damage must be excluded | Match plasma power, exposure geometry and purge time between Mo and W subcycles; map GPC, density and O/Mo ratio; analyze C/N by XPS or ERDA and phase by XRD/GIXRD | [83,84] |
| H:$MoO_x$: $MoCl_5$ + $H_2O$ | Low-temperature ALD below 150 °C has been used to deposit hydrogenated $MoO_x$, with deposition temperature controlling hydrogenation, work function and electrical behavior | The halide chemistry introduces possible Cl retention and corrosive HCl-containing by-products, while incorporated H changes the electronic state. These effects may chemically modify the underlying $WO_3$ and shift band alignment | Quantify Cl and H, work function and Mo valence; verify reactor and substrate compatibility; use extended purging and examine interfacial corrosion or etching by depth-resolved XPS/TEM | [85] |
| $WO_3$: $W(CO)_6$ + $O_3$ | A narrow $WO_3$ ALD window of 195–205 °C with a saturated growth rate of approximately 0.21 Å $cycle^{-1}$ was reported | The window lies above the $Mo(CO)_6$ window; a nominal carbonyl–carbonyl supercycle therefore lacks a demonstrated common temperature window. Different decomposition and crystallization behavior can generate roughness and composition gradients | Demonstrate a genuine common window experimentally or deposit the oxides in spatially separated zones. Use QCM/FTIR saturation tests, carbon XPS and equal-thickness controls | [86] |

**Table 4.** *Cont.*

| Oxide/Precursor–Reactant Pair | Verified Deposition Behavior | Main Risk in a $WO_3/MoO_3$ Supercycle | Required Process and Interface Control | Ref. |
|---|---|---|---|---|
| $WO_3$: $(^tBuN)_2(Me_2N)_2W$ + $O_2$ plasma | PEALD $WO_3$ growth was demonstrated over 100–400 °C. The broad range overlaps the Mo imido-amido/$O_2$-plasma process and is therefore attractive for paired supercycles | A nominally overlapping temperature range does not ensure matched surface chemistry: the Mo and W precursors can have different saturation doses, ligand removal, oxygen deficiency and crystallization thresholds | Calibrate both half-cycles on the same starting surfaces; match radical dose and substrate temperature; compare GPC and incubation; quantify W/Mo, O/M and C/N depth profiles | [87] |
| Matched Mo/W bis(tert-butylimido)-bis(N,N′-diisopropylacet--amidinato) precursors + $O_3$ | Both oxides were deposited near 300 °C using chemically analogous precursors. W growth was saturative (~0.45 Å cycle$^{-1}$), whereas Mo showed high growth (up to ~2 Å cycle$^{-1}$) but incompletely saturative surface reactions and stronger phase sensitivity | Even chemically matched precursor families can generate unequal GPC, non-equivalent ligand removal and dissimilar crystallization, producing composition and roughness gradients across short-period nanolaminates | Determine saturation separately for each oxide and for cross-nucleation surfaces; normalize subcycle thickness, not merely cycle count; verify interface sharpness by XPS depth profiling, XRR and STEM-EDS/EELS | [88] |

Hybrid architectures further expand the functionality of $WO_3/MoO_3$ systems beyond binary oxide films. The incorporation of reduced graphene oxide (rGO), carbon nanotubes (CNTs), or conductive nanoparticles can compensate for the intrinsically low electronic conductivity of $MoO_3$ and accelerate pseudocapacitive processes. In gasochromic, photocatalytic, and transparent-electrode systems, additional components such as Pd, Pt, Ag, $TiO_2$, ZnO, or carbon phases may also be introduced. However, their contribution must be clearly distinguished from genuine W–O–Mo interfacial synergy [89–91].

### *3.3. Solution-Based Fabrication Methods*

Table 5 systematizes the main solution-based and electrochemical approaches used for the fabrication of $WO_3/MoO_3$ composite thin films. For each method, the key processing parameters, typical resulting architectures, and characteristic deposition-related challenges are identified. This comparison provides a practical basis for selecting an appropriate fabrication route depending on the required morphology, scalability, phase/interface control, and substrate-related limitations. In solution-based methods, parameters such as precursor chemistry, solvent composition, pH, viscosity, drying regime, and annealing temperature largely determine film uniformity, porosity, hydration degree, cracking tendency, and residual organic content. In electrochemical approaches, the applied potential or current density, electrolyte composition, pH, peroxo-complex stability, deposition charge, and substrate conductivity directly affect film thickness, oxygen deficiency, hydration state, and accessibility of ion-transport pathways. Accordingly, these methods are not merely low-cost alternatives to vacuum deposition. They are also flexible tools for controlling porosity, surface area, defect concentration, and electrochemically active interfaces in $WO_3/MoO_3$ thin-film architectures. The data summarized in Table 5 show that each fabrication method has a specific set of controllable parameters and associated risks. For example, sol–gel processing and spin coating enable molecular-level mixing of W and Mo components, but are highly sensitive to shrinkage, cracking, hydration, and residual organic species. Hydrothermal synthesis provides highly developed nanostructured surfaces but usually requires an additional transfer or fixation step, during which adhesion and film uniformity become critical. Electrochemical deposition allows film thickness to be precisely controlled through the deposition charge, but is limited to conductive substrates and is sensitive to the electrolyte composition, pH, and molybdenum oxidation state. Therefore, reproducible $WO_3/MoO_3$ composite films require careful reporting and control of all key processing parameters. This requirement includes parameters often omitted from brief experimental descriptions.

**Table 5.** Critical processing parameters of solution-based and electrochemical methods for $WO_3/MoO_3$ composite thin films.

| Method | Formed Structure | Controlled Parameters | Main Risks | Parameters That Must Be Reported |
|---|---|---|---|---|
| Sol–gel + spin coating | Molecularly mixed W/Mo oxides; thin porous layers | Precursor concentration; pH; viscosity; spin speed (rpm); number of coating cycles; annealing regime | Shrinkage; cracking; residual water/organic species; hydration | Precursors; solvent; sol aging time; spin speed; thickness per cycle; annealing regime |
| Dip coating | Uniform coatings over large areas | Withdrawal speed; viscosity; substrate wettability; humidity | Runoff/streaks; thickness gradients; edge effects | Withdrawal speed; atmosphere; humidity; substrate preparation |
| Spray coating/ spray pyrolysis | Mesoporous layers; aerosol-derived mixed oxides; compositionally graded coatings | Substrate temperature; aerosol flow rate; droplet size; nozzle–substrate distance | Surface roughness; compositional inhomogeneity; difficult phase control | Flow rate; nozzle–substrate distance; solvent; substrate temperature; number of passes |
| Hydrothermal/ solvothermal synthesis + transfer | Nanorods; nanosheets; $MoO_3$ ribbons; hierarchical structures | Temperature; pressure; mineralizer; growth time; pH | Poor adhesion; layer inhomogeneity; difficult integration into uniform thin films | Anchoring/transfer method; washing/annealing regime; precursor loading; layer thickness |
| Electrodeposition/ anodization | Hydrated $WO_3/MoO_{3-x}$ layers; porous electrochemically active films | Potential/current; pH; electrolyte composition; deposition charge; electrode geometry | Valence instability of Mo; limitation to conductive substrates; high sensitivity to electrolyte composition | Deposition mode; electrolyte formulation; electrode area; passed charge; pH; temperature; post-treatment |

#### 3.3.1. Sol–Gel Processing and Related Solution-Based Deposition Methods

Sol–gel processing (Figure 15) and related solution-based methods remain among the most accessible routes for fabricating $WO_3/MoO_3$ thin films. These approaches enable W and Mo precursors to be mixed at the molecular level and deposited by spin coating, dip coating, or spray coating. For $WO_3$, commonly used precursors include peroxotungstic, tungstate, and alkoxide-based systems, whereas $MoO_3$ films can be prepared from molybdates, peroxomolybdate complexes, or organosols. After deposition, mild thermal treatment is critical. It removes solvent and organic residues and also determines the hydration state, crystallinity, porosity, and possible formation of substoichiometric oxide regions [35,70,72,73,90].

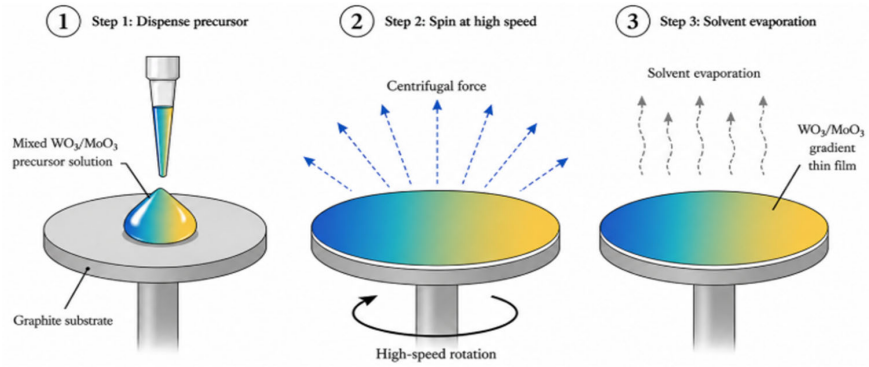



**Figure 15.** Schematic representation of the spin-coating route for $WO_3/MoO_3$ nanocomposite thin-film fabrication from a mixed W/Mo precursor solution.

The chief advantage of solution-based routes is their flexibility. Their key limitation is poor reproducibility. Small variations in pH, humidity, sol aging time, viscosity, or drying rate can lead to different degrees of hydration, shrinkage, cracking, and phase evolution.

For solution-derived $WO_3/MoO_3$ films, performance is governed by the complete chemical and processing history rather than by the nominal deposition method alone. Key variables include precursor composition, solvent system, aging conditions, thickness per coating cycle, annealing temperature, and annealing duration.

Figure 15 schematically illustrates the spin-coating route for fabricating $WO_3/MoO_3$ nanocomposite thin films from a mixed W/Mo precursor solution. The process includes precursor dispensing onto the substrate, high-speed rotation driven by centrifugal forces, solvent evaporation, and thermal treatment, resulting in a mixed or interfacially coupled $WO_3/MoO_3$ oxide architecture. This scheme emphasizes that the final film uniformity, porosity, phase distribution, and degree of W–O–Mo interfacial contact are governed by precursor chemistry, viscosity, rotation speed, solvent evaporation kinetics, wetting behavior, and annealing conditions. The blue-to-yellow gradient schematically represents the spatial variation in the relative W/Mo precursor composition across the coating and is qualitative rather than a calibrated concentration scale; blue arrows indicate centrifugal spreading during spinning, whereas gray dashed arrows indicate solvent evaporation.

Although sol–gel processing is an economically attractive and versatile route, it often suffers from limited thickness control, film nonuniformity, shrinkage-induced defects, and difficulties in ensuring reproducible coating quality.

### 3.3.2. Hydrothermal Methods

Hydrothermal and solvothermal methods typically produce nanostructured active surfaces rather than dense, smooth coatings. These surfaces may comprise nanoribbons, nanorods, nanosheets, or hierarchical assemblies. This approach is particularly effective for $\alpha$-$MoO_3$, whose layered crystal structure provides enhanced accessibility to interlayer spaces and increases the density of surface-active sites. However, when hydrothermally synthesized materials are transferred onto a substrate, adhesion, layer uniformity, and mechanical stability must be carefully controlled [35,64,70].

Figure 16 presents SEM images of $MoO_3$ samples obtained by hydrothermal synthesis using different additives. At the same scale of 500 nm, the micrographs reveal pronounced morphology changes depending on the type and concentration of the additive, ranging from loosely aggregated particles to more ordered nanoribbon- or rod-like structures. This comparison demonstrates that hydrothermal synthesis conditions strongly influence crystallite size, shape, aggregation degree, and surface accessibility, which are critical parameters for optimizing the active surface of $MoO_3$-based and $WO_3/MoO_3$ nanocomposite materials.

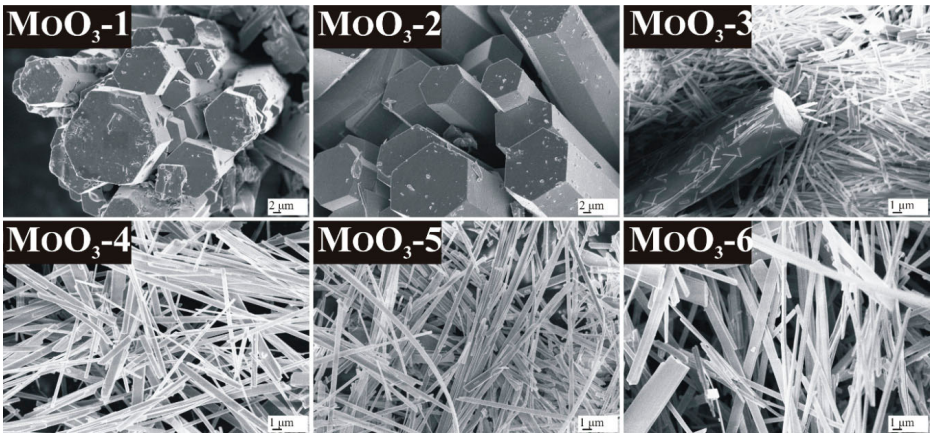



**Figure 16.** SEM images of $MoO_3$ samples obtained by hydrothermal synthesis using different additives. The micrographs illustrate the effect of additive type and concentration on the morphology, size, and aggregation behavior of $MoO_3$ nanostructures. Reproduced from [71] under the terms of the Creative Commons Attribution license (CC BY 4.0).

3.3.3. Electrochemical Methods

Electrochemical deposition, particularly cathodic deposition, and anodization should be considered separately because they provide low-temperature routes for forming hydrated $WO_3$ and Mo-containing oxide layers directly on conductive substrates. Unlike in spin coating, where solution viscosity, rotation speed, and drying conditions mainly govern film thickness, the thickness deposited electrochemically is directly related to the charge passed. The potential, current density, pH, electrolyte composition, and electrode geometry control the morphology. These approaches are especially promising for electrochromic coatings, flexible electrodes, photoanodes, and pseudocapacitive systems, where short diffusion pathways and good electrical contact with the substrate are essential.

Figure 17 shows FE-SEM images of $WO_3$ and $WO_3$–$MoO_3$ nanostructures obtained by electrochemical anodization with a molybdenum-containing additive [69,73,91]. The micrographs reveal a highly developed porous and granular surface morphology rather than a dense compact film. At lower magnification, the coatings exhibit continuous surface coverage with a rough, interconnected nanostructure. At higher magnification, they show fine grains, open pores, and locally aggregated nanoclusters. Such morphology is important because it increases the electrochemically active surface area and facilitates electrolyte penetration, thereby shortening ion-diffusion pathways and improving access to redox-active W/Mo centers.

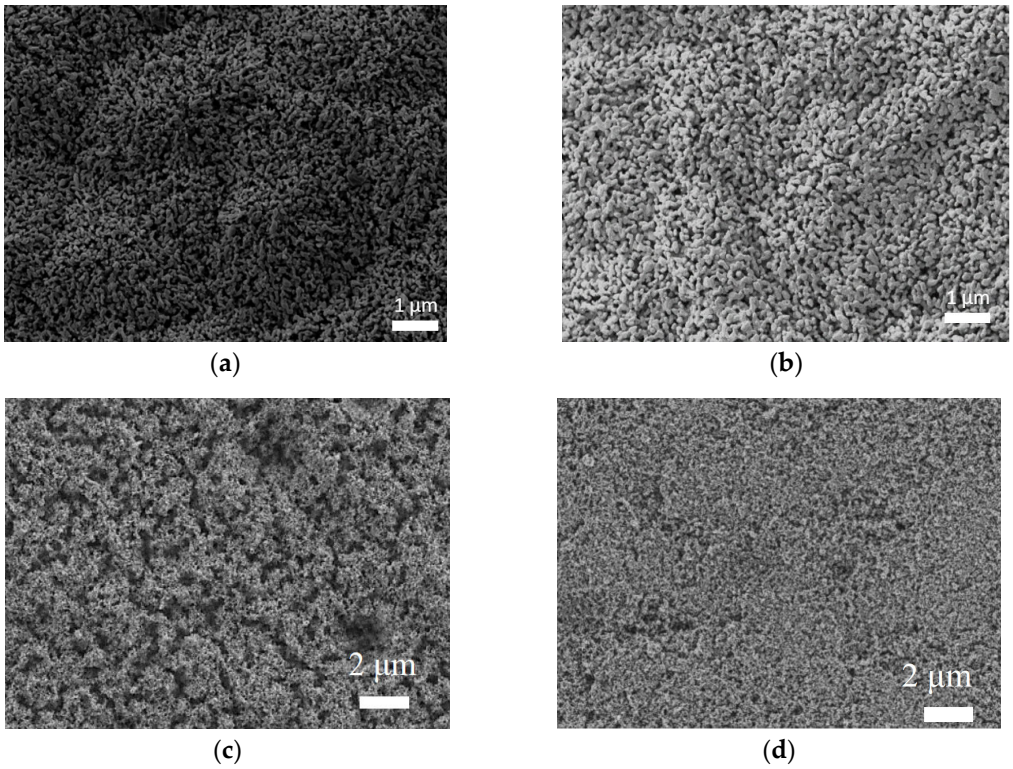



**Figure 17.** FE-SEM images of anodically formed oxide nanostructures: (**a**) $WO_3$, (**b**) $WO_3$ prepared with a 0.01 M molybdate-containing additive, (**c**) $TiO_2$, and (**d**) $TiO_2$ prepared with 0.01 M $Zn(NO_3)_2$. The comparison illustrates the effect of Mo- and Zn-containing additives on the surface morphology of anodically synthesized oxide nanostructures. Reproduced from Ref. [72] under the terms of the Creative Commons Attribution license (CC BY 4.0).

However, comparison of the different panels indicates that the addition of Mo species and variation in the electrochemical regime can substantially change surface porosity, grain size, particle packing, and the degree of structural uniformity. These changes may strongly influence the photocurrent, capacitance, or electrochromic response even with-

out true W–O–Mo interfacial synergy. Therefore, increases in current, capacitance, or photocurrent in such systems should not automatically be attributed solely to W–O–Mo interfacial effects. They must be interpreted by correlating electrochemical data with SEM morphology, XRD/Raman phase analysis, and XPS-based evaluation of W/Mo oxidation states and oxygen-defect concentration. This is especially important for anodized $WO_3$–$MoO_3$ films, where the functional response can arise from a combined contribution of porosity, hydration, oxygen vacancies, Mo-induced surface modification, and interfacial charge-transfer pathways.

### *3.4. Post-Treatment*

Post-treatment should be regarded as a critical and independent stage in the fabrication of $WO_3/MoO_3$ nanocomposite thin films. Annealing, mild reduction, plasma treatment, hydration, or re-oxidation can substantially modify the phase composition, oxygen non-stoichiometry, oxidation states of W and Mo, defect density, and stability of W–O–Mo interfaces. These changes directly affect the functional behavior of the films, including optical modulation, ion insertion, charge transport, sensing response, photocatalytic activity, and pseudocapacitive charge storage [35,40,43,73,89].

The key point is that the optimal post-treatment regime does not necessarily correspond to the highest crystallinity or the maximum concentration of oxygen vacancies. Excessive crystallization may reduce ion-accessible pathways, whereas over-reduction can generate unstable suboxide phases, charge traps, or irreversible optical and electrochemical degradation. Therefore, post-treatment must be optimized according to the intended application rather than treated as a universal final annealing step.

Table 6 summarizes how the choice of fabrication method and post-treatment strategy should be aligned with the target function of the $WO_3/MoO_3$ film. For electrochromic devices, the priorities are high optical modulation and cycling stability. For sensors, surface accessibility and humidity stability are critical. Energy-storage systems require control of ion transport, defect stability, and resistance growth. For photocatalytic or photoelectrochemical systems, phase composition, defect-mediated recombination, and band alignment are decisive. Thus, post-treatment serves as the final tool for balancing crystallinity, defect chemistry, interfacial stability, and functional performance in $WO_3/MoO_3$ thin-film architectures.

Analysis of current fabrication strategies shows that there is no universal method for producing $WO_3/MoO_3$ composite thin films. When reproducible composition mapping and identification of the optimum electrochromic performance are required, RMS is the most rational approach. When porosity, low cost, and scalability are prioritized, solution-based methods are preferable. When short diffusion pathways and strong adhesion to conductive substrates are essential, electrodeposition and anodization are particularly suitable. If the key requirement is the density, sharpness, and stability of interfaces, ALD/CVD and nanolaminate architectures offer clear advantages.

For further discussion of $WO_3/MoO_3$-based devices, it is important to distinguish four major types of systems: atomically mixed oxides, compositionally graded coatings, nanolaminates/heterostructures, and hybrid composites incorporating conductive matrices. This classification makes it possible to link the fabrication route with the dominant functional mechanism and to distinguish genuine W–O–Mo interfacial synergy from apparent performance improvements caused by film thickness, porosity, secondary phases, or different degrees of oxide reduction.

**Table 6.** Selection of synthesis methods for $WO_3/MoO_3$ composite thin films according to target function.

| No | Target Function | Preferred Architecture | Optimal Methods | Parameters | Critical Risk |
|---|---|---|---|---|---|
| 1 | Electrochromic smart windows | Amorphous or weakly crystalline mixed $WO_3/MoO_3$ films; compositionally graded layers | Reactive sputtering; sol–gel/spin coating; electrodeposition | ΔT, coloration efficiency, cycling stability | Ion trapping, residual coloration, loss of transparency |
| 2 | Gas sensors | Porous $WO_3/MoO_3$ surfaces and W–O–Mo heterointerfaces | Spray coating; hydrothermal growth; PVD followed by annealing | Sensitivity, selectivity, response/recovery time, humidity stability | $MoO_3$ hydration, signal drift, humidity interference |
| 3 | Supercapacitors/LIBs | Nanolaminates, porous electrodes, $WO_3/MoO_3$/rGO hybrids | ALD; electrodeposition; hydrothermal synthesis combined with a conductive matrix | Capacitance/capacity, retention, EIS, rate capability | $MoO_3$ volume expansion, increase in resistance |
| 4 | Photocatalysis/PEC | Defective $WO_3/MoO_{3-x}$ heterostructures with controlled band alignment | Anodization; hydrothermal growth; spray coating; CVD | Photocurrent, IPCE, EIS, pollutant degradation | Defect-mediated recombination, photocorrosion |
| 5 | OLEDs/transparent electrodes | Thin $MoO_3$-rich/$WO_3$ interlayers; oxide/metal/oxide stacks | PVD; e-beam evaporation; ALD; multilayer deposition | Transparency, sheet resistance | Work-function shift, metal diffusion, contact instability |

## 4. Functional Devices and Properties of $WO_3/MoO_3$ Nanocomposite Films and Heterostructures

Building on the fabrication strategies discussed in Section 3, Section 4 moves beyond synthesis and addresses how $WO_3/MoO_3$ nanocomposite thin films and heterostructures translate structural complexity into device-relevant functionality. This section does not treat performance as a set of isolated peak values, such as optical modulation, sensitivity, capacitance, photocurrent, or charge-storage capacity. Instead, it emphasizes the mechanistic links among processing history, chemical composition, phase constitution, oxygen nonstoichiometry, defect chemistry, W–O–Mo interfacial coupling, and long-term operational durability. Within this framework, $WO_3/MoO_3$-based architectures are examined as multifunctional, defect- and interface-engineered platforms. Nanoscale heterogeneity is treated as a functional design principle for electrochromic devices, gas sensors, supercapacitors, lithium-ion energy-storage systems, photoelectrochemical cells, transparent electrodes, and organic electronic devices.

### *4.1. Technological Applications of $WO_3/MoO_3$ Nanocomposite Thin Films and Heterostructures*

The principal application areas of $WO_3/MoO_3$-based nanocomposite thin films and heterostructures, summarized in Figure 18, demonstrate the broad multifunctionality of these architectures, spanning electrochromic devices, gas sensors, photocatalysts, supercapacitors, lithium-ion energy-storage systems, transparent electrodes, and organic optoelectronic devices.

$WO_3$ and $MoO_3$ thin films exhibit a broad range of chromogenic effects. Electrochromism involves reversible color and optical modulation under an applied potential. Other responses include UV-induced photochromism, gasochromism in reducing atmospheres such as $H_2$ or $H_2S$, and thermochromism driven by temperature changes [5,7,8,19,20,40,92]. The chromogenic response of $WO_3$ and $MoO_3$ is largely governed by the reversible intercalation and deintercalation of small cations coupled with

electron injection. Under electrochemical polarization, for instance, $H^+$ or $Li^+$ ions enter the oxide lattice together with charge-compensating electrons. This process forms bronze-like phases such as $H_xWO_3$, $Li_xWO_3$, $H_xMoO_3$, or $Li_xMoO_3$. This coupled ion–electron insertion partially reduces $W^{6+}/Mo^{6+}$ to $W^{5+}/W^{4+}$ or $Mo^{5+}/Mo^{4+}$ states. The resulting electronic transitions produce intense blue or dark-blue coloration and pronounced changes in optical absorption [5,7,8,19,20,30,40,77,78,92–97]. In a generalized form, the electrochromic switching mechanism can be represented by the following reaction:

$$MO_3 + x(A^+ + e^-) \rightleftharpoons AxMO_3, \text{ where M = W or Mo; } A^+ = H^+, Li^+, Na^+, \text{ or } K^+ \quad (4)$$

Here, x denotes the degree of intercalation, i.e., the number of inserted cations and charge-compensating electrons per oxide formula unit. In an idealized case involving monovalent cations, x may vary over a relatively broad range. However, in real $WO_3$ and $MoO_3$ electrochromic thin films, the reversible intercalation window is typically much narrower and is limited by the onset of ion trapping, phase transformations, and structural degradation. Therefore, the kinetics and reversibility of reaction (4) critically depend on the crystallinity of the film, the density of oxygen vacancies, and the state of interfacial boundaries. These factors become particularly important when moving from single-phase oxides to nanocomposite and heterostructured architectures [5,14,78].

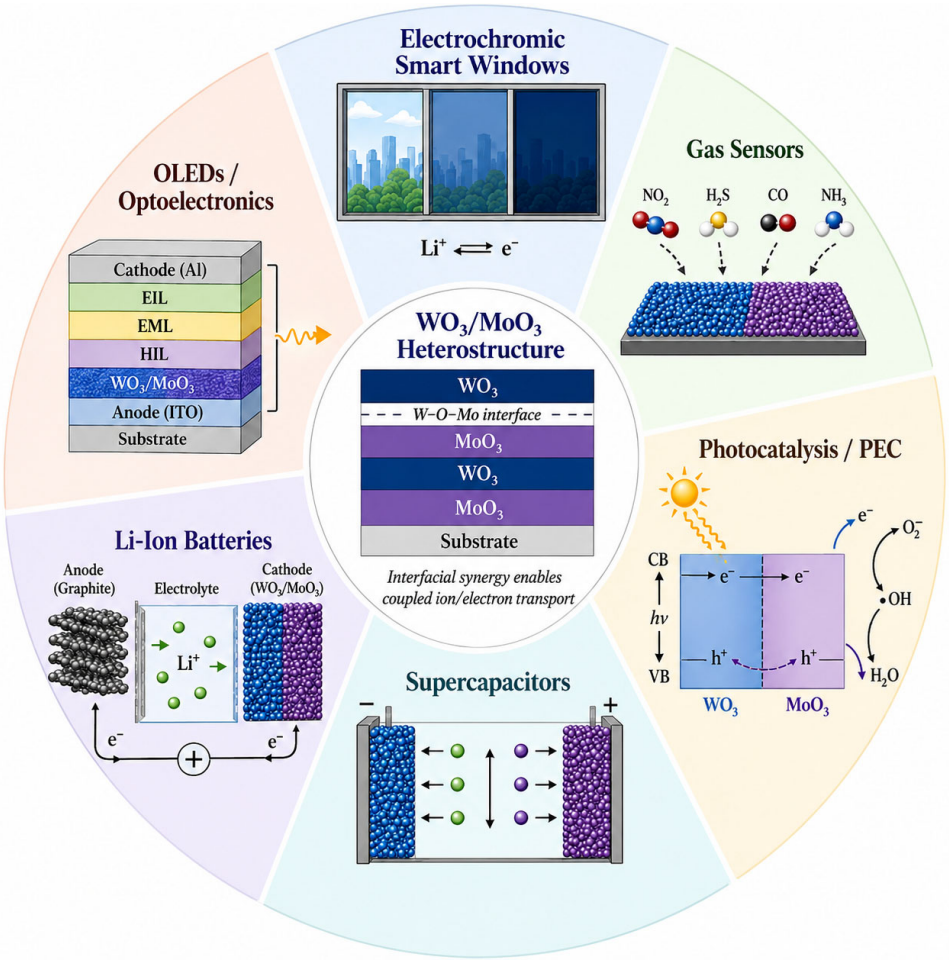



**Figure 18.** Multifunctional application landscape of $WO_3/MoO_3$ nanocomposite thin films and heterostructures.

In this sense, nanocomposite and heterostructured $WO_3/MoO_3$ architectures should not be viewed merely as mixed-oxide systems, but as interfacially engineered materials in

which crystallinity, oxygen-defect chemistry, and W–O–Mo boundary states collectively define the electrochromic response.

### 4.2. From Interface-Engineered $WO_3/MoO_3$ Materials to Functional Device Architectures

The transition from material to device requires identifying the true active region of a $WO_3/MoO_3$ architecture. Depending on the application, this region may correspond to the bulk of the mixed-oxide film, the surface accessible for adsorption and ion insertion, the W–O–Mo interface, oxygen-vacancy-rich domains, or the electrode/electrolyte contact. In electrochromic devices, both the bulk and surface participate in coupled cation–electron transport. In gas sensors, the response is governed mainly by the surface and depletion layer. In supercapacitors, accessible redox centers and ion-transport channels dominate. In photoelectrochemical systems, the active regions generate and separate charge, whereas energetically selective contacts govern optoelectronic devices.

Accordingly, device optimization cannot be reduced to selecting a nominal W:Mo ratio. It requires matching the active-layer geometry, phase constitution, oxygen-vacancy concentration, mixed-valence $W^{5+}/W^{4+}$ and $Mo^{5+}/Mo^{4+}$ states, and the quality of W–O–Mo interfacial contacts to the operating mechanism of each device.

Before discussing specific device classes, it is important to distinguish intrinsic $WO_3/MoO_3$ and Mo–W–O architectures from the broader family of $WO_3$- or $MoO_3$-based composites containing secondary oxides, sulfides, polymers, or carbonaceous phases. Mixed $WO_3$–$MoO_3$ electrochromic films have been studied since the late 1980s [95]. The modern field, however, has shifted from simple W–Mo oxide blending toward deliberate design of $WO_3/MoO_3$ interfaces, gradient coatings, nanolaminates, and defect-engineered Mo–W–O heterostructures. Table 7 summarizes representative architectures in which the functional response is directly associated with the coexistence of W- and Mo-oxide components or with the formation of a mixed Mo–W–O oxide matrix.

Electrochromic coatings and smart windows remain the most established and intensively studied application field for $WO_3/MoO_3$-based architectures. Their performance is primarily governed by the controlled design of W–O–Mo interfaces, porosity, and oxygen-defect chemistry, which together facilitate coupled ion–electron transport and improve switching kinetics. Beyond electrochromics, recent studies demonstrate a clear expansion of $WO_3/MoO_3$ systems toward energy storage, photocatalysis, and neuromorphic optoelectronics, indicating a gradual transition from conventional chromogenic coatings to multifunctional device platforms. Consequently, this functional diversification calls for application-specific design strategies that link interfacial architecture and defect-mediated transport to the dominant electrochemical, catalytic, or optoelectronic process.

**Table 7.** Main $WO_3/MoO_3$ and Mo–W–O architectures, fabrication methods, and device-oriented applications.

| No | Architecture | Fabrication Method | Key Mechanism | Application | Ref. |
|---|---|---|---|---|---|
| 1 | Amorphous $WO_3/MoO_3$ films | Thin-film deposition of an amorphous mixed oxide film | Intervalence charge transfer between W and Mo centers | Electrochromic absorption | [97] |
| 2 | Mo-doped $WO_3/W_{1-y}$ Mo_$yO_3$ | Magnetron sputtering | Mo tunes defect density, conductivity, and spectral response | Electrochromic layers for smart windows | [77,98] |
| 3 | Sol–gel $MoO_3$–$WO_3$ films | Dip-coating from a P123-assisted sol–gel system; annealing | Porous matrix accelerates ion intercalation | Electrochromic coatings on ITO | [16] |
| 4 | $WO_3$–$MoO_3$ nanocomposite films | Cathodic electrodeposition | Coupled $H^+/Li^+$ intercalation; increased active surface area | Electrochromic films | [75] |

**Table 7.** *Cont.*

| No | Architecture | Fabrication Method | Key Mechanism | Application | Ref. |
|---|---|---|---|---|---|
| 5 | $MoO_3/WO_3$ nanocomposite films | Solution processing/dip-coating | $MoO_3$ optimizes surface roughness and ion transport | Electrochromic modulation | [99] |
| 6 | Mixed $MoO_3$–$WO_3$ films | Atmospheric chemical vapor deposition | W–Mo network enhances electron transfer between redox centers | Electrochromic and optoelectronic coatings | [92] |
| 7 | $WO_3/MoO_3$ gradient films | Reactive magnetron co-sputtering | Properties are governed by the W:Mo ratio and film thickness | Optimization of coloration efficiency | [14] |
| 8 | $WO_3/MoO_x$ hybrid films | Chemical/solution-based formation | $MoO_x$ modifies charge balance and switching reversibility | Complementary electrochromic devices | [35] |
| 9 | $MoO_3$–$WO_3$/Ag/$MoO_3$–$WO_3$ | Multilayer oxide/metal/oxide architecture | Ag improves conductivity, while W–Mo oxides preserve transparency and electrochromic response | ITO-free transparent electrodes | [90] |
| 10 | $MoWO_x$/Mo_y$W_{1-y}O_{3-\delta}$ | Solvothermal synthesis followed by film formation | Mixed oxide matrix enables VIS/NIR plasmonic control | Dual-band smart windows | [100] |
| 11 | Ultrathin W–Mo oxide films | Spray-coating from aqueous nanoparticle ink | Porous W–Mo network provides high contrast and fast charge transfer | High-contrast electrochromic coatings | [78] |
| 12 | Mo-doped $WO_3$ nanowires | Hydrothermal growth followed by Mo modification | Increased number of active sites and redox-storage capability | Electrochromic/ energy-storage devices | [30] |
| 13 | Porous W–Mo oxide electrodes | Solution-based formation of porous films | Porous channels facilitate ion and electron transport | Energy-storing smart windows | [101] |
| 14 | $MoO_x$/W–Mo oxide nanowires | Solution-based nanohybridization | $MoO_x$ enhances switching reversibility | Reversible energy-storing smart windows | [102] |
| 15 | $WO_3/MoO_3$ nanoparticulate composite films | Electrodeposition | Increased optical modulation and areal capacitance | Electrochromic energy storage | [94] |
| 16 | $MoO_3/WO_3$ heterojunction | Electron-beam evaporation | Photo- and electrically tunable conductance plasticity | Optoelectronic synapses | [56] |
| 17 | $WO_3$–$MoO_3$ nanohybrid | Atomic layer deposition | High density of W–O–Mo interfaces and short diffusion pathways | Thin-film supercapacitors | [64] |
| 18 | $MoO_3/WO_3$/rGO | Solution/chemical synthesis with rGO | rGO increases conductivity and buffers deformation | Supercapacitors; electrocatalysis | [103] |
| 19 | $WO_3/WO_3$–$MoO_3$ photoanodes | Electrochemical formation of $WO_3$ followed by Mo modification | Mo lowers charge-transfer resistance | Photoelectrocatalysis | [72] |
| 20 | $WO_3/MoO_{3-x}$ heterostructure | Hydrothermal/solvothermal growth of $MoO_{3-x}$ on $WO_3$ | Oxygen vacancies and heterojunction improve $e^-/h^+$ separation | RhB degradation; $H_2$ evolution | [104] |
| 21 | $WO_{3-x}/MoO_{3-x}$ heterostructure | In situ solvothermal reduction | Defective region and vacancy bridges enhance charge separation | $CO_2$ photoreduction | [105] |
| 22 | $WO_3/MoO_{3-x}$ from W–Mo alloy scrap | Oxidative chemical recycling of W–Mo alloy scrap | Mixed W/Mo surface combines adsorption and photocatalysis | Removal of dyes and pollutants | [106] |
| 23 | Combinatorial Mo–W–O libraries | Thermal co-evaporation; combinatorial deposition | Composition-dependent oxide chemistry and surface acidity | Antibacterial films; screening | [107] |
| 24 | Plasmonic Mo–W hybrid oxide | Solvothermal synthesis | LSPR and activation of visible-light charge transfer | Visible-light-enhanced catalysis | [108] |
| 25 | Molybdenum–tungsten oxides | Solvothermal synthesis | The Mo/W ratio determines band structure and charge transfer | Photoelectrochemical water splitting | [109] |

*4.3. Electrochromic Devices and Smart Windows*

Electrochromic devices represent the most established application of $WO_3/MoO_3$-based composites, since both oxides participate in reversible coupled ion–electron processes. $WO_3$ provides pronounced cathodic coloration through the reduction of $W^{6+}$ to $W^{5+}$ and/or $W^{4+}$ during the intercalation of small cations, whereas $MoO_3$ can modulate the work function, defect chemistry, charge transport, and chemical stability of the interface. For $WO_3$- and $WO_3/MoO_3$-based electrochromic films, the key performance parameters are optical modulation, coloration efficiency, switching kinetics, and cycling stability [14,16,22,35,74,77,78,93,94,96–100,110].

The $WO_3/MoO_3$ composition should not be optimized by simply maximizing the content of either component. Combinatorial $WO_3/MoO_3$ thin films show that the highest coloration efficiency is achieved at an intermediate $MoO_3$ content, where interfacial synergy reflects a balance among optical absorption, film thickness, electrical conductivity, and ion-insertion kinetics [14].

A representative example of an interface-oriented strategy is the work of Dong et al. [90]. In that study, an electrochromic device was fabricated without a conventional ITO-based transparent conducting electrode. In the multilayer $MoO_3$–$WO_3/Ag/MoO_3$–$WO_3$ architecture, the thin Ag interlayer provides electrical conductivity, whereas the $MoO_3$–$WO_3$ oxide layers contribute to the electrochromic response, optical transparency, and interfacial stability. This design demonstrates that $WO_3/MoO_3$ composite films can serve not only as active chromogenic materials but also as interface-engineered functional layers, enabling transparency, conductivity, and reversible optical switching to be integrated within a single ITO-free electrochromic device.

Historically, electrochromic smart windows have been the most developed application area for $WO_3$, because dynamic modulation of transmittance in the visible and near-infrared regions enables effective control of light and heat fluxes through facade glazing [5,7,111–113]. Depending on climate, facade orientation, and control strategy, such systems can provide a substantial reduction in building energy consumption. For example, in an office building located in a hot and humid climate, electrochromic glazing was calculated to reduce energy use by 17–23% compared with conventional low-E glazing [112]. For more complex self-regulating electrochromic systems with integrated energy-storage functionality, building-scale calculations for the U.S. office stock indicate considerable potential for electricity savings and $CO_2$-emission reduction. However, such quantitative estimates should be regarded as scenario-dependent values governed by device architecture, climatic zone, operating regime, and the assumed energy-generation model [114].

$WO_3$ is regarded as one of the benchmark cathodic electrochromic materials owing to reversible cation intercalation, stable $W^{6+}/W^{5+}$ redox switching, and pronounced modulation of optical absorption [19]. These features allow $WO_3$ to dynamically tune visible and near-infrared transmittance, which is important for energy-saving glazing, adaptive optical components, optical phase modulators, and optical-memory devices [5,7,8,19,40]. $MoO_3$ also exhibits electrochromic and photochromic behavior. However, its practical use in the pristine state is often limited by low intrinsic electronic conductivity, sluggish charge transport, and increased sensitivity to structural changes during deep ion intercalation [23,24,32,39,44,115]. At the same time, $MoO_3$ provides additional functionality. Its layered structure creates anisotropic ion-transport pathways, and its high work function makes it a valuable charge-selective buffer layer. The surface redox activity of the $Mo^{6+}/Mo^{5+}$ couple also opens opportunities for gas-sensitive coatings, photoactive heterojunctions, supercapacitors, and ion batteries [23,30,78]. Therefore, combining $WO_3$ and $MoO_3$ in nanocomposite films and heterostructures is particularly attractive. This approach

integrates the strong electrochromic response of $WO_3$ with the anisotropic ion transport, high work function, and surface redox activity of $MoO_3$.

In recent years, electrochromic materials have increasingly been considered as both optical modulators and functional components of energy-storage devices. For $WO_3/MoO_3$-based systems, this concept is particularly natural, since the same $H^+/Li^+$ intercalation process that induces optical coloration can also contribute to pseudocapacitive charge storage. In hybrid smart-window devices, therefore, not only the transmittance modulation $\Delta T$ but also the ability of the active layer to store charge without losing optical reversibility becomes technologically important [96,101,102].

However, coupling electrochromism with energy storage imposes more stringent requirements on structural and cycling stability. When the intercalation depth becomes excessive, especially in $MoO_3$-rich regions, the risk of volumetric stress, phase drift, and irreversible ion trapping increases. No universal $MoO_3$ fraction or layer thickness can be prescribed. For dual-function smart windows, the optimum should be reported as a capacity–optical-contrast–cycle-life Pareto front within a reversible electrochromic window. A composition maximizing CE in one film library must not be interpreted as a universal stability limit. Thin $MoO_3$-rich domains, a continuous $WO_3$-rich framework, controlled moderate oxygen deficiency, and charge-limited cycling provide a more transferable design rule than a single atomic-percent threshold.

For this reason, such devices are better served by architectures based on thin $MoO_3$ domains, nanolaminates, gradient coatings, or conductive carbon matrices, which shorten diffusion pathways while simultaneously buffering mechanical deformation. Thus, the optimal $WO_3/MoO_3$ architecture for electrochromic energy-storage windows should not maximize charge insertion, but rather balance optical contrast, reversible charge capacity, ion-transport kinetics, and long-term mechanical integrity.

### *4.4. Gas Sensors*

In parallel with electrochromic technologies, gas-sensing applications of $WO_3$-, $MoO_3$-, and $WO_3/MoO_3$-based nanostructures and thin films are actively being developed. High specific surface area, defect-rich structures, oxygen vacancies, and heterojunction formation can enhance the chemiresistive response and sensitivity. These features may also improve selectivity toward $NO_2$, $H_2S$, CO, $NH_3$, and volatile organic compounds [4,26,36,39,69,71,116]. For selected sensor architectures, ppb-level detection has been reported, which is particularly important for environmental monitoring, industrial safety, and air-quality diagnostics.

In gas sensing, $WO_3$ is widely used to detect $NO_2$, $H_2$, $H_2S$, CO, and $NH_3$. $MoO_3$ and $MoO_{3-x}$ are attractive because of their high surface acidity, tunable oxygen-vacancy concentration, and ability to interact selectively with water, oxygen, and reducing gas molecules [39,49,69,71,116,117]. In $WO_3/MoO_3$-based gas sensors, target molecules interact with surface oxygen species, oxygen vacancies, and W–O–Mo interfacial sites, leading to changes in the charge-carrier concentration and electrical resistance. Figure 19 illustrates this concept for a chemiresistive $WO_3/MoO_3$ nanocomposite sensing channel exposed to oxidizing and reducing gas molecules. In $WO_3/MoO_3$ nanocomposites, these effects can be further amplified through interfacial charge redistribution, modulation of the depletion-layer width, and the formation of additional adsorption-active sites at W–O–Mo boundaries. Thus, the gas-sensing performance of $WO_3/MoO_3$ heterostructures should be interpreted not only in terms of surface area or grain size, but also as the result of coupled surface chemistry, oxygen-defect engineering, and W–O–Mo interfacial electronic effects.

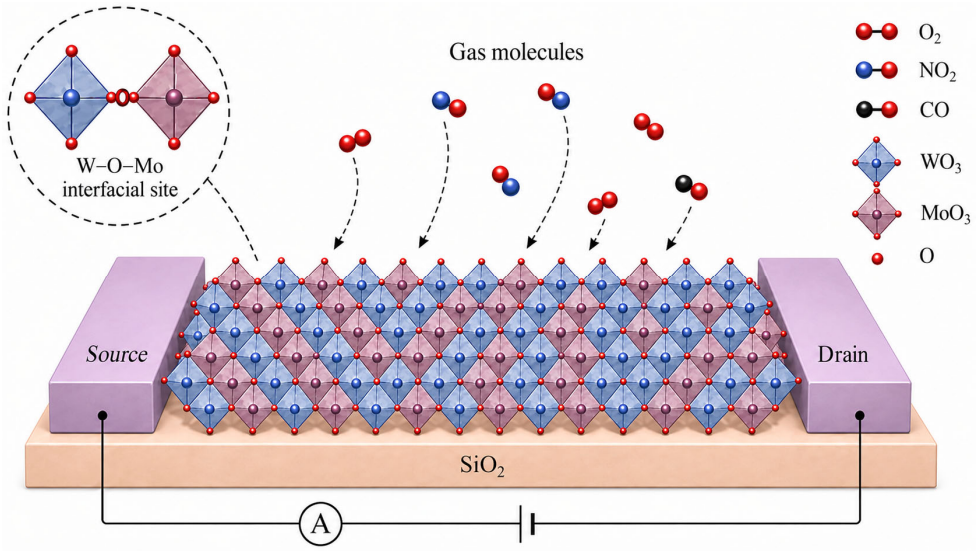



**Figure 19.** Schematic illustration of a $WO_3/MoO_3$ nanocomposite chemiresistive gas sensor. Dashed arrows indicate the approach and adsorption of gas molecules onto the $WO_3/MoO_3$ sensing surface; the dashed circular callout highlights a representative W–O–Mo interfacial site; the source–drain circuit illustrates the chemiresistive electrical readout.

In $WO_3/MoO_3$ heterostructures, the gas-sensing response can be enhanced by modulation of the potential-barrier height at W–O–Mo interfaces and by redistribution of adsorbed oxygen species. However, an increased response does not by itself prove interfacial synergy. Similar improvements may arise from reduced grain size, increased porosity, a higher concentration of oxygen vacancies, or changes in humidity. Figure 20 compares the $H_2$-sensing responses of different $MoO_3$ phases. It demonstrates that the phase state and morphology of $MoO_3$ can strongly affect the sensor signal even without a $WO_3$ component. For $WO_3/MoO_3$ composites, this highlights the need to verify the phase state of the $MoO_3$ component before attributing enhanced sensing performance to W–O–Mo interfacial synergy.

For practical gas-sensing devices, a high response alone is insufficient. At present, stable operation under these conditions cannot be claimed for an unencapsulated, calibration-free chemiresistor. Without hydrophobic protection or active thermal stabilization, practical use would require a continuous $WO_3$-rich conduction network, spatially confined $MoO_3$ domains, independent humidity/temperature referencing, and multivariate drift compensation. Validation should include humidity cycling, mixed-gas interference, temperature variations, and long-term baseline stability. Although α-$MoO_3$@$WO_3$ nanosheets demonstrated enhanced triethylamine sensing at an optimum temperature of 200 °C, robust room-temperature operation in complex atmospheres was not established [56]. Operating temperature, baseline drift, selectivity in complex gas mixtures, and resistance to humidity must also be considered. $WO_3/MoO_3$ composites are particularly attractive because their sensing behavior can be tuned through the balance between $MoO_3$-derived acidic surface sites and n-type electronic transport in $WO_3$. Nevertheless, this interpretation requires mechanistic validation by DRIFTS, operando XPS, or at least systematic measurements under controlled humidity and mixed-gas atmospheres, since otherwise enhanced response may be incorrectly attributed to W–O–Mo interfacial synergy.

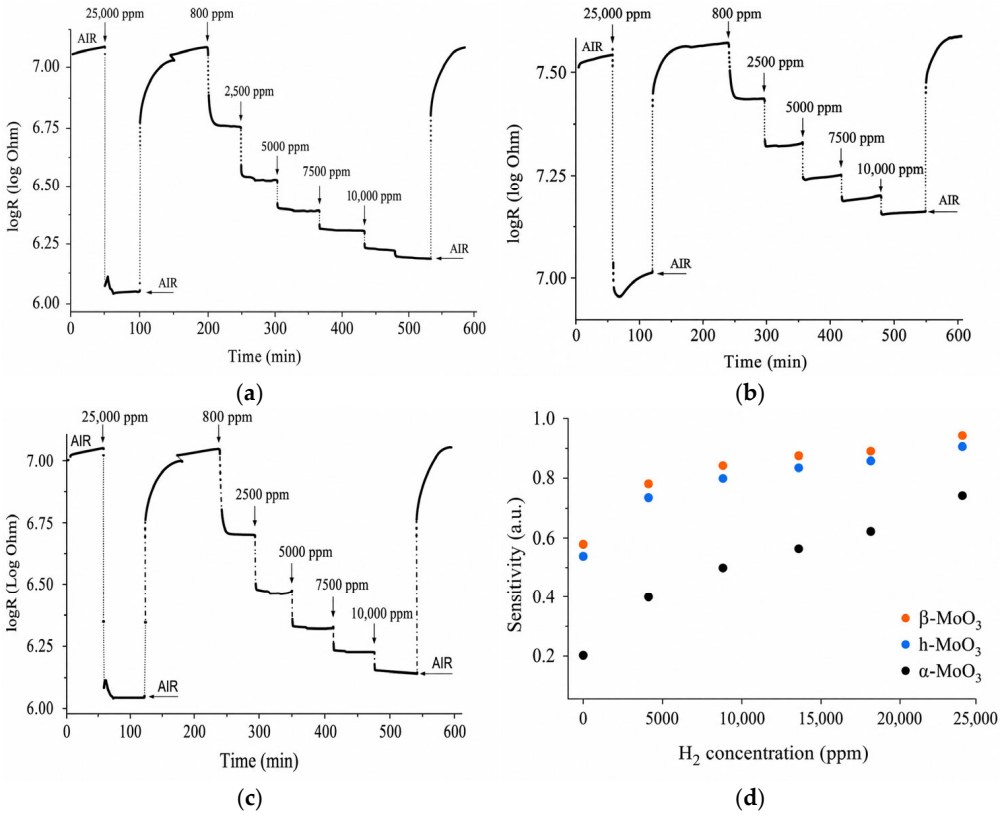



**Figure 20.** Gas-sensing response of different $MoO_3$ polymorphs toward $H_2$: (**a**) $MoO_3$-10, monoclinic phase ($CrCl_3$, 240 °C, 6 h); (**b**) $MoO_3$-8, orthorhombic phase (CTAB, 240 °C, 6 h); (**c**) $MoO_3$-1, hexagonal phase (90 °C, 3 h); and (**d**) sensitivity of the $MoO_3$ polymorphs. Reproduced from [71] under the terms of the Creative Commons Attribution license (CC BY 4.0).

### *4.5. Supercapacitors and Lithium-Ion Batteries*

In energy-storage applications, $WO_3$ and $MoO_3$ can participate in reversible pseudocapacitive and limited ion-insertion reactions, but deep lithiation of $MoO_3$ may proceed by conversion rather than intercalation. $WO_3$ is valuable as a comparatively stable pseudocapacitive framework. The layered structure of α-$MoO_3$ provides accessible $Li^+$-transport pathways, but the commonly cited theoretical value of approximately 1117 mAh $g^{-1}$ is the six-electron deep-conversion limit for Equation (1). It is not a reversible electrochromic or intercalation capacity [22,39,45]. Therefore, high reversible capacity, specific capacitance, and optical charge storage must be discussed separately from the theoretical conversion limit. Developing $WO_3$/$MoO_3$ nanocomposites and hybridizing them with highly conductive carbon matrices such as rGO are effective strategies for increasing active-site accessibility, accelerating coupled electron–ion transport, buffering conversion-induced stress, and improving cycling stability. For example, a $MoO_3$/$WO_3$/rGO nanocomposite was reported to deliver a specific capacitance of 583 F $g^{-1}$ while retaining 92.6% of its capacitance after 2000 cycles [103]. Such ternary $WO_3$/$MoO_3$/carbon architectures demonstrate that high-performance electrodes require electronically conductive and mechanically resilient frameworks capable of stabilizing repeated ion insertion/extraction and limiting irreversible conversion.

Performance analysis in supercapacitors and LIBs should therefore distinguish three contributions: surface-controlled pseudocapacitance, comparatively reversible limited intercalation, and deep conversion that is often only partially reversible. $WO_3$ provides a relatively stable three-dimensional framework for reversible ion insertion, whereas α-$MoO_3$ offers layered transport pathways but becomes a major source of mechanical degrada-

tion when lithiation progresses toward $Mo^0/Li_2O$ formation. Capacities approaching the 1117 mAh $g^{-1}$ theoretical limit indicate increasing participation of the $Mo^{6+} \rightarrow Mo^0$ conversion pathway, not a reversible electrochromic intercalation process. The design objective should therefore not be to maximize $MoO_3$ content or lithiation depth. Instead, $WO_3/MoO_3$ architectures should combine mechanical stability, electronic connectivity, and ionic accessibility to sustain the genuinely reversible fraction of charge storage during long-term cycling [39,45,46].

Several architecture-level strategies are particularly promising for $WO_3/MoO_3$-based energy-storage electrodes. $WO_3/MoO_3$ nanolaminates can limit the thickness of $MoO_3$-rich layers and thereby suppress deep intercalation and mechanical degradation. $WO_3/MoO_3$/rGO and related carbon-hybrid architectures improve electronic conductivity while buffering intercalation-induced stress. ALD-derived nanohybrids, in turn, provide precise control over oxide-layer thickness, a high density of W–O–Mo interfaces, and short ion-diffusion pathways [64,79,103,118,119].

For such devices, performance evaluation should not be limited to specific capacitance alone. A comprehensive assessment must include capacitance retention after cycling, charge-transfer resistance, post-cycling morphological changes, and preservation of the phase composition. When the increase in capacitance originates from uncontrolled reduction of $MoO_3$ or the formation of suboxide phases, the initial improvement in electrochemical performance may be followed by accelerated degradation of the system. Therefore, composition alone does not govern the efficiency and durability of $WO_3/MoO_3$-based electrochemical devices. Electrode architecture, interfacial stability, phase integrity, and the ability of the active layer to maintain coupled ion–electron transport during long-term cycling are also critical.

Table 8 summarizes the key architectural requirements for $WO_3/MoO_3$-based electrodes, including film thickness, electrical conductivity, defect chemistry, porosity, and interfacial state, and relates them to their functional roles, potential degradation risks, and appropriate diagnostic methods. Such a framework provides a basis for moving beyond isolated performance metrics toward the rational design of mechanically stable, electronically connected, and ionically accessible electrode architectures.

**Table 8.** Architectural requirements for $WO_3/MoO_3$ electrodes for energy storage.

| Parameter | Desired State | Functional Rationale | Potential Risk | Diagnostics |
|---|---|---|---|---|
| $MoO_3$-domain thickness | Thin layer or nanodomain | Shortens $Li^+$-diffusion pathways and reduces intercalation-induced stress | Deep intercalation and loss of contact between active domains | SEM/TEM before and after cycling |
| Electrical conductivity | Continuous electronic network | Reduces internal resistance and improves rate capability | Insulating $MoO_3$ domains limit rate performance | EIS; four-point probe |
| Defect chemistry | Moderate concentration of oxygen vacancies | Enhances redox activity and facilitates ion–electron transport | Phase drift and formation of $MoO_2$/suboxide phases | XPS, XRD, Raman spectroscopy |
| Porosity | Accessible but mechanically stable porous structure | Increases the accessible area of active redox sites | Cracking and loss of adhesion | SEM; profilometry |
| Interface | Stable W–O–Mo contacts | Facilitates charge transfer and interfacial ion–electron transport | Phase segregation and degradation of interfacial connectivity | STEM-EDS/EELS; XPS depth profiling |

The optimization of each parameter involves a trade-off between performance enhancement and unavoidable degradation risks. For example, increasing the active-layer

thickness can improve capacitance, but it also lengthens ion-diffusion pathways and may promote mechanical failure. Similarly, excessive defect density may enhance redox activity but can also induce phase drift and structural instability. Here, interfacial synergy requires stable W–O–Mo interfaces. These interfaces facilitate charge transfer but may be susceptible to phase segregation. The proposed set of diagnostic methods, including SEM, EIS, XPS, and STEM-EDS, enables a comprehensive assessment of whether the electrode meets the required architectural criteria and allows degradation processes to be identified at an early stage.

### *4.6. Photoelectrochemical and Photocatalytic Devices*

In photocatalytic and photoelectrochemical systems, $WO_3/MoO_3$ heterostructures are attractive because they provide a platform for tuning photogenerated charge separation, oxygen-defect chemistry, and interfacial band alignment. $WO_3$ acts as a relatively stable n-type photoactive oxide, while oxygen-deficient $MoO_{3-x}$ can reshape the interfacial energy landscape and introduce defect-mediated charge-transfer pathways. Nevertheless, defect engineering must remain controlled, since excessive oxygen vacancies or deeply reduced Mo species may become recombination centers and compromise long-term photoactivity.

Figure 21 presents a conceptual framework for designing $WO_3/MoO_3$-based photocatalytic and photoelectrochemical architectures.

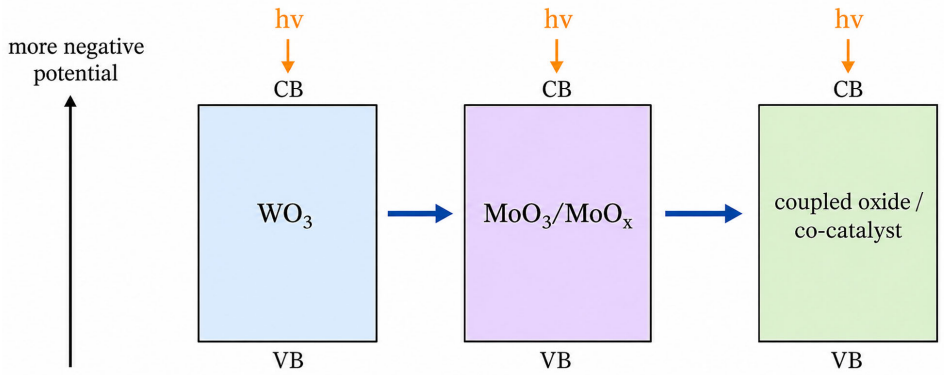



**Figure 21.** Photocatalytic and photoelectrochemical design based on band alignment and interfacial effects.

The scheme emphasizes that device performance is governed not only by the energetic alignment of the constituent oxides but also by interfacial charge separation, surface-reaction kinetics, controlled defect chemistry, and resistance to photocorrosion. In this context, $WO_3$ acts as the photoactive and chemically stable framework, whereas $MoO_3/MoO_x$ is most effective as a confined interfacial modifier coupled with an additional oxide or co-catalyst. The diagram is qualitative and does not imply a universal band-offset configuration for all $WO_3/MoO_3$ heterostructures.

Oxygen-deficient $WO_3/MoO_{3-x}$ heterostructures can reduce electron–hole recombination, promote molecular oxygen activation, and enhance the photocatalytic oxidation of organic pollutants. For the optimized $WO_3/MoO_{3-x}$ composition designated WOM83%, RhB degradation reached 98% within 40 min. The same composition exhibited a photocatalytic $H_2$ evolution rate of up to 4214.2 μmol $h^{-1}{\cdot}g^{-1}$ [104]. Thus, interfacial synergy in $WO_3/MoO_{3-x}$ heterostructures reflects the combined influence of oxygen-vacancy engineering, interfacial charge separation, band-structure modulation, and preservation of phase stability under illumination. Electrochemical impedance spectroscopy provides a useful tool for evaluating whether Mo modification reduces charge-transfer resistance. Figure 22 presents the EIS spectra of $WO_3$ and $WO_3$–$MoO_3$ photoanodes. A decrease in the Nyquist-arc radius for the optimized composition indicates facilitated interfacial charge

transfer; however, this interpretation should be supported by complementary analysis of morphology and phase composition.

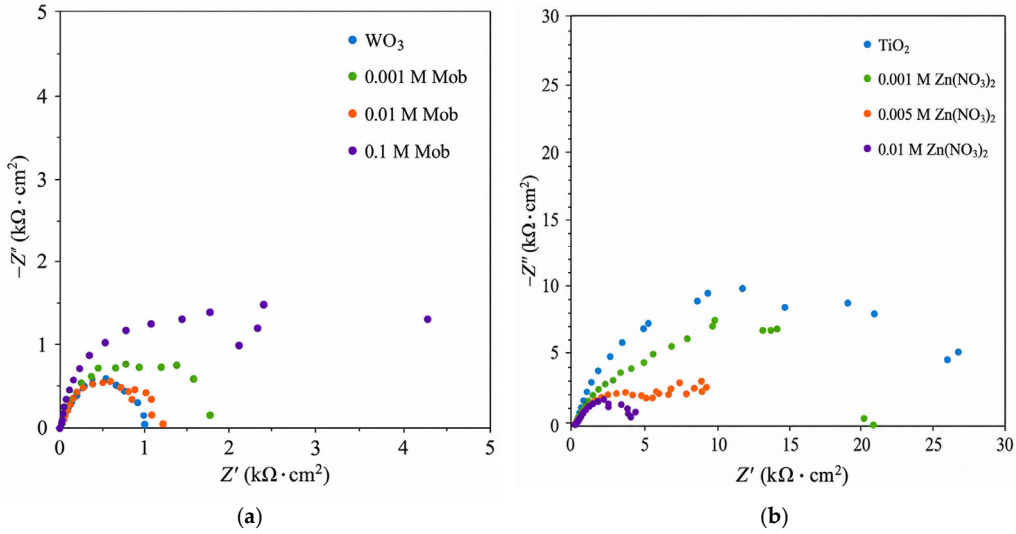



**Figure 22.** Electrochemical impedance spectroscopy (EIS) Nyquist plots of nanostructured photoanodes: (**a**) $WO_3$ and $WO_3$–$MoO_3$ prepared with different molybdate concentrations; (**b**) $TiO_2$ and $TiO_2$–ZnO prepared with different $Zn(NO_3)_2$ concentrations. Reproduced from [72] under the terms of the Creative Commons Attribution license (CC BY 4.0).

Photocurrent provides a direct measure of photogenerated charge-carrier generation, separation, and collection efficiency. Figure 23 presents the photoelectrochemical response of $WO_3$–$MoO_3$ nanostructures under illumination at different applied potentials. These results indicate that Mo-containing modification can promote charge separation and interfacial transfer; however, the optimum performance is governed by the molybdate-additive concentration, film thickness, surface morphology, and defect state.

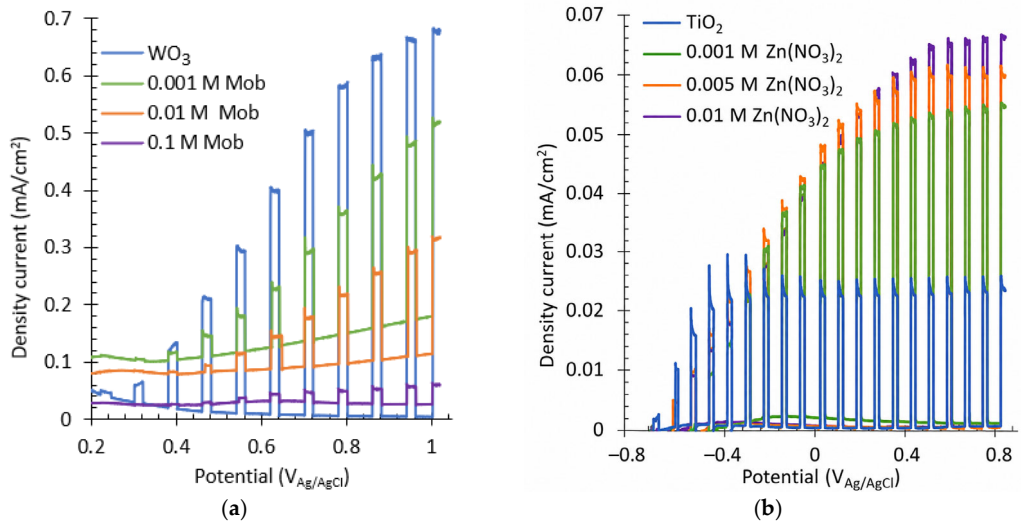



**Figure 23.** Water-splitting photocurrent response curves recorded under chopped illumination for nanostructured photoanodes: (**a**) $WO_3$ and $WO_3$–$MoO_3$ prepared with different molybdate concentrations; (**b**) $TiO_2$ and $TiO_2$–ZnO prepared with different $Zn(NO_3)_2$ concentrations. Reproduced from [72] under the terms of the Creative Commons Attribution license (CC BY 4.0).

In photocatalytic systems, $WO_3/MoO_{3-x}$ heterostructures can enhance the degradation of organic pollutants through more efficient $e^-/h^+$ separation and activation of molecular oxygen. Nevertheless, dye-degradation kinetics alone are insufficient to con-

firm a heterojunction-driven mechanism. PL quenching, EPR detection of reactive oxygen species, Mott–Schottky analysis, photocurrent measurements, and carefully designed control samples with comparable morphology should support this interpretation. These methods distinguish the effects of band alignment and interfacial charge transfer from simple surface-area or defect-concentration effects [37,104–106,108,109,120].

### *4.7. Optoelectronics*

The high work function of $MoO_3$ makes it one of the most important hole-injection and charge-selective oxide interlayers in organic electronics. In such devices, $MoO_3$ does not necessarily function as a bulk active layer; its key role is to provide energetic alignment at the electrode/organic-semiconductor interface. In this application, $WO_3$–$MoO_3$ interfacial synergy can improve chemical stability, enable optical tuning, and support the formation of multilayer oxide stacks [11,23,121].

For OLEDs and organic optoelectronic devices, the main performance criteria include low turn-on voltage, high luminance, external quantum efficiency, operational stability, and resistance to contact degradation. In this context, excessive oxygen nonstoichiometry can be detrimental because it modifies the work function and introduces trap states. Therefore, for $MoO_3$/$WO_3$ interlayers, UPS/KPFM analysis and nanometer-scale thickness control are particularly important.

### *4.8. Biomedical and Antibacterial Applications of Mo–W–O Systems*

Biomedical and antibacterial applications provide another context in which Mo–W–O interfacial synergy may be explored. The antibacterial activity of these materials against *Escherichia coli* has been associated with local acidification, surface redox processes, and reactive oxygen species. Visible-light pathways involving oxygen-deficient $W_{18}O_{49}$ may also contribute [107,122]. Although this research direction remains less mature than electrochromic, sensing, and energy-storage applications, it demonstrates the expanding functional scope of $WO_3$/$MoO_3$-based composites beyond conventional thin-film device technologies [122].

### *4.9. Reliability, Scalability, and Criteria for Device Translation*

For all $WO_3$/$MoO_3$-based device platforms, the key challenge is the long-term preservation of functional performance, structural integrity, and interfacial synergy under realistic operating conditions. Degradation manifests differently depending on the application. In electrochromic devices, it appears as loss of optical modulation and residual coloration. In gas sensors, it leads to baseline drift and humidity sensitivity. In energy-storage electrodes, it causes capacitance fading and resistance growth. In photoelectrochemical systems, it results in photocorrosion or enhanced charge recombination. These failure modes demonstrate that high initial performance is not sufficient for device relevance unless the W–O–Mo interfacial architecture remains chemically and mechanically stable during cycling.

Device translation therefore requires moving beyond laboratory-scale optimization toward reproducible control of composition, thickness, morphology, defect chemistry, and W–O–Mo interfacial connectivity over large areas. Particularly promising approaches include combinatorial sputtering, ALD-derived nanolaminates, spray-coating with optical monitoring, and electrodeposition combined with in situ diagnostics. In this context, the ability to fabricate larger films is not the only measure of scalability. Spatial uniformity, adhesion, optical/electrical response, and cycling durability must also be preserved across the entire active area. Regardless of the fabrication route, it is essential to verify that W–O–Mo interfacial contacts and the associated functional response are retained after cycling. Therefore, reliability testing, post-mortem structural analysis, and operando characteri-

zation should become mandatory criteria for translating $WO_3/MoO_3$ architectures from model materials into practical functional devices.

Table 9 summarizes the main degradation scenarios for electrochromic, sensing, energy-storage, photoelectrochemical, and optoelectronic $WO_3/MoO_3$-based devices, together with mitigation strategies and post-test diagnostic methods. This framework provides practical criteria for assessing device reliability and for selecting architectures suitable for scalable implementation.

**Table 9.** Main degradation scenarios and mitigation strategies in $WO_3/MoO_3$-based devices.

| Device | Degradation Scenario | Main Cause | Mitigation Strategy | Post-Test Diagnostics/Control |
|---|---|---|---|---|
| Electrochromic window | Loss of optical contrast; residual coloration | Ion trapping; excessive oxygen vacancies; cracking | Optimized porosity; thin $MoO_3$ interfacial layer; mild annealing | UV–Vis cycling; XPS; SEM |
| Gas sensor | Signal drift; humidity interference | $MoO_3$ hydration; changes in surface adsorbates | Hydrophobic protection; temperature modulation; humidity calibration | Repeated response cycles; DRIFTS/XPS |
| Supercapacitor | Capacitance fading | Volume expansion of $MoO_3$; loss of electrical/mechanical contact | $MoO_3$ nanodomains; conductive carbon matrix; ALD-limited oxide thickness | EIS; SEM/TEM; cyclic GCD testing |
| PEC/photocatalysis | Photocurrent decrease; loss of catalytic activity | Defect-mediated recombination; photocorrosion | Controlled oxygen vacancies; protective layers; pH optimization | Photocurrent; PL; post-test XRD/XPS |
| OLED/electrode interlayer | Increase in $V_O$; luminance decay | Work-function shift; metal diffusion | Nanometer-scale control of $MoO_3/WO_3$; barrier layer | J–V–L; UPS/KPFM; aging tests |

Overall, the most promising $WO_3/MoO_3$ systems are not bulk mixed oxides, but thin-film architectures with controlled phase connectivity, such as gradient layers, nanolaminates, $MoO_3$-rich interfaces, $WO_3$ frameworks with Mo-modified surfaces, and hybrids with conductive matrices. These architectures make it possible to combine the strong electrochromic response of $WO_3$, the layered ion-transport pathways of $MoO_3$, and tunable W–O–Mo interfacial coupling within a single multifunctional platform. Their technological value is therefore defined by more than the intrinsic properties of the individual oxides. It also arises from interfacial charge redistribution, oxygen-vacancy regulation, modified ion-transport pathways, and the formation of new active sites. Consequently, the transition from single-phase oxide films to interface-engineered $WO_3/MoO_3$ nanocomposites represents a key strategy for developing smart windows, gas sensors, supercapacitors, lithium-ion storage systems, photoactive coatings, organic electronics, and other sustainable device technologies.

## 5. Outlook for $WO_3/MoO_3$ Nanocomposite Thin Films: From Interface Engineering to Sustainable Device Technologies

The future development of $WO_3/MoO_3$ nanocomposite thin films will be defined not by the simple mixing of two oxides, but by the controlled engineering of phase connectivity, defect chemistry, and W–O–Mo interfacial states. This shift is important because the same nominal W:Mo ratio can lead to fundamentally different architectures, including amorphous mixed oxides, phase-segregated composites, nanolaminates, gradient coatings, and oxygen-deficient suboxide systems. Therefore, a key scientific challenge is to establish reproducible links between synthesis conditions, interfacial structure, oxygen-vacancy concentration, valence-state distribution, and device-level functionality.

First-principles modeling provides an important foundation for understanding $WO_3/MoO_3$ systems. Representative calculations have addressed several aspects of the

individual oxides. These include $WO_3$ polymorph stability [123], oxygen-vacancy energetics [47], and polaron formation and transport [124,125]. For $MoO_3$, calculations cover vacancy formation [126], defect-mediated adsorption [127], and Li adsorption, diffusion, and lithiation-induced deformation [128,129]. Related computational–experimental work on coherent $\alpha$-$MoO_3$/$\eta$-$Mo_4O_{11}$ lattice pinning [45] and experimental $WO_3/MoO_{3-x}$ heterojunctions [104] further motivates explicit interface modeling. However, geometry-matched calculations for realistic $WO_3/MoO_3$ interfaces remain insufficient to establish universal W–O–Mo bonding configurations, vacancy-segregation energies, or valence- and conduction-band offsets. Future studies should therefore combine experimentally constrained interface models with calculations of defect energetics, band alignment, ion migration, and mechanically induced interfacial strain.

Among the different application areas, electrochromic coatings and smart-window devices remain the closest to practical implementation. $WO_3$ provides strong cathodic coloration and reversible ion insertion, whereas $MoO_3$ can modify charge transport, defect chemistry, optical response, and interfacial stability [130]. Future progress should therefore be assessed by more than record optical modulation or coloration efficiency. It also requires the combined optimization of optical contrast, switching kinetics, residual coloration, cycling durability, and large-area uniformity.

A particularly important direction is the integration of electrochromic and energy-storage functions within a single thin-film platform. Since optical switching and pseudocapacitive charge storage both rely on coupled ion–electron processes, $WO_3/MoO_3$ architectures can serve as multifunctional active layers for smart windows with energy-storage capability. Nanolaminates, porous but mechanically stable coatings, and hybrids with conductive carbon matrices are especially promising for this purpose. These architectures can shorten ion-diffusion pathways, improve electronic conductivity, and mitigate mechanical degradation during repeated insertion/extraction cycles.

Gas sensing, photocatalysis, and photoelectrochemical applications represent more complex but highly promising directions. In gas sensors, $WO_3/MoO_3$ composites can combine n-type transport, surface acidity, oxygen-vacancy chemistry, and W–O–Mo interfacial barriers. However, future studies must clearly distinguish true interfacial effects from changes caused by surface area, porosity, humidity, grain size, or phase composition. In photocatalysis and photoelectrochemistry, $WO_3/MoO_{3-x}$ systems should be considered defect-engineered heterojunctions in which oxygen vacancies and band alignment govern charge separation, $O_2$ activation, and surface reactivity. The central task is to enhance charge separation while avoiding excessive defect-mediated recombination and photocorrosion.

Organic electronics, transparent electrodes, and charge-selective interlayers represent another important application field. In these systems, $WO_3$ and $MoO_3$ are used not as bulk active materials, but as ultrathin interface-modifying layers. The decisive parameters are work-function tuning, energetic alignment, nanometer-scale thickness control, and long-term contact stability.

From a technological perspective, the transition from laboratory samples to functional devices requires reproducibility over large areas. Scalable processing must simultaneously control composition, thickness, morphology, valence state, oxygen-vacancy concentration, and functional response. Combinatorial sputtering, ALD/MLD nanolaminates, spray-coating with in situ optical monitoring, and electrodeposition with charge/current diagnostics are particularly promising in this regard. Future progress requires controlled synthesis, evidence-based interfacial diagnostics, standardized testing protocols, and long-term reliability assessment. Meeting these requirements could transform $WO_3/MoO_3$ nanocomposite thin films from model materials into practical platforms for smart, energy-efficient, and sustainable devices.

## 6. Conclusions

This review demonstrates that $WO_3/MoO_3$ nanocomposite thin films and heterostructures should not be viewed as a simple combination of two related Group VI oxides. Instead, they represent a distinct class of interface-engineered functional materials. Their properties are governed by the coupled effects of $WO_3$ structural connectivity, the layered nature of $\alpha$-$MoO_3$, oxygen nonstoichiometry, mixed $W^{6+}/W^{5+}$ and $Mo^{6+}/Mo^{5+}$ redox states, and the quality of W–O–Mo interfacial contacts. In these systems, composition, phase state, defect chemistry, morphology, and interface structure are not secondary factors. They are key design parameters that determine ion–electron transport, optical absorption, surface reactivity, charge separation, and long-term functional stability.

1. Improved performance in $WO_3/MoO_3$ films should not automatically be attributed to W–O–Mo interfacial synergy, as similar effects may arise from changes in thickness, porosity, grain size, hydration, oxygen-vacancy concentration, or suboxide formation. Therefore, reliable interpretation of $WO_3/MoO_3$ nanocomposites requires direct correlation between functional testing and structural, morphological, valence-state, and interfacial diagnostics. These measurements should be performed on the same sample series. Methods such as XRD, Raman spectroscopy, XPS/XANES, SEM/TEM, EIS, PL spectroscopy, Mott–Schottky analysis, UPS/KPFM, and operando or post-mortem characterization are essential for distinguishing true interfacial effects from morphology- or defect-driven enhancement.
2. The synthesis route plays a decisive role in defining the active architecture of $WO_3/MoO_3$ systems. Magnetron sputtering and combinatorial co-sputtering are particularly suitable for constructing composition–structure–property maps. Sol–gel processing, spin-coating, dip-coating, and spray-coating are attractive for scalable coatings. Electrodeposition and anodization enable porous, hydrated, and substrate-adherent layers. ALD/CVD provide nanometer-scale control of interfaces and nanolaminate architectures, whereas PLD and evaporation are valuable for preparing dense model heterostructures. Thus, the fabrication method should be considered a functional design tool. It determines film thickness, W/Mo distribution, phase connectivity, oxygen-defect density, and the stability of W–O–Mo contacts.
3. $WO_3/MoO_3$-based thin films offer a broad application landscape, including electrochromic smart windows, electrochromic energy-storage devices, gas sensors, supercapacitors, lithium-ion storage systems, photocatalytic and photoelectrochemical coatings, transparent electrodes, OLEDs, organic optoelectronics, and antibacterial surfaces. Across these applications, their main advantage lies in the possibility of simultaneously tuning optical modulation, ion insertion, electron transport, surface redox activity, charge selectivity, and interfacial stability. However, practical implementation is still limited by insufficient reproducibility, phase instability, $MoO_3$ hydration, uncontrolled oxygen-defect formation, cycling-induced degradation, and the absence of standardized protocols for comparing device performance.
4. The most promising future direction is the transition from uncontrolled mixed oxides to deliberately designed thin-film architectures. These include gradient coatings, nanolaminates, $MoO_3$-rich interfaces, $WO_3$ frameworks with Mo-modified surfaces, oxygen-deficient $WO_3/MoO_{3-x}$ heterostructures, and hybrids with conductive matrices. Such architectures can integrate several key functions within a single multifunctional platform. These include the strong electrochromic response of $WO_3$, the layered ion-transport pathways of $MoO_3$, and tunable W–O–Mo interfacial coupling. If future studies combine controlled synthesis, evidence-based interfacial diagnostics, long-term reliability testing, and scalable processing, $WO_3/MoO_3$ nanocomposite

thin films can progress from promising laboratory materials toward practical smart, energy-efficient, and sustainable device technologies.

**Author Contributions:** Conceptualization, A.V.S. (Aleksei V. Shchegolkov); methodology, I.A.K.; software, A.V.S. (Aleksei V. Shchegolkov); validation, A.V.S. (Alexandr V. Shchegolkov); formal analysis, A.V.S. (Alexandr V. Shchegolkov); investigation, V.V.K.; resources, V.O.M.; data curation, V.V.K.; writing—original draft preparation, A.V.S. (Aleksei V. Shchegolkov); writing—review and editing, A.V.S. (Aleksei V. Shchegolkov); visualization, A.V.S. (Aleksei V. Shchegolkov); supervision, A.V.S. (Alexandr V. Shchegolkov); project administration, A.V.S. (Aleksei V. Shchegolkov); funding acquisition, A.V.S. (Aleksei V. Shchegolkov). All authors have read and agreed to the published version of the manuscript.

**Funding:** This work was financially supported by the Moscow Polytechnic University within the framework of the grant named after Pyotr Kapitsa.

**Data Availability Statement:** No new experimental data were obtained; the qualitative comparative assessments are derived from the cited literature.

**Acknowledgments:** This work was financially supported by the Moscow Polytechnic University within the framework of the grant named after Pyotr Kapitsa.

**Conflicts of Interest:** The authors declare no conflicts of interest.

## Abbreviations

The following abbreviations are used in this manuscript:

| Abbreviation | Definition |
|---|---|
| 3D | three-dimensional |
| ALD | atomic layer deposition |
| ALD/CVD | atomic layer deposition/chemical vapor deposition |
| ALD/MLD | atomic layer deposition/molecular layer deposition |
| CBP | 4,4′-bis(N-carbazolyl)-1,1′-biphenyl |
| CC BY | Creative Commons Attribution license |
| CE | coloration efficiency |
| CS | crystallographic shear |
| CTAB | cetyltrimethylammonium bromide |
| CV | cyclic voltammetry or cyclic voltammogram, depending on context |
| CVD | chemical vapor deposition |
| DFT | density functional theory |
| DRIFTS | diffuse reflectance infrared Fourier-transform spectroscopy |
| EDS | energy-dispersive X-ray spectroscopy |
| EELS | electron energy-loss spectroscopy |
| EIS | electrochemical impedance spectroscopy |
| EPR | electron paramagnetic resonance |
| EXAFS | extended X-ray absorption fine structure |
| FE-SEM | field-emission scanning electron microscopy |
| FTO | fluorine-doped tin oxide |
| GCD | galvanostatic charge–discharge |
| HRTEM | high-resolution transmission electron microscopy |
| IPCE | incident photon-to-current efficiency |
| ITO | indium tin oxide |
| J–V–L | current density–voltage–luminance characteristics |
| KPFM | Kelvin probe force microscopy |
| LIB | lithium-ion battery |
| LSPR | localized surface plasmon resonance |
| MLD | molecular layer deposition |

| | |
|---|---|
| NIR | near-infrared |
| OLED | organic light-emitting diode |
| PEC | photoelectrochemical |
| PL | photoluminescence |
| PLD | pulsed laser deposition |
| PVD | physical vapor deposition |
| PVP | polyvinylpyrrolidone |
| RBS | Rutherford backscattering spectrometry |
| rGO | reduced graphene oxide |
| RhB | rhodamine B |
| RMS | reactive magnetron sputtering |
| ROS | reactive oxygen species |
| SE | spectroscopic ellipsometry |
| SEM | scanning electron microscopy |
| STEM | scanning transmission electron microscopy |
| TEM | transmission electron microscopy |
| TMO | transition metal oxide |
| UPS | ultraviolet photoelectron spectroscopy |
| UV | ultraviolet |
| UV–Vis | ultraviolet–visible |
| UV–Vis–NIR | ultraviolet–visible–near-infrared |
| VOCs | volatile organic compounds |
| XANES | X-ray absorption near-edge structure |
| XPS | X-ray photoelectron spectroscopy |
| XRD | X-ray diffraction |
| Symbol/notation | Meaning in the manuscript |
| $A^+$ | monovalent intercalating cation in the generalized electrochromic reaction; typically $H^+$, $Li^+$, or $Na^+$ |
| $A_xMO_3$ | bronze-like intercalated oxide phase formed after coupled cation–electron insertion |
| Ag | silver |
| CO | carbon monoxide |
| $d^0$ | zero d-electron configuration |
| *E. coli* | *Escherichia coli* |
| $e^-$ | electron |
| $h^+$ | hole |
| $H_2$ | hydrogen |
| $H_2S$ | hydrogen sulfide |
| $H^+$ | proton |
| $H_xMoO_3$/$H_xWO_3$ | proton-intercalated molybdenum/tungsten oxide bronze-like phases |
| $K^+$ | potassium ion |
| $Li^+$ | lithium ion |
| $Li_xC_6$ | lithiated graphite phase |
| $Li_xMoO_3$/$Li_xWO_3$ | lithium-intercalated molybdenum/tungsten oxide bronze-like phases |
| M | metal cation in the general formula $MO_3$; here W or Mo |
| $MO_3$ | general formula for transition-metal trioxides such as $WO_3$ and $MoO_3$ |
| $MO_6$ | metal–oxygen octahedron used as a structural unit in $WO_3$ and $MoO_3$ |
| $Mo^{4+}$, $Mo^{5+}$, $Mo^{6+}$ | molybdenum oxidation states involved in reduction/oxidation and defect chemistry |
| $MoO_2$ | molybdenum dioxide |
| $MoO_3$ | molybdenum trioxide |
| $\alpha$-$MoO_3$ | orthorhombic layered $\alpha$ phase of molybdenum trioxide |
| $MoO_{3-x}$ | oxygen-deficient molybdenum trioxide |
| $MoO_{3-\delta}$ | slightly oxygen-deficient molybdenum trioxide; $\delta$ denotes a small oxygen deficiency |

| | |
|---|---|
| $MoO_x$ | generic notation for molybdenum oxides with variable oxygen content |
| Mo–$O_x$ | surface molybdenum–oxygen sites with variable oxygen coordination/nonstoichiometry |
| $Mo_4O_{11}$ | reduced molybdenum oxide/molybdenum suboxide |
| $Mo_8O_{23}$ | molybdenum crystallographic-shear suboxide |
| $Mo_9O_{26}$ | molybdenum crystallographic-shear suboxide |
| $Na^+$ | sodium ion |
| $NH_3$ | ammonia |
| $NO_2$ | nitrogen dioxide |
| $O_2$ | molecular oxygen |
| O 1s | oxygen 1s core-level region in XPS spectra |
| $OH^-$ | hydroxyl group/ion |
| $ReO_3$ | rhenium trioxide structure type used as a reference framework for $WO_3$ |
| $V_2O_5$ | vanadium pentoxide |
| $V_O$ | oxygen vacancy |
| $W^{4+}$, $W^{5+}$, $W^{6+}$ | tungsten oxidation states involved in reduction/oxidation and defect chemistry |
| W 4f | tungsten 4f core-level region in XPS spectra |
| W–O–Mo | interfacial tungsten–oxygen–molybdenum bond/contact |
| $WO_3$ | tungsten trioxide |
| $WO_{3-x}$ | oxygen-deficient tungsten trioxide |
| $WO_x$ | generic notation for tungsten oxides with variable oxygen content |
| $WO_6$ | tungsten–oxygen octahedron |
| $W_{18}O_{49}$ | oxygen-deficient tungsten oxide/Magnéli-type suboxide |
| $W_{20}O_{58}$ | oxygen-deficient tungsten oxide/crystallographic-shear suboxide |
| $W_{25}O_{73}$ | oxygen-deficient tungsten oxide/crystallographic-shear suboxide |
| $W_5O_{14}$ | oxygen-deficient tungsten oxide/crystallographic-shear suboxide |
| x | degree of oxygen deficiency or intercalation, depending on the formula |
| δ | small deviation from stoichiometric oxygen content |
| ΔT | optical transmittance modulation |

## References


1. Fortunato, E.; Barquinha, P.; Martins, R. Oxide Semiconductor Thin-Film Transistors: A Review of Recent Advances. *Adv. Mater.* **2012**, *24*, 2945–2986. [CrossRef] [PubMed]
2. Simon, P.; Gogotsi, Y. Materials for Electrochemical Capacitors. *Nat. Mater.* **2008**, *7*, 845–854. [CrossRef]
3. Boltasseva, A.; Atwater, H.A. Low-Loss Plasmonic Metamaterials. *Science* **2011**, *331*, 290–291. [CrossRef]
4. Korotcenkov, G. Metal Oxides for Solid-State Gas Sensors: What Determines Our Choice? *Mater. Sci. Eng. B* **2007**, *139*, 1–23. [CrossRef]
5. Granqvist, C.G. Electrochromics for Smart Windows: Oxide-Based Thin Films and Devices. *Thin Solid Films* **2014**, *564*, 1–38. [CrossRef]
6. Granqvist, C.G. Transparent Conductors as Solar Energy Materials: A Panoramic Review. *Sol. Energy Mater. Sol. Cells* **2007**, *91*, 1529–1598. [CrossRef]
7. Niklasson, G.A.; Granqvist, C.G. Electrochromics for Smart Windows: Thin Films of Tungsten Oxide and Nickel Oxide, and Devices Based on These. *J. Mater. Chem.* **2007**, *17*, 127–156. [CrossRef]
8. Mortimer, R.J. Electrochromic Materials. *Chem. Soc. Rev.* **1997**, *26*, 147–156. [CrossRef]
9. Riess, I. Mixed Ionic–Electronic Conductors—Material Properties and Applications. *Solid State Ion.* **2003**, *157*, 1–17. [CrossRef]
10. Kudo, A.; Miseki, Y. Heterogeneous Photocatalyst Materials for Water Splitting. *Chem. Soc. Rev.* **2009**, *38*, 253–278. [CrossRef]
11. Meyer, J.; Hamwi, S.; Kröger, M.; Kowalsky, W.; Riedl, T.; Kahn, A. Transition Metal Oxides for Organic Electronics: Energetics, Device Physics and Applications. *Adv. Mater.* **2012**, *24*, 5408–5427. [CrossRef]
12. MacManus-Driscoll, J.L.; Zerrer, P.; Wang, H.; Yang, H.; Yoon, J.; Fouchet, A.; Yu, R.; Blamire, M.G.; Jia, Q. Strain Control and Spontaneous Phase Ordering in Vertical Nanocomposite Heteroepitaxial Thin Films. *Nat. Mater.* **2008**, *7*, 314–320. [CrossRef]
13. Ramesh, R.; Schlom, D.G. Whither Oxide Electronics? *MRS Bull.* **2008**, *33*, 1006–1014. [CrossRef]
14. Lábadi, Z.; Takács, D.; Zolnai, Z.; Petrik, P.; Fried, M. Compositional Optimization of Sputtered $WO_3/MoO_3$ Films for High Coloration Efficiency. *Materials* **2024**, *17*, 1000. [CrossRef]

15. Fried, M.; Bogar, R.; Takács, D.; Lábadi, Z.; Horváth, Z.E.; Zolnai, Z. Investigation of Combinatorial $WO_3$–$MoO_3$ Mixed Layers by Spectroscopic Ellipsometry Using Different Optical Models. *Nanomaterials* **2022**, *12*, 2421. [CrossRef]
16. Jittiarporn, P.; Sikong, L.; Kooptarnond, K.; Taweepreda, W.; Stoenescu, S.; Badilescu, S.; Truong, V.-V. Electrochromic Properties of $MoO_3$–$WO_3$ Thin Films Prepared by a Sol–Gel Method, in the Presence of a Triblock Copolymer Template. *Surf. Coat. Technol.* **2017**, *327*, 66–74. [CrossRef]
17. Deb, S.K. Optical and Photoelectric Properties and Colour Centres in Thin Films of Tungsten Oxide. *Philos. Mag.* **1973**, *27*, 801–822. [CrossRef]
18. Berggren, L.; Niklasson, G.A. Optical Charge Transfer Absorption in Lithium-Intercalated Tungsten Oxide Thin Films. *Appl. Phys. Lett.* **2006**, *88*, 081906. [CrossRef]
19. Akbar, I.; Inamdar, Y.S.; Kim, B.U.; Jang, H.I.; Jung, W.; Kim, D.-Y.; Kim, H. Effects of Oxygen Stoichiometry on Electrochromic Properties in Amorphous Tungsten Oxide Films. *Thin Solid Films* **2012**, *520*, 5367–5371. [CrossRef]
20. Hsu, C.-S.; Chan, C.-C.; Huang, H.-T.; Peng, C.-H.; Hsu, W.-C. Electrochromic Properties of Nanocrystalline $MoO_3$ Thin Films. *Thin Solid Films* **2008**, *516*, 4839–4844. [CrossRef]
21. Wang, D.; Li, J.-N.; Zhou, Y.; Xu, D.-H.; Xiong, X.; Peng, R.-W.; Wang, M. Van der Waals epitaxy of ultrathin α-$MoO_3$ sheets on mica substrate with single-unit-cell thickness. *Appl. Phys. Lett.* **2016**, *108*, 053107. [CrossRef]
22. Whittingham, M.S. Lithium Batteries and Cathode Materials. *Chem. Rev.* **2004**, *104*, 4271–4302. [CrossRef]
23. Greiner, M.T.; Lu, Z.-H. Thin-Film Metal Oxides in Organic Semiconductor Devices: Their Electronic Structures, Work Functions and Interfaces. *NPG Asia Mater.* **2013**, *5*, e55. [CrossRef]
24. Sivakumar, R.; Jayachandran, M.; Sanjeeviraja, C. Effect of Annealing on Structural, Surface and Optical Properties of PVD-EBE α-$MoO_3$ Thin Films for Electrochromic Devices. *Surf. Eng.* **2004**, *20*, 385–390. [CrossRef]
25. Chen, S.; Xiao, Y.; Xie, W.; Wang, Y.; Hu, Z.; Zhang, W.; Zhao, H. Facile Strategy for Synthesizing Non-Stoichiometric Monoclinic Structured Tungsten Trioxide ($WO_{3-x}$) with Plasma Resonance Absorption and Enhanced Photocatalytic Activity. *Nanomaterials* **2018**, *8*, 553. [CrossRef]
26. Wang, C.; Yin, L.; Zhang, L.; Xiang, D.; Gao, R. Metal Oxide Gas Sensors: Sensitivity and Influencing Factors. *Sensors* **2010**, *10*, 2088–2106. [CrossRef]
27. Patil, S.B.; Udayabhanu, U.; Kishore, B.; Nagaraju, G.; Dupont, J. High Capacity $MoO_3$/rGO Nanocomposite Anode for Lithium-Ion Batteries: An Intuition into the Conversion Mechanism of $MoO_3$. *New J. Chem.* **2018**, *42*, 18569–18577. [CrossRef]
28. Ma, Y.; Wang, L.; Liu, D.; Liu, Y.; Yang, G.; Qian, Y.; Lei, W. Functionalized $MoO_3$ Nanosheets for High-Efficiency RhB Removal. *Glob. Chall.* **2023**, *7*, 2200154. [CrossRef]
29. Lee, J.; Kim, S.K.; Sohn, Y. Understanding Photocatalytic Coupled-Dye Degradation, and Photoelectrocatalytic Water Splitting and $CO_2$ Reduction over $WO_3$/$MoO_3$ Hybrid Nanostructures. *J. Ind. Eng. Chem.* **2018**, *62*, 362–374. [CrossRef]
30. Zhou, D.; Shi, F.; Xie, D.; Wang, D.H.; Xia, X.H.; Wang, X.L.; Gu, C.D.; Tu, J.P. Bi-functional Mo-doped $WO_3$ nanowire array electrochromism-plus electrochemical energy storage. *J. Colloid Interface Sci.* **2016**, *465*, 112–120. [CrossRef]
31. Ramana, C.V.; Mauger, A.; Julien, C.M. Growth, Characterization and Performance of Bulk and Nanoengineered Molybdenum Oxides for Electrochemical Energy Storage and Conversion. *Prog. Cryst. Growth Charact. Mater.* **2021**, *67*, 100533. [CrossRef]
32. Tang, K.; Farooqi, S.A.; Wang, X.; Yan, C. Recent Progress on Molybdenum Oxides for Rechargeable Batteries. *ChemSusChem* **2019**, *12*, 755–771. [CrossRef]
33. Li, Y.; Fu, Z.-Y.; Su, B.-L. Hierarchically Structured Porous Materials for Energy Conversion and Storage. *Adv. Funct. Mater.* **2012**, *22*, 4634–4667. [CrossRef]
34. Zhao, F.; Wang, B.; Zhang, W.; Cao, S.; Liu, L.; Elezzabi, A.Y.; Li, H.; Yu, W.W. Counterbalancing the Interplay between Electrochromism and Energy Storage for Efficient Electrochromic Devices. *Mater. Today* **2023**, *66*, 431–447. [CrossRef]
35. Hsu, S.-C.; Chao, S.-H.; Wu, N.-J.; Huang, J.-H.; Kang, J.-L.; Weng, H.C.; Liu, T.-Y. Facile Synthesis of Hybrid $WO_3$/$MoO_x$ Electrochromic Films for Application in Complementary Electrochromic Devices. *J. Alloys Compd.* **2023**, *945*, 169256. [CrossRef]
36. An, F.; Zhou, A.F.; Feng, P.X. Effect of Tungsten Oxide Nanostructures on Sensitivity and Selectivity of Pollution Gases. *Sensors* **2020**, *20*, 4801. [CrossRef]
37. Zhong, Y.; Peng, C.; He, Z.; Chen, D.; Jia, H.; Zhang, J.; Ding, H.; Wu, X. Interface Engineering of Heterojunction Photocatalysts Based on 1D Nanomaterials. *Catal. Sci. Technol.* **2020**, *11*, 27–42. [CrossRef]
38. Pirker, L.; Višić, B.; Škapin, S.D.; Dražić, G.; Kovač, J.; Remškar, M. Multi-Stoichiometric Quasi-Two-Dimensional $W_nO_{3n-1}$ Tungsten Oxides. *Nanoscale* **2020**, *12*, 15102–15114. [CrossRef]
39. da Silva Júnior, M.G.; Arzuza, L.C.C.; Sales, H.B.; Farias, R.M.d.C.; Neves, G.d.A.; Lira, H.d.L.; Menezes, R.R. A Brief Review of $MoO_3$ and $MoO_3$-Based Materials and Recent Technological Applications in Gas Sensors, Lithium-Ion Batteries, Adsorption, and Photocatalysis. *Materials* **2023**, *16*, 7657. [CrossRef]
40. Tan, F.; Zhou, J.; Guo, Z.; Zhang, C.; Yu, S.; Yang, Y.; Xie, Y.; Cao, X.; Wu, X.; Gao, X.; et al. Research Progress on Electrochromic Properties of $WO_3$ Thin Films. *Coatings* **2025**, *15*, 1310. [CrossRef]

41. Martín-Ramos, P.; Fernández-Coppel, I.; Avella, M.; Martín-Gil, J. α-$MoO_3$ Crystals with a Multilayer Stack Structure Obtained by Annealing from a Lamellar $MoS_2$/g-$C_3N_4$ Nanohybrid. *Nanomaterials* **2018**, *8*, 559. [CrossRef]
42. Mineo, G.; Ruffino, F.; Mirabella, S.; Bruno, E. Investigation of $WO_3$ Electrodeposition Leading to Nanostructured Thin Films. *Nanomaterials* **2020**, *10*, 1493. [CrossRef]
43. Morankar, P.J.; Amate, R.U.; Yewale, M.A.; Jeon, C.-W. Effect of Annealing Temperature on Morphology and Electrochromic Performance of Electrodeposited $WO_3$ Thin Films. *Crystals* **2024**, *14*, 1038. [CrossRef]
44. Guo, Y.; Robertson, J. Origin of the High Work Function and High Conductivity of $MoO_3$. *Appl. Phys. Lett.* **2014**, *105*, 222110. [CrossRef]
45. Sun, S.; Han, Z.; Liu, W.; Xia, Q.; Xue, L.; Lei, X.; Zhai, T.; Su, D.; Xia, H. Lattice Pinning in $MoO_3$ via Coherent Interface with Stabilized $Li^+$ Intercalation. *Nat. Commun.* **2023**, *14*, 6391. [CrossRef]
46. Nikgoftar, K.; Reddy, A.K.M.R.; Reddy, M.V.; Zaghib, K. Carbonaceous Materials as Anodes for Lithium-Ion and Sodium-Ion Batteries. *Batteries* **2025**, *11*, 123. [CrossRef]
47. Wang, W.; Janotti, A.; Van de Walle, C.G. Role of Oxygen Vacancies in Crystalline $WO_3$. *J. Mater. Chem. C* **2016**, *4*, 6641–6648. [CrossRef]
48. Noby, S.Z.; Fakharuddin, A.; Schupp, S.; Sultan, M.; Krumova, M.; Drescher, M.; Azarkh, M.; Boldt, K.; Schmidt-Mende, L. Oxygen Vacancies in Oxidized and Reduced Vertically Aligned α-$MoO_3$ Nanoblades. *Mater. Adv.* **2022**, *3*, 3571–3581. [CrossRef]
49. Methani, W.; Pál, E.; Lipcsei, S.; Ugi, D.; Pászti, Z.; Groma, I.; Jenei, P.; Dankházi, Z.; Kun, R. Nanomechanical, Structural and Electrochemical Investigation of Amorphous and Crystalline $MoO_3$ Thin-Film Cathodes in Rechargeable Li-Ion Batteries. *Batteries* **2022**, *8*, 80. [CrossRef]
50. Lee, Y.-J.; Lee, T.; Soon, A. Phase Stability Diagrams of Group 6 Magnéli Oxides and Their Implications for Photon-Assisted Applications. *Chem. Mater.* **2019**, *31*, 4282–4290. [CrossRef]
51. Migas, D.B.; Shaposhnikov, V.L.; Borisenko, V.E. Tungsten Oxides. II. The Metallic Nature of Magnéli Phases. *J. Appl. Phys.* **2010**, *108*, 093714. [CrossRef]
52. Lakshmi-Narayana, A.; Hussain, O.M.; Ramana, C.V.; Camacho-Lopez, M.; Abdel-Ghany, A.; Hashem, A.; Mauger, A.; Julien, C.M. Molybdenum-Suboxide Thin Films as Anode Layers in Planar Lithium Microbatteries. *Electrochem* **2020**, *1*, 160–187. [CrossRef]
53. Vincent, R.C.; Luo, Y.; Andrews, J.L.; Zohar, A.; Zhou, Y.; Yan, Q.; Mozur, E.M.; Preefer, M.B.; Weker, J.N.; Cheetham, A.K.; et al. High-Rate Lithium Cycling and Structure Evolution in $Mo_4O_{11}$. *Chem. Mater.* **2022**, *34*, 4122–4133. [CrossRef]
54. Kim, H.S.; Cook, J.B.; Lin, H.; Ko, J.S.; Tolbert, S.H.; Ozolins, V.; Dunn, B. Oxygen Vacancies Enhance Pseudocapacitive Charge Storage Properties of $MoO_{3-x}$. *Nat. Mater.* **2017**, *16*, 454–460. [CrossRef]
55. Wu, C.; Wang, L.; Shi, J.; Xie, S.; Hu, Z.; Luo, D.; Chang, C.-R. Collaborative Interface Engineering of the $WO_3$–$MoO_3$ Heterostructure Enabling Accelerated $CO_2$ Cycloaddition with Epoxides. *Inorg. Chem.* **2026**, *65*, 5780–5790. [CrossRef]
56. Yan, S.; Yang, F.; Dong, X.; Zhang, C.; Xu, X.; Chi, Z.; Yang, W.; Xie, W. Rational Construction of α-$MoO_3$@$WO_3$ Nanosheets and Its Triethylamine Sensing Performances. *Ceram. Int.* **2024**, *50*, 14238–14246. [CrossRef]
57. Morankar, P.J.; Amate, R.U.; Bhosale, M.K.; Jeon, C.-W. PVP-Engineered $WO_3$/$TiO_2$ Heterostructures for High-Performance Electrochromic Applications with Enhanced Optical Modulation and Stability. *Polymers* **2025**, *17*, 1683. [CrossRef]
58. Kodan, N.; Singh, A.P.; Vandichel, M.; Wickman, B.; Mehta, B.R. Favourable Band Edge Alignment and Increased Visible Light Absorption in β-$MoO_3$/α-$MoO_3$ Oxide Heterojunction for Enhanced Photoelectrochemical Performance. *Int. J. Hydrogen Energy* **2018**, *43*, 15773–15783. [CrossRef]
59. Yun, J.; Jang, W.; Lee, T.; Lee, Y.; Soon, A. Aligning the Band Structures of Polymorphic Molybdenum Oxides and Organic Emitters in Light-Emitting Diodes. *Phys. Rev. Appl.* **2017**, *7*, 024025. [CrossRef]
60. Zheng, L.; Xu, Y.; Jin, D.; Xie, Y. Novel Metastable Hexagonal $MoO_3$ Nanobelts: Synthesis, Photochromic, and Electrochromic Properties. *Chem. Mater.* **2009**, *21*, 5681–5690. [CrossRef]
61. Tahini, H.A.; Tan, X.; Lou, S.N.; Scott, J.; Amal, R.; Ng, Y.H.; Smith, S.C. Mobile Polaronic States in α-$MoO_3$: An Ab Initio Investigation of the Role of Oxygen Vacancies and Alkali Ions. *ACS Appl. Mater. Interfaces* **2016**, *8*, 10911–10917. [CrossRef]
62. Inzani, K.; Nematollahi, M.; Vullum-Bruer, F.; Grande, T.; Reenaas, T.W.; Selbach, S.M. Electronic Properties of Reduced Molybdenum Oxides. *Phys. Chem. Chem. Phys.* **2017**, *19*, 9232–9245. [CrossRef]
63. Santos, H.L.S.; Bezerra, L.S.; Camargo, P.H.C.; Mascaro, L.H. Tailoring $WO_3$ Photoelectrodes with Defect-Rich $MoO_{3-x}$ Nanosheets for Efficient Water Splitting Reaction. *J. Solid State Electrochem.* **2025**, *29*, 2157–2167. [CrossRef]
64. Lopa, N.; Karbalaei Akbari, M.; Lu, H.-L.; Zhuiykov, S. ALD-Enabled $WO_3$–$MoO_3$ Nanohybrid Heterostructure for High-Performance Electrochemical Supercapacitors. *J. Energy Storage* **2024**, *84*, 110777. [CrossRef]
65. Marom, G.; Fischer, S.; Tuler, F.R.; Wagner, H.D. Hybrid Effects in Composites: Conditions for Positive or Negative Effects versus Rule-of-Mixtures Behaviour. *J. Mater. Sci.* **1978**, *13*, 1419–1426. [CrossRef]
66. Pazhamalai, P.; Krishnan, V.; Saleem, M.S.M.; Kim, S.; Seo, H. Investigating Composite Electrode Materials of Metal Oxides for Advanced Energy Storage Applications. *Nano Converg.* **2024**, *11*, 30. [CrossRef]

67. Rajpurohit, A.; Joannès, S.; Singery, V.; Sanial, P.; Laiarinandrasana, L. Hybrid Effect in In-Plane Loading of Carbon/Glass Fibre Based Inter- and Intraply Hybrid Composites. *J. Compos. Sci.* **2020**, *4*, 6. [CrossRef]
68. Phillips, M.G. Composition Parameters for Hybrid Composite Materials. *Composites* **1981**, *12*, 113–116. [CrossRef]
69. Ciftyürek, E.; Šmíd, B.; Li, Z.; Matolín, V.; Schierbaum, K. Spectroscopic Understanding of $SnO_2$ and $WO_3$ Metal Oxide Surfaces with Advanced Synchrotron Based; XPS-UPS and Near Ambient Pressure (NAP) XPS Surface Sensitive Techniques for Gas Sensor Applications under Operational Conditions. *Sensors* **2019**, *19*, 4737. [CrossRef]
70. Jiang, J.; Liu, Y.; Li, J.; Sun, A.; Li, S.; Guo, F.; Zhang, M.; Jie, W.; Hao, L. Multifunctional Ultralow-Power-Consumption Artificial Optoelectronic Synapses Based on the Heterojunctions of $MoO_3/WO_3$ for Neuromorphic Computing and Bionic Visual Systems. *ACS Appl. Mater. Interfaces* **2025**, *17*, 64743–64752. [CrossRef]
71. Nagyné-Kovács, T.; Studnicka, L.; Lukács, I.E.; László, K.; Pasierb, P.; Szilágyi, I.M.; Pokol, G. Hydrothermal Synthesis and Gas Sensing of Monoclinic $MoO_3$ Nanosheets. *Nanomaterials* **2020**, *10*, 891. [CrossRef]
72. Cifre-Herrando, M.; Roselló-Márquez, G.; Navarro-Gázquez, P.J.; Muñoz-Portero, M.J.; Blasco-Tamarit, E.; García-Antón, J. Characterization and Comparison of $WO_3/WO_3$–$MoO_3$ and $TiO_2/TiO_2$–ZnO Nanostructures for Photoelectrocatalytic Degradation of the Pesticide Imazalil. *Nanomaterials* **2023**, *13*, 2584. [CrossRef]
73. Pinto, O.M.; Toledo, R.P.; Barros, H.E.S.; Gonçalves, R.A.; Nunes, R.S.; Joshi, N.; Berengue, O.M. Advances and Challenges in $WO_3$ Nanostructures' Synthesis. *Processes* **2024**, *12*, 2605. [CrossRef]
74. Kotlarski, G.; Stoeva, D.; Dechev, D.; Ivanov, N.; Ormanova, M.; Mateev, V.; Marinova, I.; Valkov, S. Review on Metal (-Oxide, -Nitride, -Oxy-Nitride) Thin Films: Fabrication Methods, Applications and Future Characterization Methods. *Coatings* **2025**, *15*, 869. [CrossRef]
75. Song, X.C.; Wang, X.; Zheng, Y.F.; Yin, H.Y. Electrochromic Properties of $WO_3$–$MoO_3$ Nanocomposite Films Prepared by Electrodeposition Method. *Curr. Nanosci.* **2013**, *9*, 330–334. [CrossRef]
76. Xie, S.; Bi, Z.; Chen, Y.; He, X.; Guo, X.; Gao, X.; Li, X. Electrodeposited Mo-Doped $WO_3$ Film with Large Optical Modulation and High Areal Capacitance toward Electrochromic Energy-Storage Applications. *Appl. Surf. Sci.* **2018**, *459*, 774–781. [CrossRef]
77. Arvizu, M.A.; Granqvist, C.G.; Niklasson, G.A. Electrochromism in Sputter Deposited $W_{1-y}Mo_yO_3$ Thin Films. *J. Phys. Conf. Ser.* **2016**, *682*, 012005. [CrossRef]
78. Li, H.; Chen, J.; Cui, M.; Cai, G.; Eh, A.L.-S.; Lee, P.S.; Wang, H.; Zhang, Q.; Li, Y. Spray Coated Ultrathin Films from Aqueous Tungsten Molybdenum Oxide Nanoparticle Ink for High Contrast Electrochromic Applications. *J. Mater. Chem. C* **2016**, *4*, 33–38. [CrossRef]
79. Shchegolkov, A.V.; Lipkin, M.S.; Shchegolkov, A.V. Preparation of $WO_3$ Films on Titanium and Graphite Foil for Fuel Cell and Supercapacitor Applications by Electrochemical (Cathodic) Deposition Method. *Russ. J. Gen. Chem.* **2022**, *92*, 1161–1167. [CrossRef]
80. Diskus, M.; Nilsen, O.; Fjellvåg, H. Growth of Thin Films of Molybdenum Oxide by Atomic Layer Deposition. *J. Mater. Chem.* **2011**, *21*, 705–710. [CrossRef]
81. Drake, T.L.; Stair, P.C. Vapor Deposition of Molybdenum Oxide Using Bis(ethylbenzene) Molybdenum and Water. *J. Vac. Sci. Technol. A* **2016**, *34*, 051403. [CrossRef]
82. Mattinen, M.; King, P.J.; Khriachtchev, L.; Heikkilä, M.J.; Fleming, B.; Rushworth, S.; Mizohata, K.; Meinander, K.; Räisänen, J.; Ritala, M.; et al. Atomic Layer Deposition of Crystalline Molybdenum Oxide Thin Films and Phase Control by Post-Deposition Annealing. *Mater. Today Chem.* **2018**, *9*, 17–27. [CrossRef]
83. Vos, M.; Macco, B.; Thissen, N.F.W.; Bol, A.A.; Kessels, W.M.M. Atomic Layer Deposition of Molybdenum Oxide from $(N^tBu)_2(NMe_2)_2Mo$ and $O_2$ Plasma. *J. Vac. Sci. Technol. A* **2016**, *34*, 01A103. [CrossRef]
84. Lorenzo, D.; Tobaldi, D.M.; Tasco, V.; Esposito, M.; Passaseo, A.; Cuscunà, M. Molybdenum Precursor Delivery Approaches in Atomic Layer Deposition of α-$MoO_3$. *Dalton Trans.* **2023**, *52*, 902–908. [CrossRef]
85. Xu, Z.; Liu, X.; Zhou, J.; Yan, Y.; Song, Y.; Huang, Q.; Ren, H.; Ding, Y.; Zhang, X.; Zhao, Y.; et al. Atomic-Layer-Deposited H:$MoO_x$ Function Layer as Efficient Hole-Selective Passivating Contact in Silicon Solar Cells. *Mater. Today Energy* **2023**, *36*, 101362. [CrossRef]
86. Malm, J.; Sajavaara, T.; Karppinen, M. Atomic Layer Deposition of $WO_3$ Thin Films Using $W(CO)_6$ and $O_3$ Precursors. *Chem. Vap. Depos.* **2012**, *18*, 245–248. [CrossRef]
87. Balasubramanyam, S.; Sharma, A.; Vandalon, V.; Knoops, H.C.M.; Kessels, W.M.M.; Bol, A.A. Plasma-Enhanced Atomic Layer Deposition of Tungsten Oxide Thin Films Using $(^tBuN)_2(Me_2N)_2W$ and $O_2$ Plasma. *J. Vac. Sci. Technol. A* **2018**, *36*, 01B103. [CrossRef]
88. Mattinen, M.; Wree, J.-L.; Stegmann, N.; Ciftyurek, E.; El Achhab, M.; King, P.J.; Mizohata, K.; Räisänen, J.; Schierbaum, K.D.; Devi, A.; et al. Atomic Layer Deposition of Molybdenum and Tungsten Oxide Thin Films Using Heteroleptic Imido-Amidinato Precursors: Process Development, Film Characterization, and Gas Sensing Properties. *Chem. Mater.* **2018**, *30*, 8690–8701. [CrossRef]

89. Vernardou, D. Progress and challenges in industrially promising chemical vapour deposition processes for the synthesis of large-area metal oxide electrode materials designed for aqueous battery systems. *Materials* **2021**, *14*, 4177. [CrossRef]
90. Dong, W.; Lv, Y.; Xiao, L.; Fan, Y.; Zhang, N.; Liu, X. Bifunctional $MoO_3$–$WO_3$/Ag/$MoO_3$–$WO_3$ Films for Efficient ITO-Free Electrochromic Devices. *ACS Appl. Mater. Interfaces* **2016**, *8*, 33842–33847. [CrossRef]
91. Ou, N.C.; Su, X.; Bock, D.C.; McElwee-White, L. Precursors for Chemical Vapor Deposition of Tungsten Oxide and Molybdenum Oxide. *Coord. Chem. Rev.* **2020**, *421*, 213459. [CrossRef]
92. Ivanova, T.; Gesheva, K.; Hamelmann, F.; Popkirov, G.; Abrashev, M.; Ganchev, M.; Tzvetkova, E. Optical and Electrochromic Properties of CVD Mixed $MoO_3$–$WO_3$ Thin Films. *Vacuum* **2004**, *76*, 195–198. [CrossRef]
93. Hasani, A.; Le, Q.V.; Nguyen, T.P.; Choi, K.S.; Sohn, W.; Kim, J.K.; Jang, H.W.; Kim, S.Y. Facile Solution Synthesis of Tungsten Trioxide Doped with Nanocrystalline Molybdenum Trioxide for Electrochromic Devices. *Sci. Rep.* **2017**, *7*, 13258. [CrossRef]
94. Wei, C.-C.; Wu, T.-H.; Huang, J.-W.; Young, B.-L.; Jian, W.-B.; Lin, Y.-L.; Chen, J.-T.; Hsu, C.-S.; Ma, Y.-R.; Tsukagoshi, K. Nanoparticulate Films of $WO_3$ and $MoO_3$ Composites for Enhancing UV Light Electrochromic Transmittance Variation and Energy Storage Applications. *Electrochim. Acta* **2023**, *442*, 141897. [CrossRef]
95. Donnadieu, A.; Davazoglou, D.; Abdellaoui, A. Structure, Optical and Electro-Optical Properties of Polycrystalline $WO_3$ and $MoO_3$ Thin Films Prepared by Chemical Vapour Deposition. *Thin Solid Films* **1988**, *164*, 333–338. [CrossRef]
96. Wang, K.; Wu, H.; Meng, Y.; Zhang, Y.; Wei, Z. Integrated Energy Storage and Electrochromic Function in One Flexible Device: An Energy Storage Smart Window. *Energy Environ. Sci.* **2012**, *5*, 8384–8389. [CrossRef]
97. Faughnan, B.W.; Crandall, R.S. Optical Properties of Mixed-Oxide $WO_3$/$MoO_3$ Electrochromic Films. *Appl. Phys. Lett.* **1977**, *31*, 834–836. [CrossRef]
98. Madhavi, V.; Kondaiah, P.; Hussain, O.M.; Uthanna, S. Structural, Optical, and Electrochromic Properties of Pure and Mo-Doped $WO_3$ Films by RF Magnetron Sputtering. *Conf. Pap. Sci.* **2013**, *2013*, 104047. [CrossRef]
99. Chaichana, S.; Sikong, L.; Kooptarnond, K.; Chetpattananondh, K. The Electrochromic Property of $MoO_3$/$WO_3$ Nanocomposite Films. *IOP Conf. Ser. Mater. Sci. Eng.* **2018**, *378*, 012002. [CrossRef]
100. Gillissen, F.; Lobet, M.; Dewalque, J.; Colson, P.; Spronck, G.; Gouttebaron, R.; Duttine, M.; Faceira, B.; Rougier, A.; Henrard, L.; et al. Mixed Molybdenum–Tungsten Oxide as Dual-Band, VIS–NIR Selective Electrochromic Material. *Adv. Opt. Mater.* **2025**, *13*, 2401995. [CrossRef]
101. Li, H.; Li, J.; Hou, C.; Ho, D.; Zhang, Q.; Li, Y.; Wang, H. Solution-Processed Porous Tungsten Molybdenum Oxide Electrodes for Energy Storage Smart Windows. *Adv. Mater. Technol.* **2017**, *2*, 1700047. [CrossRef]
102. Li, H.; McRae, L.; Firby, C.J.; Al-Hussein, M.; Elezzabi, A.Y. Nanohybridization of Molybdenum Oxide with Tungsten Molybdenum Oxide Nanowires for Solution-Processed Fully Reversible Switching of Energy Storing Smart Windows. *Nano Energy* **2018**, *47*, 130–139. [CrossRef]
103. Askari, M.B.; Salarizadeh, P. $MoO_3$/$WO_3$/rGO as Electrode Material for Supercapacitor and Catalyst for Methanol and Ethanol Electrooxidation. *Sci. Rep.* **2024**, *14*, 9907. [CrossRef]
104. Shao, Y.; You, D.; Wan, Y.; Cheng, Q.; Pan, Z. An Investigation on a $WO_3$/$MoO_3-x$ Heterojunction Photocatalyst for Excellent Photocatalytic Performance and Enhanced Molecular Oxygen Activation Ability. *React. Chem. Eng.* **2024**, *9*, 70–81. [CrossRef]
105. Liu, Y.; Dong, X.L.; Yuan, Q.; Liang, J.S.; Zhou, Y.L.; Qu, X.H.; Dong, B. In-Situ Synthesis of $WO_{3-x}$/$MoO_{3-x}$ Heterojunction with Abundant Oxygen Vacancies for Efficient Photocatalytic Reduction of $CO_2$. *Colloids Surf. A Physicochem. Eng. Asp.* **2021**, *621*, 126582. [CrossRef]
106. Liu, Y.; Liu, Y.; Cheng, J.; Ma, L.; Xi, X.; Nie, Z. Preparation of $WO_3$/$MoO_{3-x}$ Composites from W–Mo Alloy Scrap and Its Adsorption-Photocatalytic Properties. *Opt. Mater.* **2024**, *157*, 116024. [CrossRef]
107. Mardare, C.C.; Hassel, A.W. Investigations on Bactericidal Properties of Molybdenum–Tungsten Oxides Combinatorial Thin Film Material Libraries. *ACS Comb. Sci.* **2014**, *16*, 631–639. [CrossRef]
108. Yin, H.; Kuwahara, Y.; Mori, K.; Cheng, H.; Wen, M.; Huo, Y.; Yamashita, H. Localized Surface Plasmon Resonances in Plasmonic Molybdenum Tungsten Oxide Hybrid for Visible-Light-Enhanced Catalytic Reaction. *J. Phys. Chem. C* **2017**, *121*, 23531–23540. [CrossRef]
109. Spetter, D.; Tahir, M.N.; Hilgert, J.; Khan, I.; Qurashi, A.; Lu, H.; Weidner, T.; Tremel, W. Solvothermal Synthesis of Molybdenum–Tungsten Oxides and Their Application for Photoelectrochemical Water Splitting. *ACS Sustain. Chem. Eng.* **2018**, *6*, 12641–12649. [CrossRef]
110. Mateen, S.; Nawaz, R.; Qamar, M.T.; Ali, S.; Iqbal, S.; Aslam, M.; Raheel, M.; Awwad, N.S.; Ibrahium, H.A. Integration of $WO_3$-Doped $MoO_3$ with ZnO Photocatalyst for the Removal of 2-Nitrophenol in Natural Sunlight Illumination. *Catalysts* **2023**, *13*, 1262. [CrossRef]
111. Cannavale, A.; Fiorito, F.; Ayr, U.; Martellotta, F. Smart Electrochromic Windows to Enhance Building Energy Efficiency and Visual Comfort. *Energies* **2020**, *13*, 1449. [CrossRef]
112. Budaiwi, I.M.; Fasi, M.A. Assessing the Energy-Saving Potential and Visual Comfort of Electrochromic Smart Windows in Office Buildings: A Case Study in Dhahran, Saudi Arabia. *Sustainability* **2023**, *15*, 9632. [CrossRef]

113. Sun, F.; Pal, R.; Eom, S.Y.; Choi, J.W.; Zhang, W.; Jeong, B.; Park, J.S. Fast-Switching Dual-Cathode Electrochromic Smart Windows for Year-Round Building Energy Savings. *Nat. Commun.* **2025**, *16*, 9569. [CrossRef]
114. DeForest, N.; Shehabi, A.; O'Donnell, J.; Garcia, G.; Greenblatt, J.; Lee, E.S.; Selkowitz, S.; Milliron, D.J. United States Energy and $CO_2$ Savings Potential from Deployment of Near-Infrared Electrochromic Window Glazings. *Build. Environ.* **2015**, *89*, 107–117. [CrossRef]
115. Chang, C.-C.; Chi, P.-W.; Chandan, P.; Lin, C.-K. Electrochemistry and Rapid Electrochromism Control of $MoO_3/V_2O_5$ Hybrid Nanobilayers. *Materials* **2019**, *12*, 2475. [CrossRef]
116. Mirzaei, A.; Leonardi, S.G.; Neri, G. Detection of Hazardous Volatile Organic Compounds (VOCs) by Metal Oxide Nanostructures-Based Gas Sensors: A Review. *Ceram. Int.* **2016**, *42*, 15119–15141. [CrossRef]
117. Gajarska, Z.; Zelenka, K.C.; Rathner, P.; Recktenwald, D.; Kollender, J.P.; Shahzad, K.; Müller, N.; Hassel, A.W.; Mardare, C.C. Insight into antimicrobial properties via self-acidification of compounds from the molybdenum–tungsten–oxygen system. *ACS Appl. Bio Mater.* **2019**, *2*, 1477–1488. [CrossRef]
118. Gao, T.; Xiao, X.; Dong, Z.; Lu, X.; Mao, L.; Wang, J.; Liu, Y.; Hu, Q.; Xu, J. Application of defect engineering via ALD in supercapacitors. *Batteries* **2024**, *10*, 438. [CrossRef]
119. Fleischmann, S.; Zeiger, M.; Quade, A.; Kruth, A.; Presser, V. Atomic Layer-Deposited Molybdenum Oxide/Carbon Nanotube Hybrid Electrodes: The Influence of Crystal Structure on Lithium-Ion Capacitor Performance. *ACS Appl. Mater. Interfaces* **2018**, *10*, 18675–18684. [CrossRef]
120. Araújo, E.S.; Pereira, M.F.G.; da Silva, G.M.G.; Tavares, G.F.; Oliveira, C.Y.B.; Faia, P.M. A Review on the Use of Metal Oxide-Based Nanocomposites for the Remediation of Organics-Contaminated Water via Photocatalysis: Fundamentals, Bibliometric Study and Recent Advances. *Toxics* **2023**, *11*, 658. [CrossRef]
121. Gao, Z.; Feng, Z.; Chen, W.; Qu, W.; Ao, W.; Yang, T.; Li, J.; Gao, F. The Application of a Non-Doped Composite Hole Transport Layer of $[MoO_3/CBP]_n$ with Multi-Periodic Structure for High Power Efficiency Organic Light-Emitting Diodes. *RSC Adv.* **2019**, *9*, 4957–4962. [CrossRef]
122. Yan, Z.; Fan, J.; Zuo, Z.; Li, Z.; Zhang, J. $NH_3$ Adsorption on the Lewis and Brønsted Acid Sites of $MoO_3$(010) Surface: A Cluster DFT Study. *Appl. Surf. Sci.* **2014**, *288*, 690–694. [CrossRef]
123. Hamdi, H.; Salje, E.K.H.; Ghosez, P.; Bousquet, E. First-Principles Reinvestigation of Bulk $WO_3$. *Phys. Rev. B* **2016**, *94*, 245124. [CrossRef]
124. Bousquet, E.; Hamdi, H.; Aguado-Puente, P.; Salje, E.K.H.; Artacho, E.; Ghosez, P. First-Principles Characterization of Single-Electron Polaron in $WO_3$. *Phys. Rev. Res.* **2020**, *2*, 012052(R). [CrossRef]
125. Tao, J.; Liu, T. Electron and Hole Polaron Formation and Transport in Monoclinic $WO_3$ Studied by Hybrid Functional Approach. *J. Phys. Chem. C* **2023**, *127*, 16204–16210. [CrossRef]
126. Akande, S.O.; Chroneos, A.; Vasilopoulou, M.; Kennou, S.; Schwingenschlögl, U. Vacancy Formation in $MoO_3$: Hybrid Density Functional Theory and Photoemission Experiments. *J. Mater. Chem. C* **2016**, *4*, 9526–9531. [CrossRef]
127. Huan, C.; Wang, P.; He, B.; Cai, Y.; Ke, Q. Oxygen-Deficient $\alpha$-$MoO_3$ with Enhanced Adsorption and State-Quenching of $H_2O$ for Gas Sensing: A DFT Study. *J. Mater. Chem. C* **2022**, *10*, 1839–1849. [CrossRef]
128. Li, F.; Cabrera, C.R.; Chen, Z. Theoretical Design of $MoO_3$-Based High-Rate Lithium-Ion Battery Electrodes: The Effect of Dimensionality Reduction. *J. Mater. Chem. A* **2014**, *2*, 19180–19188. [CrossRef]
129. Hu, R.; Liu, T.; Chen, B.; Zhou, J. Atomic Mechanical Properties of Structure and Diffusion in the $MoO_3$ Anode Materials during Lithiation. *Comput. Mater. Sci.* **2018**, *145*, 8–13. [CrossRef]
130. Shchegolkov, A.V.; Jang, S.-H.; Shchegolkov, A.V.; Rodionov, Y.V.; Sukhova, A.O.; Lipkin, M.S. A Brief Overview of Electrochromic Materials and Related Devices: A Nanostructured Materials Perspective. *Nanomaterials* **2021**, *11*, 2376. [CrossRef]


**Disclaimer/Publisher's Note:** The statements, opinions and data contained in all publications are solely those of the individual author(s) and contributor(s) and not of MDPI and/or the editor(s). MDPI and/or the editor(s) disclaim responsibility for any injury to people or property resulting from any ideas, methods, instructions or products referred to in the content.